# COMPUTATIONAL MODELING OF
# OVERHAUSER DYNAMIC NUCLEAR POLARIZATION IN LIQUIDS

by
Sami Emre Küçük

Submitted to the Graduate School of Engineering and Natural Sciences
in partial fulfillment of
the requirements for the degree of
Doctor of Philosophy

Sabanci University
July, 2016

# COMPUTATIONAL MODELING OF OVERHAUSER DYNAMIC NUCLEAR POLARIZATION IN LIQUIDS

APPROVED BY:

Asst. Prof. Dr. Deniz Sezer...............................................................................
      (Thesis Supervisor)

Prof. Dr. Cihan Saçlıoğlu..................................................................

Prof. Dr. Ali Rana Atılgan................................................................

Assoc. Prof. Dr. Levent Sarı.............................................................

Assoc. Prof. Dr. Özhan Özatay.........................................................

DATE OF APPROVAL:

ABSTRACT


COMPUTATIONAL MODELING OF OVERHAUSER DYNAMIC NUCLEAR

POLARIZATION IN LIQUIDS


Sami Emre Küçük

PhD Thesis, July 2014

Supervisor Deniz Sezer


Keywords: NMR, DNP, MD Simulations, *ab initio*

Since its discovery, nuclear magnetic resonance (NMR) spectroscopy has been a vital tool for molecular structure and function determination. Inherently, NMR signals suffer from lack of sensitivity, however Overhauser Dynamic Nuclear Polarization (ODNP) offers a substantial enhancement in the NMR signals exploiting the stochastic modulation of hyperfine interaction between electron and nuclear spins. The origin of the hyperfine interaction is known to comprise of dipolar and scalar couplings whose magnitudes can change depending on the nuclear spin. For instance, $^1$H ODNP is dominated by dipolar interaction while $^{13}$C may be influenced by both interactions. Therefore, prediction of the enhancement necessitates the knowledge of separate contributions. Although the dipolar contribution can be predicted via analytical models which exploit its geometric nature, the contribution of scalar interaction is impossible to predict using such analytical models since its magnitude depends on the electron spin density on the nucleus. Recently, a methodology based on molecular dynamics simulations was developed for predicting ODNP enhancements influenced by dipolar interaction. In this work, the strategy is successfully applied for proton ODNP of acetone and DMSO liquids doped with nitroxide TEMPOL. Due to its high sensitivity on ODNP enhancements, the fidelity of the rotational motion of the simulated molecules is also assessed by dielectric relaxation analysis. The scope of methodology is extended to take scalar interaction into account by performing DFT calculations. The functional and basis set dependency of the DFT calculations is investigated and quantitative agreement with the experiment is achieved for the carbons of acetone and chloroform.

ÖZET

SIVILARDA OVERHAUSER DİNAMİK NÜKLEER POLARİZASYONUNUN
HESAPLAMALI MODELLEMESİ

Sami Emre Küçük

PhD Tezi, Temmuz 2014

Süpervizör Deniz Sezer

Keywords: NMR, DNP, MD Simülasyonları, *ab initio*

Keşfedildiğinden bu yana, Nükleer Manyetik Rezonans (NMR) spektroskopisi molekül yapısı ve fonksiyonu belirlemede hayati bir araç haline gelmiştir. Doğası gereği, NMR sinyalleri düşük duyarlılıktan muzdariptir, ancak Overhauser Dinamik Nükleer Polarizasyonu (ODNP), elektron ve nükleer spinleri arasındaki hyperfine etkileşiminin rastsal değişiminden yararlanarak önemli ölçüde sinyal artışı sağlamaktadır. Etkileşimin kaynağının dipolar ve skaler eşleşmeler olduğu ve bunların katkılarının nükleer spin tipine göre değiştiği bilinmektedir. Mesela, $^{1}$H ODNP büyük ölçüde dipolar etkileşimin etkisindeyken, $^{13}$C ODNP her iki etkileşimden de etkilenebilir. Bu yüzden, sinyal artışının büyüklüğünün öngörüsü bu etkileşimlerin başlıbaşına katkılarını bilmeyi gerektirir. Dipolar etkileşimin katkısı, bu etkileşimin tamamen geometrik olan doğasından istifade eden analitik modeller vasıtasıyla öngörülebilse de, nükleer spin üzerindeki elektron spininin yoğunluğuna bağlı olan skaler etkileşimin katkısı analitik modellemeyle mümkün değildir. Yakın zamanda, ODNP sinyal artışını sadece dipolar etkileşimin etkisi altında olan proton için, moleküler dinamik (MD) simülasyonlarını kullanarak öngörmeyi amaçlayan bir metodoloji geliştirilmiştir. Nitroksit TEMPOL ile katkılanmış aseton ve DMSO sıvılarında proton ODNP artışlarını öngörmek için, bahsedilen metodoloji başarıyla uygulanmıştır. ODNP artışına olan yüksek hassasiyetinden dolayı, simülasyonu gerçekleştirilen moleküllerin dönme hareketlerinin uygunluk derecesi, dielektrik sönümlenme analiziyle incelenmiştir. Daha sonra metodolojinin ölçeği genişletilerek DFT hesaplamaları gerçekleştirilerek skaler etkileşimin de hesaba katılması sağlanmıştır. DFT hesaplamalarının fonksiyonal ve baz seti bağımlılığı araştırılmış ve aseton ve kloroform sıvıları için nicel olarak deneylerle uyuşan karbon ODNP sinyal artışları hesaplanmıştır.

*This thesis is dedicated to my wife, Elif.*

# Acknowledgements

First and foremost, I would like to acknowledge my thesis advisor Professor Deniz Sezer for his constant guidance, encouragment and patience. His energy and never-ending ideas have been a driving force for my accomplishments in this field. The skills I have gained have been invaluable and I am thankful to him for the rest of my life.

I would like to express my deepest appreciation to Prof. Cihan Saçlıoğlu for his excellent lectures which are invaluably precious in every minute. Also my special thanks go to other thesis jury members, Prof. Ali Rana Atılgan, Assoc. Prof. Levent Sarı and Assoc. Prof. Özhan Özatay for their kind support and help.

I would like to thank Tolga Çağlar for his friendship and precious conversations throughout my PhD years. I am also grateful to all physics graduate students in Sabanci, Nur Gürsoy, Onur Benli, Onur Akbal, Ali Asgharpour and countless friends.

I would like to thank Tuğçe Oruç for being a wonderful group member and all G022 friends for creating a fruitful working environment.

I gratefully acknowledge the financial support from TUBİTAK BİDEB scholarship which has been vital in my doctoral study.

Finally, I would like to thank my family, mother, father and brother for their continuous support. I could not be able to thank enough to my wife for believing in me throughout my PhD study.

# Contents

# List of Figures

# List of Tables

# Chapter 1

# INTRODUCTION

## 1.1. Motivation

Nuclear magnetic resonance (NMR) spectroscopy has been a valuable tool for obtaining structural and dynamical information about the various substances and biomolecules and it has attracted tremendous interest in many fields such as physics, structural biology, chemistry and medicine. Magnetic Resonance Imaging (MRI) which is based on the same principles of NMR, became a routine application in medicinal areas due to its non-invasive method.

Unfortunately, NMR suffers from the lack of sensitivity. The technique is based on exploiting the spin polarization of the nuclei in conjunction with the application of a strong magnetic field. However, the spin polarization for nuclei is in minuscule amounts. Even the largest one, $^{1}$H, has polarization on the order of $10^{-5}$ in room temperature. The low spin polarization issues the NMR signals to be weak thereby making the duration of detection undesirably long. This handicap gets even worse when the natural abundance of the employed nuclei is very small as in the case of $^{13}$C.

Many hyperpolarization techniques were developed to overcome the lack of sensitivity of NMR. A simple way to increase the signal intensity is to strengthen the applied magnetic field. However, even the largest superconducting magnets in this day (over 20 T) are unable to produce appreciable polarization. Another obvious method is to decrease the temperature but for experiments in the room temperature or for the medicinal purposes which necessitates the temperature to be body temperature, unfortunately this method is of no use. On the other hand, since the beginning of NMR, scientists developed elegant methods such as chemically induced dynamic nuclear polarization (CIDNP), parahydrogen induced polarization (PHIP), Overhauser dynamic nuclear polarization (ODNP) and many others.

Albert Overhauser predicted that the free electrons in the conducting metals transfer their polarization to the nearby nuclear spins [6] and soon after it was experimentally

1

proved [7]. The main concept behind the Overhauser effect is the relaxation mechanism governed by the hyperfine structure interaction between nuclear and electron spins. Although the theory was proposed that this event is applicable only in conducting metals, later it is shown that the effect can also be activated in liquids by free radicals which have an unpaired electron [8, 9]. Theoretically, this mechanism offers an enhancement up the order of $\sim$660 for $^1$H and $\sim$2600 for $^{13}$C, therefore its use is highly desirable for the NMR applications.

Although, the mechanism is discovered more than seventy years ago, together with the technical and instrumental developments, liquid-state Overhauser DNP has renewed attention. Numerous DNP experiments have been performed at high magnetic fields ($3 - 9$ T) for a variety of solvents and nuclei in the last decade. For instance, water protons at 3.4 T [10, 11, 12] and at 9.2 T [13], ethanol protons at 3.4 T [14] toluene protons at 3.4 T [15, 16] and at 9.2 T [3]. In addition experiments have been performed for other nuclei such as $^{13}$C [17, 18, 5], $^{15}$N at 0.35 T [19] and $^{19}$F [20, 21]. Despite the fact that the hydrodynamic models suggest the high-field DNP enhancements are negligibly small, these studies reported appreciable enhancements. Therefore, a quantitative prediction of DNP enhancements due to a specific free radical and solvent is desirable for a knowledge-based experiment.

Force-Field based Molecular dynamics (MD) simulations and also quantum mechanical *ab initio* calculations become a substantial tool to obtain both structural and dynamic information on the molecular level. The use of the simulations to connect to the experimental observables is indisputable nowadays. Accordingly, in the last couple of years, a methodology for prediction of the Overhauser DNP enhancements quantitatively that uses computer simulations has been developed [22, 23, 24]. In essence, hyperfine interaction between spins involves a dipolar part which depends on the spatial parameters of the inter-spin vector. In MD simulations, particles do not possess any spin information but the point-dipole approximation is proved by *ab initio* calculations to be a good approach [1]. The developed methodology puts use of simulated molecular motions and extract information about the dipolar interaction between the nuclear spin bearing molecules and electrons of the free radicals. The accuracy of this procedure is quantitatively shown to be in very good agreement with experiments [23, 24].

For $^1$H DNP, the dipolar interaction is dominant. However, if the scalar interaction has also influence on hyperfine interaction, which is true for some species such as $^{13}$C [9, 25] or $^{19}$F [20], then the use of quantum mechanical calculations is necessary. Therefore, the extension of the methodology to the *ab initio* is inevitable for the prediction of ODNP enhancements with the nuclei that is known to have the scalar coupling.

In this thesis, the methodology was applied to the $^1$H DNP for the acetone and DMSO cases. To validate the fidelity of the molecular motions in MD simulations, complex frequency response analysis was performed. The use of *ab initio* calculations was introduced

2

thereby the spectrum of the applicability to the variety of nuclear spins was broaden. The three-spin effect to the Overhauser DNP which is due to the case where multiple nuclear spins are present along with electron spin was also analyzed. Quantitative predictions for $^1$H and $^{13}$C have been made and compared with the experiments.

## 1.2.   Scope of the thesis

The 2nd chapter elucidates the theoretical background of magnetic resonance and DNP. A formal derivation of relaxation equations and spectral density functions using Redfield relaxation theory is given. Then briefly, basic concepts of the molecular dynamics simulations are explained and the methodology to calculate the spectral density functions from simulations are given.

In the 3rd chapter the methodology of calculating SDFs was applied for the case of $^1$H Overhauser DNP in liquids of acetone and DMSO. Various technical details about the MD simulations and then the validation of the simulations are expressed. Afterwards, by calculating the dipolar SDFs, various experimental parameters, such as coupling factor and relaxation rates are calculated. This chapter contains materials published in the Ref. [2].

In the 4th chapter, scalar interaction was incorporated to the methodology was applied for $^{13}$C DNP for the carbons of acetone. Along with the technical details about the MD and *ab initio* simulations, calculation of scalar SDFs are explained. The coupling factors are calculated from both dipolar and scalar SDFs and compared with experimental parameters. The three-spin contribution to the enhancement is calculated. The contents of this chapter is published in Ref. [4].

In the 5th chapter, the accuracy of the computation of the scalar coupling is improved by comparatively testing various functional and basis sets of *ab initio* methods. ODNP of chloroform and water-acetone solvents doped with TEMPOL is studied and calculated coupling factors are compared with experiments therefore most convenient choice of *ab initio* method is assessed. This chapter contains material from the publication of Ref. [1].

# Chapter 2

# THEORETICAL BACKGROUND

In this chapter, background to the dynamic nuclear polarization is summarized. First part introduces the basic principles of the magnetic resonance. In the second chapter relaxation phenomenon and the characteristic keywords for DNP are given. The third chapter gives a summary of the Redfield theory of relaxation. In the last chapter the methodology to obtain the experimental parameters from simulations and necessary procedure for validation of simulations are explained.

## 2.1. Magnetic Resonance and Dynamic Nuclear Polarization

All magnetic resonance experiments are based on the same concept, "spin". Both Nuclear Magnetic Resonance (NMR) and Electron Spin Resonance (ESR) experiments exploit the properties of nuclear and electronic spins, respectively. Underlying mechanism can be understood from classical and quantum mechanical perspectives and in this section, I will describe the mechanism using both points of views.

Classically, potential energy associated with interaction between the magnetic moment of a charged particle and the applied magnetic field is given as:

$$H = -\mu \cdot \mathbf{B}, \tag{2.1}$$

and magnetic moment is related to the angular momentum of the particle $\mathbf{L}$:

$$\mu = \gamma \mathbf{L}, \tag{2.2}$$

where $\gamma$ is the gyromagnetic ratio. If the magnetic moment of the particle is originated from its angular momentum, for instance a particle with a rotational motion, then the particle executes a precessional motion around the magnetic field direction. The frequency associated with this precession, called Larmor frequency ($\omega$) is related to the applied

magnetic field and the gyromagnetic ratio. For instance, if the magnetic field is uniform constant and in the z-direction[1], $\mathbf{B} = B_0\hat{z}$ , then the precession frequency is:

$$\omega = -\gamma B_0, \tag{2.3}$$

where the negative frequency represents the opposite directions of precessional motion with respect to the right hand rule [26].

If we move to the quantum description, we see that the definition of the Hamiltonian remains same except the observables are the quantum counterparts. The magnetic moment (operator) is related to orbital angular momentum operator:

$$\mu = \gamma\mathbf{L}_z = \gamma m\hbar l_z, \tag{2.4}$$

where $m$ and $l_z$ are the eigenvalues and eigenfunctions of the operator $L_z$, respectively and $\hbar$ is the reduced Planck constant. Analogous to the orbital angular momentum, we define the magnetic moment associated with the spin as:

$$\mu = \gamma\mathbf{I}, \tag{2.5}$$

where $I$ is the spin operator and $\gamma$ is the gyromagnetic ratio between spin angular momentum and the spin magnetic moment. Gyromagnetic ratio is an intrinsic property of all spins and defined for nuclear ($I$) and electron spins ($S$) as:

$$\begin{aligned}
\gamma_I &= \frac{g\mu_N}{\hbar}, \\
\gamma_S &= \frac{g\mu_B}{\hbar},
\end{aligned} \tag{2.6}$$

where $\mu_N$ and $\mu_B$ are nuclear and Bohr magnetons and $g$ is the corresponding g-factor. When a uniform magnetic field, whose strength $B_0$, the Hamiltonian operator will be as in the equation (2.1), and energy eigenvalues will be proportional to the eigenvalues of the spin operator $m$:

$$E_m = m\gamma\hbar B_0. \tag{2.7}$$

The application of a magnetic field towards spins results in a phenomenon called Zeeman splitting. When there is no magnetic field, the spins remain in the same (degenerate) energy level. However, under the magnetic field the energy levels split into the quantized energy levels corresponding to the $m$ values. These energy levels are called Zeeman levels.

The spin quantum numbers ($m$) are restricted by the orbital angular momentum eigenvalues ($l$) in a way that they can be between $-l$ and $l$ with increasing in integer numbers.

---

[1] It is a convention to choose the direction of the magnetic field in laboratory to be positive z-axis and in this thesis this choice is valid in all calculations unless it is mentioned otherwise.

For instance, for proton and electron, the orbital quantum number is $1/2$ therefore $m$ can be $-1/2$ or $1/2$ and corresponding energy of the values can be $E_{\pm} = \pm 1/2 \gamma \hbar B_0$.

As in the classical description, the energy can be written in terms of the Larmor frequencies, using the definition $\omega_0 = -\gamma_I B_0$. The energy difference between the states will be:

$$\Delta E = -\gamma_I \hbar B_0 = \hbar \omega_0. \tag{2.8}$$

Note that there is a linear relationship between the applied magnetic field and the frequency of the energy difference between states.

If we return to the classical picture, we can think of the spins as arrows pointing in all directions. When the magnetic field applied, the magnetic field forces spins to align with itself. Some of the spins will align parallel to the magnetic field and some will align anti-parallel. In the quantum counterpart of this picture, this event becomes as the some spins will be on the lower energy level (parallel) and some on the higher energy level (anti-parallel).

In equilibrium, the populations of the spins on each energy level are distributed according to Boltzmann statistics. Therefore number of the spins in the $(+)$ or $(-)$ states are related by the Boltzmann factors:

$$n_+ = n_- \mathrm{e}^{-\frac{E_+ - E_-}{k_B T}}, \tag{2.9}$$

where $k_{\mathrm{B}}$ is the Boltzmann constant and $T$ is the temperature.

The sample under the experimental interest, involves immense number of spins, i.e., on the order of Avogadro number. Since some of the spins will be in the up direction and some down direction, total bulk magnetization will be proportional to the difference of up and down populations. Here we define a quantity for this difference, called polarization:

$$P = \frac{n_+ - n_-}{n_+ + n_-} = \tanh\left(\frac{E_+ - E_-}{k_{\mathrm{B}} T}\right). \tag{2.10}$$

The direction of the net magnetization due to the choice of magnetic field in z-axis, is in the z-direction and this magnetization is called longitudinal magnetization. The time that the longitudinal magnetization returns to its equilibrium position is denoted with $T_1$. In NMR experiment, a secondary oscillating field in the radio-frequency band (RF) transmitted into the sample in the horizontal direction. This field has same or in the vicinity of the frequency as the Larmor frequency of the corresponding magnetic field and the gyromagnetic ratio of the nuclear spin. When RF pulse is transmitted, the magnetization vector can be tilted away from the z-axis and ensure that it makes a precessional motion about applied the z-axis. For this reason, these experiment are called magnetic resonance experiments, because the precessional motion is achieved by a resonant irradiation. The process of a secondary electromagnetic field is similarly performed on the ESR experi-

ment, however, the frequency of the transmitted pulse for electron is on the microwave frequency region and the Larmor frequency corresponding to the electron spin is much larger than the nuclear spin $\omega_S \gg \omega_I$.

Thus, the polarization is the main factor that determines the intensity of the magnetization and in this respect, the intensity of the NMR signals. The polarization given in the equation (2.10), depends on the energy difference between the (+) and (-) states and also inversely proportional to the temperature. Hence, one expects that the intensity of the signal decreases with the increasing temperature. And since the energy difference, $\Delta E = \gamma_I \hbar B_0$, depends on the magnetic field intensity, as the field is elevated, the polarization increases. On the other hand, gyromagnetic ratio, which is not an experimental input, directly affects the polarization.

In order to gain an insight about the degree of the polarizations that NMR and ESR can provide, polarization for a variety of nuclei and electron spins are given in the Table 2.1. An average magnetic field intensity of the current technological devices (3 T) and the room temperature (300 K) are assumed.

Table 2.1: Polarizations of various nuclear spins and electron spin are listed.

| Spin | Natural Abundance | $\gamma$ | $\gamma/\gamma_{\text{electron}}$ | P (%) |
|------|-------------------|----------|-----------------------------------|-------|
| $^1$H | 99.8 | 42.58 | 658 | 0.0010 |
| $^{13}$C | 1.07 | 10.71 | 2616 | 0.0002 |
| $^{14}$N | 99.63 | 3.077 | 9108 | 0.0001 |
| $^{17}$O | 0.038 | $-5.77$ | 4857 | 0.0001 |
| $^{31}$P | 100 | 17.24 | 1625 | 0.0004 |
| electron | | $-28024.95$ | 1 | 0.6700 |

The polarizations of nuclear spins, together with their low gyromagnetic ratios, seem to be minuscule compared to the polarization of the electron. In addition, the carbon nuclei suffers from the low natural abundance, that is only the 1% of the carbons posses spin 1/2. Therefore, we expect the outcome of the NMR experiments will be much smaller compared to that of the ESR experiments. In the NMR, small amount of magnetization is generally suppressed by the contribution of the other random motions in the sample making it undetectable. For this reason, the experiment should be performed several times to decrease the signal to noise ratio and isolate the targeted magnetization. The ESR experiment, on the other hand, produces much better results due to its much larger polarization. From the gyromagnetic ratios, it is seen that the electron polarization is ∼660 times larger than $^1$H and ∼2600 times than $^{13}$C polarization.

Now if we somehow alter these equilibrium polarizations, we can increase the NMR signal intensity [8]:

$$P = \frac{n_+ - n_-}{n_+ + n_-} = \frac{\langle I_z \rangle}{I_z^{\text{eq}}} \tanh\left(\frac{E_+ - E_-}{k_{\text{B}} T}\right), \qquad (2.11)$$

where $I_z^{\text{eq}}$ is the equilibrium polarization. The techniques that achieve this elevation are called hyperpolarization tecniques. In liquids, Overhauser Dynamic Nuclear Polarization, which is the main focus of this thesis, offer an enhancement as much as the ratio between the gyromagnetic ratios of electron and nuclear spins. This phenomenon is effective when both nuclear and electron spins exist in the sample and by manipulating the electron spins via tertiary MW irradiation, the enhancement of the NMR signals can be achieved. The interaction between the electron and nuclear spins is governed by a relaxation mechanism. In the next chapter this phenomenon will be summarized.

## 2.2. Relaxation

### 2.2..1 Phenomenological equations of relaxation

Relaxation mechanisms are fundamental in all magnetic resonance experiments. As definition, it refers to the process of the returning to the equilibrium position. Since in NMR experiments, the applied uniform magnetic field cause the magnetization vector of the nuclear spins ($I_z$) to align with its direction, relaxation refers to the time evolution of the magnetization vector returning to its equilibrium position. The process for a single type nuclear spin is represented by the differential equation:

$$\frac{\mathrm{d}I_z}{\mathrm{d}t} = -\frac{1}{T_1^0}(I_z - I_z^{\text{eq}}), \tag{2.12}$$

where $T_1^0$ characterizes the time that $I_z$ returns to the equilibrium.

If the sample also contains electron spins, then the relaxation equation involves an additional relaxation time:

$$\frac{\mathrm{d}I_z}{\mathrm{d}t} = -\left(\frac{1}{T_1^0} + \frac{1}{T_1^{II}}\right)(I_z - I_z^{\text{eq}}), \tag{2.13}$$

where $T_1^{II}$ comes from the electron-spin interactions. If the electrons are also taken out of the equilibrium by irradiating with a microwave field, then an additional term $T_1^{IS}$ comes into the picture:

$$\frac{\mathrm{d}I_z}{\mathrm{d}t} = -\left(\frac{1}{T_1^0} + \frac{1}{T_1^{II}}\right)(I_z - I_z^{\text{eq}}) - \frac{1}{T_1^{IS}}(S_z - S_z^{\text{eq}}), \tag{2.14}$$

where $T_1^{IS}$ arises from the out-of-equilibrium state of the electron spins.

### 2.2..2 Enhancement due to Overhauser Effect

Magnitude of the effect by ODNP process is related to the these additional relaxation terms. In this section, I will carry the calculations to obtain the enhancement due to
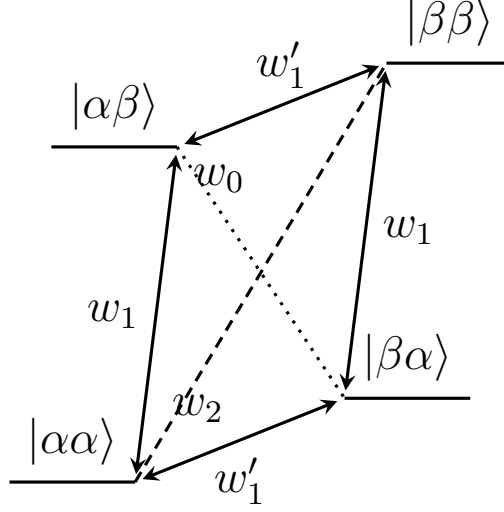
Figure 2.1: Energy levels representing nuclear and electron coupled spin system. $\alpha$ and $\beta$ represent lower and higher energy levels,respectively.

Overhauser effect.

The system containing both $1/2$ nuclear spin and electron spin can be described by the energy level diagram shown in the Fig. 2.1. The transitions between the energy levels are designated with $w$. While $w_1$ and $w_1'$ denote single excitations for nuclear and electron spins, respectively, $w_0$ and $w_2$ denote zero and double excitations. The evolution of the spin-state populations can be described in terms of the transition probabilities by the following differential equations [27]:

$$
\begin{aligned}
\frac{dn_{\beta\beta}}{dt} &= -(w_1 + w_1' + w_2)n_{\beta\beta} + w_1 n_{\alpha\beta} + w_1' n_{\beta\alpha} + w_2 n_{\alpha\alpha} + \text{cst.}, \\
\frac{dn_{\beta\alpha}}{dt} &= -(w_1 + w_1' + w_0)n_{\beta\alpha} + w_1 n_{\alpha\alpha} + w_1' n_{\beta\beta} + w_0 n_{\alpha\beta} + \text{cst.}, \\
\frac{dn_{\alpha\beta}}{dt} &= -(w_1 + w_1' + w_0)n_{\alpha\beta} + w_1 n_{\beta\beta} + w_1' n_{\alpha\alpha} + w_0 n_{\beta\alpha} + \text{cst.}, \\
\frac{dn_{\alpha\alpha}}{dt} &= -(w_1 + w_1' + w_2)n_{\alpha\alpha} + w_1 n_{\beta\alpha} + w_1' n_{\alpha\beta} + w_2 n_{\beta\beta} + \text{cst..}
\end{aligned}
\tag{2.15}
$$

Since the macroscopic magnetization is proportional to the vector sum of the magnetization, we have the relations:

$$
\begin{aligned}
I_z &\propto n_{\beta\beta} + n_{\beta\alpha} - n_{\alpha\beta} - n_{\alpha\alpha}, \\
S_z &\propto n_{\beta\beta} + n_{\alpha\beta} - n_{\beta\alpha} - n_{\alpha\alpha}.
\end{aligned}
\tag{2.16}
$$

If we differentiate the equation (2.16), together with the equation (2.15), we obtain:

$$
\begin{aligned}
\frac{dI_z}{dt} &= 2\{(w_1 + w_2)(n_{\beta\beta} - n_{\alpha\alpha}) + (w_0 + w_1)(n_{\beta\alpha} - n_{\alpha\beta})\}, \\
\frac{dS_z}{dt} &= 2\{(w_1' + w_2)(n_{\beta\beta} - n_{\alpha\alpha}) + (w_0 + w_1')(n_{\alpha\beta} - n_{\beta\alpha})\}.
\end{aligned}
\tag{2.17}
$$

9

Applying addition or subtraction of the equations in (2.16), finally we get the differential equations for $I_z$ and $S_z$:

$$\frac{dI_z}{dt} = -(w_0 + 2w_1 + w_2)(I_z - I_z^{\text{eq}}) - (w_2 - w_0)(S_z - S_z^{\text{eq}}),$$

$$\frac{dS_z}{dt} = -(w_0 + 2w_1' + w_2)(S_z - S_z^{\text{eq}}) - (w_2 - w_0)(I_z - I_z^{\text{eq}}),$$

(2.18)

where the $I^{\text{eq}}$ and $S^{\text{eq}}$ terms represent the equilibrium values of nuclear and electron magnetizations and can be correspondent of the constants in the equation (2.15). Since electron spin has a much stronger relaxation mechanism than the relaxation due to coupling with nuclear spin, relaxation times in differential equation of $S_z$ is negligible. Here the self- and cross-relaxation times for $I_z$ given in equation (2.14) can be written in terms of these transition probabilities. We define the relaxation rates $\rho_I^S$ and $\sigma_I^S$, which are the inverse of the corresponding relaxation times:

$$\frac{1}{T_1^{II}} = \rho_I^S = w_0 + 2w_1 + w_2,$$

(2.19)

and

$$\frac{1}{T_1^{IS}} = \sigma_I^S = w_2 - w_0.$$

(2.20)

If we include the relaxation rate in the absence of the electronic spin $w^t = 1/T_1^0$ then we revise the relaxation equation for $I_z$ in (2.18) as:

$$\frac{dI_z}{dt} = -(w_0 + 2w_1 + w_2 + w^t)(I_z - I_z^{\text{eq}}) - (w_2 - w_0)(S_z - S_z^{\text{eq}}).$$

(2.21)

At the steady state this equation becomes:

$$0 = -(w_0 + 2w_1 + w_2 + w^t)(I_z - I_z^{\text{eq}}) - (w_2 - w_0)(S_z - S_z^{\text{eq}})$$

(2.22)

Since we are interested in the deviation of magnetization vector from its static value (equation (2.11)), the enhancement factor is defined as:

$$e = \frac{I_z - I_z^{\text{eq}}}{I_z^{\text{eq}}}.$$

(2.23)

The equation (2.22) can be arranged as:

$$e = \frac{(I_z - I_z^{\text{eq}})}{I_z^{\text{eq}}} = \frac{w_2 - w_0}{(w_0 + 2w_1 + w_2 + w^t)} \frac{(S_z - S_z^{\text{eq}})}{I_z^{\text{eq}}}.$$

(2.24)

We rewrite this equation in the following form:

$$e = \frac{w_2 - w_0}{(w_0 + 2w_1 + w_2)} \frac{(w_0 + 2w_1 + w_2)}{(w_0 + 2w_1 + w_2 + w^t)} \frac{(S_z - S_z^{\text{eq}})}{S_z^{\text{eq}}} \frac{S_z^{\text{eq}}}{I_z^{\text{eq}}}.$$

(2.25)

10

The first term in the right hand side:

$$c = \frac{w_2 - w_0}{(w_0 + 2w_1 + w_2)},$$ (2.26)

represents the coupling factor. The reason to separate these transition probabilities is to define a quantity that comes from only electron-nuclear spin interactions by excluding the intrinsic relaxation rate $w^t$. Using the definitions in (2.19) and (2.20), we obtain this form:

$$c = \frac{\sigma_I^S}{\rho_I^S}.$$ (2.27)

The second term in equation (2.25) represents the leakage factor and it is the ratio between the relaxation rates in the absence and presence of the electron spin:

$$f = \frac{\rho_I^S}{\rho_I^S + w^t} = 1 - \frac{T_1^{II}}{T_1}.$$ (2.28)

As the value of the $T_1^{II}$ becomes negligible compared to $T_1$, this quantity becomes unity. The third term is defined as the electronic spin saturation factor:

$$s = \frac{(S_z - S_z^{eq})}{S_z^{eq}},$$ (2.29)

and it quantifies the difference of the electron spin populations. When the value $\langle S_z \rangle$ becomes zero, namely, the spin populations are distributed along the energy levels equally, the saturation factor becomes unity. The last term is the ratio of the magnetizations of electron and nuclear spins in the equilibrium. As the magnetizations are directly related to the gyromagnetic ratios, we obtain:

$$\frac{S_z^{eq}}{I_z^{eq}} = \frac{\gamma_S}{\gamma_I}.$$ (2.30)

Combining all these equations we define the enhancement factor in terms of these parameters:

$$e = cfs\frac{\gamma_S}{\gamma_I}.$$ (2.31)

## 2.2..3   Three-spin Effect

This derivation can be applied to all types of the nuclei individually. However, when the sample consist of two types of nuclear spins simultaneously, in addition to the electron spin, the relaxation equation includes the contribution from the interaction between those nuclear spins as well. When such interaction is present between different nuclear spin species denoted by $I$ and $K$, the relaxation of the longitudinal spin polarization of $I$ can

be expressed as in [8]:

$$\frac{dI_z}{dt} = -(\rho_I^S + \rho_I^K + w^t)(I_z - I_z^0) - \sigma_I^S(S_z - S_z^0) - \sigma_I^K(K_z - K_z^0) \quad (2.32)$$

where the self- and cross-relaxation rates $\rho_I^K$ and $\sigma_I^K$ which are due to the coupling between $I$ and $K$ are introduced.

As in the case of two spins, we seek the steady state solutions. Assuming the polarization of $I$ does not affect polarization of $K$, using the steady state of (2.32), the enhancement of the $I$ signal, $e_I = (I - I^0)/I^0$, becomes:

$$e_I = \frac{\sigma_I^S - \sigma_I^K c_K^S f_K^S}{\rho_I^S + \rho_I^K + w^t} s \frac{\gamma_S}{\gamma_I}, \quad (2.33)$$

where $c_K^S$ is the coupling factor of interaction between $K$ and $S$, $f_K^S$ is the leakage factor of for nuclear spin $K$. In terms of coupling factor for $I$, $c_I^S = \sigma_I^S/\rho_I^S$ and leakage factor for $I$, $f_I^S = \rho_I^S/(\rho_I^S + \rho_I^K + w_I)$, equation (2.33) reads:

$$e_I = (m\, c_I^S) f_I^S s \frac{\gamma_S}{\gamma_I}, \quad (2.34)$$

where

$$m = 1 - \frac{\sigma_I^K}{\sigma_I^S}(c_K^S f_K^S), \quad (2.35)$$

is a multiplicative correction to the coupling factor of $I$ that accounts for the additional interaction between $I$ and $K$.

## 2.3. Review to the Bloch-Wangness-Redfield Relaxation Theory

The relaxation rates are evaluated as the combinations of the transition probabilities in the previous section. However, these rates can also be obtained in terms of the spectral density functions (SDFs), through an analysis of a second-order time-dependent perturbation theory. The formal derivation for this can be found in numerous references in detail [28, 29, 30]. In this section, I will carry the formalism in these textbooks, by first deriving a general formulation for the time evolution of a spin system under time-independent and time-dependent interactions and then proceed to the specific cases of the interactions involved in Overhauser effect.

### 2.3..1 General Formalism

The formalism for a relaxing spin system weakly coupled to a lattice can be derived through time-dependent perturbation theory. The treatment starts with the assumption that

12

Hamiltonian of the spin system can be decomposed into time-independent and weak time-dependent parts. The time-independent part may involve any stationary non-fluctuating interactions such as Zeeman interaction which spins couple to the applied strong uniform magnetic field or chemical shift which arises from the electronic configuration of the atoms in the molecules etc. The time-independent part may involve weaker stochastic interactions such as dipolar, scalar or quadrupolar couplings in which spins are coupled with each other or chemical shift anisotropy which can be attributed to the anisotropic orientation tendency of the chemical shift.

Let the time-independent and stochastically fluctuating Hamiltonians be $\mathcal{H}_0$ and $\mathcal{H}_1(t)$, respectively. Then Hamiltonian of the system becomes:

$$\mathcal{H}_{\text{sys}} = \mathcal{H}_0 + \mathcal{H}_1(t). \tag{2.36}$$

By definition ensemble average (or time average assuming the ergodic hypothesis) of the time-dependent part is zero:

$$\overline{\mathcal{H}_1(t)} = 0. \tag{2.37}$$

The quantum mechanical description for the ensemble of spins is characterized by the density operator $\rho$. The evolution of the density operator is given by Liouville/von Neumann equation:

$$\frac{\mathrm{d}\rho}{\mathrm{d}t} = -i[\mathcal{H}_{\text{sys}}, \rho], \tag{2.38}$$

where Hamiltonian is divided by $\hbar$ and from now on we stick with this convention. Since the time-independent part of the Hamiltonian does not involve in the relaxation mechanism, working on the so-called rotating frame (or interaction frame) is convenient. Rotating frame does not correspond to physical rotation but the action of transforming into interaction picture resembles the action of rotation. The transformation to the interaction picture is performed by the unitary operator:

$$U = \mathrm{e}^{-i\mathcal{H}_0 t}. \tag{2.39}$$

The unitary operator is acted upon all the observables and therefore the time-dependent part of the interactions will be isolated from other effects:

$$\begin{aligned} \hat{\rho} &= U^{-1}\rho U, \\ \hat{\mathcal{H}}_{\text{sys}} &= U^{-1}\mathcal{H}_{\text{sys}}U, \end{aligned} \tag{2.40}$$

where the hat above the operators denotes interaction picture. The equation of motion is moved to the interaction representation as well:

$$\frac{\mathrm{d}[U\hat{\rho}U^{-1}]}{\mathrm{d}t} = -i[U\hat{\mathcal{H}}_{\text{sys}}U^{-1}, U\hat{\rho}U^{-1}, \tag{2.41}$$

13

which can be written as:

$$\frac{\mathrm{d}[U\hat{\rho}U^{-1}]}{\mathrm{d}t} = -iU[\hat{\mathcal{H}}_0 + \hat{\mathcal{H}}_1(t), \hat{\rho}]U^{-1}. \tag{2.42}$$

Using the Baker-Campbell-Handsdorff formula:

$$U\hat{\mathcal{H}}_0U^{-1} = \mathrm{e}^{-i\mathcal{H}_0 t}\hat{\mathcal{H}}_0\mathrm{e}^{i\hat{\mathcal{H}}_0 t} = \hat{\mathcal{H}}_0 + i[\hat{\mathcal{H}}_0, \hat{\mathcal{H}}_0] - [\hat{\mathcal{H}}_0, [\hat{\mathcal{H}}_0, \hat{\mathcal{H}}_0]] + ... = \hat{\mathcal{H}}_0, \tag{2.43}$$

so that the time-independent Hamiltonian remains same in the interaction picture and therefore, $\mathcal{H}_0$ commutes with $U$. The left hand side of the equation (2.42) can be evaluated as:

$$\begin{aligned}
\frac{\mathrm{d}[U\hat{\rho}U^{-1}]}{\mathrm{d}t} &= \frac{\mathrm{d}[U]}{\mathrm{d}t}\hat{\rho}U^{-1} + U\frac{\mathrm{d}\hat{\rho}}{\mathrm{d}t}U^{-1} + U\hat{\rho}\frac{\mathrm{d}[U^{-1}]}{\mathrm{d}t}, \\
&= -i\mathcal{H}_0 U\hat{\rho}U^{-1} + U\frac{\mathrm{d}\hat{\rho}}{\mathrm{d}t}U^{-1} + iU\hat{\rho}\mathcal{H}_0 U^{-1}, \\
&= iU[\hat{\rho}, \mathcal{H}_0]U^{-1} + U\frac{\mathrm{d}\hat{\rho}}{\mathrm{d}t}U^{-1},
\end{aligned} \tag{2.44}$$

and the right hand side of (2.42) is:

$$= -iU[\hat{\mathcal{H}}_0, \hat{\rho}]U^{-1} - iU[\hat{\mathcal{H}}_1(t), \hat{\rho}]U^{-1}. \tag{2.45}$$

First terms on both sides cancel each other. Removing the outer $U$ operators, the equation of motion becomes:

$$\frac{\mathrm{d}\hat{\rho}}{\mathrm{d}t} = -i[\hat{\mathcal{H}}(t), \hat{\rho}]. \tag{2.46}$$

The solution to this equation is carried on by an iterative method. Starting with the integral:

$$\hat{\rho}(t) = \hat{\rho}(0) - i\int_0^t \mathrm{d}t'[\hat{\mathcal{H}}(t'), \hat{\rho}(t')], \tag{2.47}$$

where we invoke the zeroth order approximation $\hat{\rho}(t) \approx \hat{\rho}(0)$. Putting this on the inside the integral in (2.47), we get:

$$\hat{\rho}(t) = \hat{\rho}(0) - i\int_0^t \mathrm{d}t'[\hat{\mathcal{H}}(t'), \hat{\rho}(0)], \tag{2.48}$$

and reinstering the equation (2.48) to the inside of integral in (2.47), we get:

$$\hat{\rho}(t) = \hat{\rho}(0) - i\int_0^t \mathrm{d}t'[\hat{\mathcal{H}}(t'), \hat{\rho}(0) - \int_0^{t'} \mathrm{d}t''[\hat{\mathcal{H}}(t''), \hat{\rho}(0)]]. \tag{2.49}$$

Differentiating this equation:

$$\frac{\mathrm{d}\hat{\rho}(t)}{\mathrm{d}t} = -i[\hat{\mathcal{H}}(t'), \hat{\rho}(0)] - \int_0^t \mathrm{d}t'[\hat{\mathcal{H}}(t), [\hat{\mathcal{H}}(t'), \hat{\rho}(0)]]. \tag{2.50}$$

We stop the iteration at the second order. Since the interactions occur between an ensemble of the spins, we take an ensemble average of the spin density operator.

$$\frac{\mathrm{d}\overline{\hat{\rho}(t)}}{\mathrm{d}t} = -i\overline{[\hat{\mathcal{H}}(t'), \hat{\rho}(0)]} - \int_0^t \mathrm{d}t' \overline{[\hat{\mathcal{H}}(t), [\hat{\mathcal{H}}(t'), \hat{\rho}(0)]]}. \tag{2.51}$$

Here we subject a change of variable $\tau = t - t'$.

$$\frac{\mathrm{d}\overline{\hat{\rho}(t)}}{\mathrm{d}t} = -i\overline{[\hat{\mathcal{H}}(t-\tau), \hat{\rho}(0)]} - \int_0^t \mathrm{d}\tau \overline{[\hat{\mathcal{H}}(t), [\hat{\mathcal{H}}(t-\tau), \hat{\rho}(0)]]}. \tag{2.52}$$

If the characteristic time of $\hat{\mathcal{H}}_1(t)$ is $\tau_c$, then the average of $\hat{\mathcal{H}}_1(t)$ and $\hat{\rho}$ can be taken independently. This is valid when the quantity of the macroscopic variable has a much slower decay than the scale of $\tau_c$. Therefore, we can drop the first term along with the condition given in (2.37). Consequence of having $t \gg \tau_c$ is that we can extend the upper integral to the infinity since it will not affect the value of the integral and the term inside of the integral $\hat{\rho}_0$ can be replaced with $\hat{\rho}(t)$:

$$\frac{\mathrm{d}\hat{\rho}(t)}{\mathrm{d}t} = -\int_0^\infty \mathrm{d}\tau \overline{[\hat{\mathcal{H}}(t), [\hat{\mathcal{H}}(t-\tau), \hat{\rho}(t)]]}, \tag{2.53}$$

where we omitted the bar over $\hat{\rho}(t)$ for convenience. Taking the lattice temperature into account we will introduce the equilibrium state density operator $\rho_0$ relying on the commutivity of $\rho_0$ with $\mathcal{H}_0$, then the expression in (2.53) becomes:

$$\frac{\mathrm{d}\hat{\rho}(t)}{\mathrm{d}t} = -\int_0^\infty \mathrm{d}\tau \overline{[\hat{\mathcal{H}}(t), [\hat{\mathcal{H}}(t-\tau), \hat{\rho}(t) - \hat{\rho}_0]]}. \tag{2.54}$$

Since we are concerned with the Overhauser effect, our Hamiltonian will consist of

$$\mathcal{H}_0 = \mathcal{H}_I + \mathcal{H}_S + \mathcal{H}_{\mathrm{dip}} + \mathcal{H}_{\mathrm{scalar}}, \tag{2.55}$$

where the first two terms are Zeeman interactions for nuclear and electron spins and they will be treated for time-independent interactions:

$$\mathcal{H}_0 = \mathcal{H}_I + \mathcal{H}_S = \omega_I I_z + \omega_S S_z, \tag{2.56}$$

where $\omega_I = -\gamma_I B_0$ and $\omega_S = -\gamma_S B_0$. The last two terms are stochastically varying dipolar and scalar interactions.

## 2.3..2 Dipolar Interaction

Classically, the dipolar interaction between two magnetic dipole is:

$$H_{\mathrm{dip}} = \frac{\mu_0}{4\pi}\left[\frac{\mu_1 \cdot \mu_2 - 3(\mu_1 \cdot \hat{r})(\mu_2 \cdot \hat{r})}{r^3}\right], \tag{2.57}$$

where $r$ is the distance vector between two magnetic dipoles and $\mu_0$ is the permittivity of free space. Quantum mechanical counterpart for dipolar interaction between the spins $I$ and $S$ is similarly:

$$\mathcal{H}_{\mathrm{dip}} = \frac{\mu_0}{4\pi}\gamma_I\gamma_S\hbar\left[\frac{I \cdot S - 3(I \cdot \hat{r})(S \cdot \hat{r})}{r^3}\right] = I \cdot \mathbf{D} \cdot S, \tag{2.58}$$

where $\mathbf{D}$ is the dipolar interaction tensor and we divided Hamiltonian by $\hbar$. Dipolar tensor is a second rank traceless tensor operator and can be decomposed into the linear combinations of orthonormal functions:

$$\mathcal{H}_{\mathrm{dip}} = \sum_\alpha F_\alpha A_\alpha = \sum_\alpha F_\alpha^* A_\alpha^\dagger, \tag{2.59}$$

where $F_\alpha$ denotes the stochastic random functions corresponding to the rotational dependence in the (2.58) and $A_\alpha$ denotes the spin operators. Hermiticity of the Hamiltonian gives rise to equality of the latter, where star (*) denotes complex conjugate and dagger (†) denotes Hermitian conjugate. The functions that constitute the dipolar tensor are given in the Table 2.2.

Table 2.2: Random functions $F_\alpha$ and $F_\alpha^*$, spin operators $A_\alpha^\beta$ and their hermitian conjugates and their corresponding frequencies in the interaction picture. The prefactor $\delta_{IS}$ is $\frac{\mu_0}{4\pi}\gamma_I\gamma_S\hbar$.

| $F_\alpha$ | $F_\alpha^*$ | $A_\alpha^\beta$ | $A_\alpha^{\beta\dagger}$ $(A_{-\alpha}^\beta)$ | $\omega$ |
|---|---|---|---|---|
| | | $\sqrt{\frac{2}{3}}I_zS_z$ | $\sqrt{\frac{2}{3}}I_zS_z$ | $0$ |
| $\sqrt{\frac{3}{2}}\delta_{IS}\frac{r^2-z^2}{r^5}$ | $\sqrt{\frac{3}{2}}\delta_{IS}\frac{r^2-z^2}{r^5}$ | $-\sqrt{\frac{1}{24}}I_+S_-$ | $-\sqrt{\frac{1}{24}}I_-S_+$ | $\omega_I - \omega_S$ |
| | | $-\sqrt{\frac{1}{24}}I_-S_+$ | $-\sqrt{\frac{1}{24}}I_+S_-$ | $-\omega_I + \omega_S$ |
| $3\delta_{IS}\frac{z(x-iy)}{r^5}$ | $3\delta_{IS}\frac{z(x+iy)}{r^5}$ | $-\frac{1}{2}I_+S_z$ | $-\frac{1}{2}I_-S_z$ | $\omega_I$ |
| | | $-\frac{1}{2}I_zS_+$ | $-\frac{1}{2}I_zS_-$ | $\omega_S$ |
| $\frac{3}{2}\delta_{IS}\frac{(x-iy)^2}{r^5}$ | $\frac{3}{2}\delta_{IS}\frac{(x+iy)^2}{r^5}$ | $-\frac{1}{2}I_+S_+$ | $-\frac{1}{2}I_-S_-$ | $\omega_I + \omega_S$ |

Note that the spin operators also decomposed into the smaller parts:

$$A_\alpha = \sum_\beta A_\alpha^\beta. \tag{2.60}$$

Consequently, the spin operators can be transformed to the interaction picture using $[\mathcal{H}_0, A_\alpha^\beta] =$

$\omega_\alpha^\beta A_\alpha^\beta$. In the interaction picture, the operators become:

$$\hat{A}_i^\beta = A_\alpha^\beta e^{-i\omega_\alpha^\beta t}, \tag{2.61}$$

where the values of $\omega_\alpha^\beta$ is given in Table 2.2. Therefore the dipolar Hamiltonian in the interaction picture becomes:

$$\hat{\mathcal{H}}_{\text{dip}}(t) = \sum_{\alpha,\beta} F_\alpha(\mathbf{r}(t))\hat{A}_\alpha^\beta e^{-i\omega_\alpha^\beta t}. \tag{2.62}$$

We impose these functions to the equation (2.54) we get:

$$\frac{\mathrm{d}\hat{\rho}(t)}{\mathrm{d}t} = -\int_0^\infty d\tau \sum_{\alpha,\beta}\sum_{\alpha',\beta'} \overline{[F_\alpha(t)\hat{A}_\alpha^\beta e^{-i\omega_\alpha^\beta t}, [F_{\alpha'}^*(t-\tau)\hat{A}_{\alpha'}^{\beta'\dagger} e^{-i\omega_{\alpha'}^{\beta'}(t-\tau)}}, \hat{\rho}(t)-\hat{\rho}_0]]. \tag{2.63}$$

If we assume the spatial part $F_\alpha$ and the spin operators are stochastically independent, then they can be averaged independently and the equation becomes:

$$\frac{\mathrm{d}\hat{\rho}(t)}{\mathrm{d}t} = -\sum_{\alpha,\beta}\sum_{\alpha',\beta'}\int_0^\infty d\tau \overline{F_\alpha(t)F_{\alpha'}^*(t-\tau)} e^{-i\omega_\alpha^\beta t} e^{-i\omega_{\alpha'}^{\beta'}(t-\tau)}[\hat{A}_\alpha^\beta, [\hat{A}_{\alpha'}^{\beta'\dagger}, \hat{\rho}(t)-\hat{\rho}_0]], \tag{2.64}$$

where we define the correlation function:

$$C_{\alpha,\alpha'}^{\text{dip}}(\tau) = \overline{F_\alpha(t)F_{\alpha'}^*(t-\tau)}. \tag{2.65}$$

Therefore we can rewrite the equation (2.64) as:

$$\frac{\mathrm{d}\hat{\rho}(t)}{\mathrm{d}t} = -\sum_{\alpha,\beta}\sum_{\beta'}\int_0^\infty d\tau C_\alpha^{\text{dip}}(\tau) e^{-i\omega_\alpha^\beta t} e^{-i\omega_\alpha^{\beta'}(t+\tau)}[\hat{A}_\alpha^\beta, [\hat{A}_\alpha^{\beta'\dagger}, \hat{\rho}(t)-\hat{\rho}_0]], \tag{2.66}$$

where we assumed that the the order of stochastic functions are independent, therefore we can invoke $C_{\alpha,\alpha'}^{\text{dip}}(\tau) = C_\alpha^{\text{dip}}(\tau)\delta_{\alpha,\alpha'}$ and also we applied the time reversibility of the correlation functions that is $C_\alpha^{\text{dip}}(t-\tau) = C_\alpha^{\text{dip}}(t+\tau)$. Now we can define the spectral density functions for dipolar interaction by:

$$J_\alpha^{\beta,\text{dip}}(\omega_\alpha^\beta) = \int_0^\infty d\tau C_\alpha^{\text{dip}}(\tau) e^{-i\omega_\alpha^\beta \tau}, \tag{2.67}$$

which is the Laplace-Fourier transform of the correlation function.

Expectation value of an observable can be found by $\langle Q \rangle = \text{Tr}\{Q\hat{\rho}\}$. Thus using the equation (2.66) and (2.67), we obtain the differential equation for the nuclear spin magnetization in z-direction, $I_z$:

$$\frac{\mathrm{d}\langle \hat{I}_z \rangle}{\mathrm{d}t} = -\operatorname{Tr}\left\{ \sum_{\alpha,\beta}\sum_{\beta'} J_\alpha^{\beta,\mathrm{dip}}(\omega_\alpha^\beta) \mathrm{e}^{-i(\omega_\alpha^\beta + \omega_\alpha^{\beta'})t)}[\hat{A}_\alpha^\beta, [\hat{A}_{\alpha'}^{\beta'\dagger}, \hat{\rho}(t) - \hat{\rho}_0]]I_z \right\}. \qquad (2.68)$$

We can rearrange this equation using the property of trace $\operatorname{Tr}[A,B] = \operatorname{Tr}[B,A]$:

$$\frac{\mathrm{d}\langle \hat{I}_z \rangle}{\mathrm{d}t} = -\operatorname{Tr}\left\{ (\hat{\rho}(t) - \hat{\rho}_0) \sum_{\alpha,\beta}\sum_{\beta'} J_\alpha^{\beta,\mathrm{dip}}(\omega_\alpha^\beta) \mathrm{e}^{-i(\omega_\alpha^\beta + \omega_\alpha^{\beta'})t)}[\hat{A}_\alpha^\beta, [\hat{A}_{\alpha'}^{\beta'\dagger}, I_z]] \right\}. \qquad (2.69)$$

The term $\mathrm{e}^{-i(\omega_\alpha^\beta + \omega_\alpha^{\beta'})t}$ is rapidly oscillating when compared to the characteristic time of relaxation, thus the exponent average to zero. Therefore equation (2.69) gives:

$$\frac{\mathrm{d}\langle I_z \rangle}{\mathrm{d}t} = -\sum_{\alpha,\beta}\sum_{\beta'} \operatorname{Tr}\left\{ (\hat{\rho}(t) - \hat{\rho}_0) J_\alpha^{\mathrm{dip}}(\omega_\alpha^\beta)[A_\alpha^\beta, [A_\alpha^{\beta'}, I_z]] \right\}. \qquad (2.70)$$

If we proceed to the spin operator part, the calculations of the commutator relations is necessary. However, in the calculations, we see that only non-vanishing terms are for $\alpha \neq 0$ and $\beta' = -\beta$; and for $\alpha = 0$, $\beta = 1$, $\beta' = 2$ and $\beta = 2$, $\beta' = 1$. Calculation of commutator relations yields the following results:

$$\begin{aligned}
[A_0^1, [A_0^2, I_z]] &= \frac{1}{12}(I_z S_+ S_- - I_+ I_- S_z), \\
[A_1^1, [A_{-1}^1, I_z]] &= \frac{1}{2} I_z S_z^2, \\
[A_2^1, [A_{-2}^1, I_z]] &= \frac{1}{2}(I_z S_- S_+ + S_z I_+ I_-),
\end{aligned} \qquad (2.71)$$

and their hermitian conjugates. We can convert the ladder operators into Cartesian coordinates:

$$\begin{aligned}
[A_0^1, [A_0^2, I_z]] &= \frac{1}{12}(I_z(S_x^2 + S_y^2) - (I_x^2 + I_y^2)S_z, \\
[A_1^1, [A_{-1}^1, I_z]] &= \frac{1}{2} I_z S_z^2, \\
[A_2^1, [A_{-2}^1, I_z]] &= \frac{1}{2}(I_z(S_x^2 + S_y^2 - S_z) + (I_x^2 + I_y^2 - I_z)S_z).
\end{aligned} \qquad (2.72)$$

To calculate the expectation values of these values we need to assume the high temperature approximation which produces the relation [30]:

$$\hat{\rho} \approx \rho \approx a + b(I_z + S_z), \qquad (2.73)$$

where a and b are constants. Thus we find:

$$\mathrm{Tr}\{\rho I_z S_z\} \approx \mathrm{Tr}\{(a + b(I_z + S_z))I_z S_z\} \approx 0,$$
$$\mathrm{Tr}\{\rho I_z S_i^2\} \approx \mathrm{Tr}\{(a + b(I_z S_z)I_z S_i^2)\} \approx \langle I_z \rangle \frac{S(S+1)}{3}. \tag{2.74}$$

Then the summation part of the differential equation becomes for $\alpha = 0$:

$$J_0^{\mathrm{dip}}(\omega_I - \omega_S)\left( -\frac{1}{9}I(I+1)(\langle I_z \rangle - \langle I_z \rangle_0) - \frac{1}{9}S(S+1)(\langle S_z \rangle - \langle S_z \rangle_0) \right), \tag{2.75}$$

for $\alpha = 1$:

$$J_1^{\mathrm{dip}}(\omega_I)\left( -\frac{1}{3} \right)I(I+1)(\langle I_z \rangle - \langle I_z \rangle_0), \tag{2.76}$$

and for $\alpha = 2$:

$$J_2^{\mathrm{dip}}(\omega_I + \omega_S)\left( -\frac{2}{3}I(I+1)\langle I_z \rangle - \langle I_z \rangle_0 + \frac{2}{3}S(S+1)\langle S_z \rangle - \langle S_z \rangle_0 \right). \tag{2.77}$$

Therefore the characteristic times of relaxation due to addition of electronic spin $T_1^{II}$ and $T_1^{IS}$ are related by:

$$\frac{1}{T_1^{II}} = \rho_I^S = I(I+1)\left( \frac{1}{9}J_0^{\mathrm{dip}}(\omega_I - \omega_S) + \frac{1}{3}J_1^{\mathrm{dip}}(\omega_I) + \frac{2}{3}J_2^{\mathrm{dip}}(\omega_I + \omega_S) \right),$$
$$\frac{1}{T_1^{IS}} = \sigma_I^S = S(S+1)\left( \frac{2}{3}J_2^{\mathrm{dip}}(\omega_I + \omega_S) - \frac{1}{9}J_0^{\mathrm{dip}}(\omega_I - \omega_S) \right). \tag{2.78}$$

Considering $I$ and $S$ corresponds to the nuclear and electron spins, and the nuclear spins that are in the focus of this thesis have the spin quantum number $1/2$, we evaluate the equation (2.78):

$$\rho_I^S = \frac{1}{12}J_0^{\mathrm{dip}}(\omega_I - \omega_S) + \frac{1}{4}J_1^{\mathrm{dip}}(\omega_I) + \frac{1}{2}J_2^{\mathrm{dip}}(\omega_I + \omega_S),$$
$$\sigma_I^S = \frac{1}{2}J_2^{\mathrm{dip}}(\omega_I + \omega_S) - \frac{1}{12}J_0^{\mathrm{dip}}(\omega_I - \omega_S). \tag{2.79}$$

Therefore acknowledging $J_\alpha(\omega) = J_\alpha(-\omega)$ and $\omega_S \gg \omega_I$ and assuming the isotropicity of the molecular motions which makes all $J_\alpha$ equal in average, the equations in (2.79) can be approximated as:

$$\rho_I^S \approx \frac{1}{12}(7J(\omega_S) + 3J(\omega_I))$$
$$\sigma_I^S \approx \frac{1}{12}(5J(\omega_S)). \tag{2.80}$$

Related to the relaxation rate, a quantity NMR experiments measure called relaxivity $r_I^S$ and it removes the concentration dependence of the self-relaxation rate. Therefore the

relaxivity due to dipolar coupling is found division of the self-relaxation rates by the concentration of electron spins ($N_S$):

$$r_I^S = \frac{\rho_I^S}{N_S}. \tag{2.81}$$

Lastly, the coupling factor influenced by only dipolar coupling can be written in terms of the spectral density functions:

$$c \approx \frac{5(J_{\omega_S})}{7J(\omega_S) + 3J(\omega_I)} \tag{2.82}$$

### 2.3..3 Scalar Interaction

Different from the dipolar interaction, the scalar interaction does not depend on the direction of the inter-spin vector. Scalar interaction arises from the Fermi contact interaction and it is directly proportional to the electron spin density at the location of the nuclear spin and only the magnitude of the de-localization is related the interaction. This magnitude is called hyperfine contact coupling constant or Fermi contact and because of its independence of direction it is denoted as $A_{\mathrm{iso}}$. The Hamiltonian for scalar interaction is:

$$\mathcal{H}_{\mathrm{scalar}} = A_{\mathrm{iso}} I \cdot S. \tag{2.83}$$

Applying the same treatment, we expand $I \cdot S$ into corresponding ladder operators and $I_z$:

$$\mathcal{H}_{\mathrm{scalar}} = A_{\mathrm{iso}}(I_z S_z + \frac{1}{2} I_+ S_- + \frac{1}{2} I_- S_+), \tag{2.84}$$

which becomes in the interaction picture:

$$\hat{\mathcal{H}}_{\mathrm{scalar}} = A_{\mathrm{iso}}(t)(I_z S_z + \frac{1}{2} I_+ S_- \mathrm{e}^{-i(\omega_I - \omega_S)t} + \frac{1}{2} I_- S_+ \mathrm{e}^{-i(-\omega_I + \omega_S)t}). \tag{2.85}$$

Rewriting the equation (2.85) as a summation:

$$\hat{\mathcal{H}}_{\mathrm{scalar}} = A_{\mathrm{iso}}(t) \sum_\gamma A_\gamma \mathrm{e}^{-i\omega_\gamma t} = A_{\mathrm{iso}}(t) \sum_\gamma A_\gamma^\dagger \mathrm{e}^{i\omega_\gamma t} \tag{2.86}$$

Here we also assume the stochasticity of the hyperfine coupling constant that is $\overline{A_{\mathrm{iso}}} = 0$. Similar to the dipolar case, we obtain the differential equation:

$$\frac{\mathrm{d}\hat{\rho}(t)}{\mathrm{d}t} = -\int_0^\infty d\tau \sum_{\gamma,\gamma'} \overline{[A_{\mathrm{iso}}(t) A^\gamma \mathrm{e}^{-i\omega^\gamma t}, [A_{\mathrm{iso}}(t-\tau) A^{\gamma'} \mathrm{e}^{-i\omega^\gamma(t-\tau)}}, \hat{\rho}(t) - \hat{\rho}_0]]. \tag{2.87}$$

Using same assumption that the hyperfine coupling constant and the spin operators are stochastically independent, we rewrite:

$$\frac{\mathrm{d}\hat{\rho}(t)}{\mathrm{d}t} = -\int_0^t d\tau \sum_{\gamma,\gamma'} \overline{A_{\mathrm{iso}}(t)A_{\mathrm{iso}}(t-\tau)}\mathrm{e}^{-i\omega^\gamma t}\mathrm{e}^{-i\omega^{\gamma'}(t-\tau)}[A^\gamma,[A^{\gamma'},\hat{\rho}(t)-\hat{\rho}_0]]. \quad (2.88)$$

Then we define the correlation function for scalar interaction:

$$C^{\mathrm{iso}}(\tau) = \overline{A_{\mathrm{iso}}(t)A_{\mathrm{iso}}(t-\tau)}, \quad (2.89)$$

and the scalar spectral density function:

$$K^{\mathrm{iso}}(\omega^\gamma) = \int_0^\infty C^{\mathrm{iso}}(\tau)\mathrm{e}^{-i\omega^\gamma}d\tau, \quad (2.90)$$

Then the differential equation in (2.88) becomes:

$$\frac{\mathrm{d}\hat{\rho}(t)}{\mathrm{d}t} = -\sum_{\gamma,\gamma'} K^{\mathrm{iso}}(\omega^\gamma)\mathrm{e}^{-i(\omega^\gamma+\omega^{\gamma'})t}[A^\gamma,[A^{\gamma'},\hat{\rho}(t)-\hat{\rho}_0]]. \quad (2.91)$$

Again we assume, because of the rapid oscillations exponential terms become unity. Thus the expectation value for $I_z$ becomes:

$$\frac{\mathrm{d}I_z(t)}{\mathrm{d}t} = -\mathrm{Tr}\left\{(\hat{\rho}(t)-\hat{\rho}_0)\sum_{\gamma,\gamma'} K^{\mathrm{iso}}(\omega^\gamma)[A^\gamma,[A^{\gamma'},I_z]]\right\}. \quad (2.92)$$

If we do the commutator calculations, we see that only non-vanishing terms are:

$$[A^1,[A^{-1},I_z]] = I_z(S_x^2+S_y^2) + S_z(I_x^2+I_y^2) \quad (2.93)$$

and its complex conjugate. Then the traces produce:

$$\begin{aligned}\frac{\mathrm{d}\langle I_z\rangle}{\mathrm{d}t} = &-\frac{8}{3}I(I+1)K(\omega_I-\omega_S)\big(\langle I_z\rangle-\langle I_z\rangle_0\big)\\ &+\frac{8}{3}S(S+1)K(\omega_I)-\omega_S\big)\big(\langle S_z\rangle-\langle S_z\rangle_0\big)\end{aligned} \quad (2.94)$$

and relaxation rates $T_1^{II}$ and $T_1^{IS}$ for scalar interaction becomes:

$$\begin{aligned}\frac{1}{T_1^{II}} &= \frac{8}{3}I(I+1)K(\omega_I-\omega_S)\\ \frac{1}{T_1^{IS}} &= -\frac{8}{3}S(S+1)K(\omega_I-\omega_S)\end{aligned} \quad (2.95)$$

As in dipolar case, we can use approximation of $\omega_S \gg \omega_I$ and using $I = 1/2$ and $S = 1/2$ we get:

$$\rho_I^S \approx \frac{1}{2}K(\omega_S), \sigma_I^S \approx -\frac{1}{2}K(\omega_S) \qquad (2.96)$$

Combining the relaxation rates for scalar and dipolar interactions we get:

$$\rho_I^S \approx \frac{1}{12}\big(7J(\omega_S) + 3J(\omega_I) + 6K(\omega_S)\big), \qquad (2.97)$$

and

$$\sigma_I^S \approx \frac{1}{12}\big(5J(\omega_S) - 6K(\omega_S)\big). \qquad (2.98)$$

The coupling factor influenced by both scalar and dipolar relaxations becomes:

$$c \approx \frac{5J(\omega_S) - 6K(\omega_S)}{7J(\omega_S) + 3J(\omega_I) + 6K(\omega_S)}. \qquad (2.99)$$

## 2.4.  Spectral density functions from simulations

The time correlation functions of the inter-spin vectors between spins can be obtained using the molecular dynamics (MD) simulations which follow the trajectory of the atoms in time. In this section, I will briefly explain basic principles of MD simulations and the methodology to extract the spectral density functions from simulations.

### 2.4..1  MD Simulations

MD simulations follow purely classical Newtonian equations of motion for a system of $N$ atoms. For instance, simulations that were carried out in this thesis have approximately $\sim 25\,000$ atoms. The equation of motion for each atom is:

$$m_i \ddot{\mathbf{r}}_i = F_i, \qquad (2.100)$$

where $m_i$ is the atomic mass, $\mathbf{r}_i$ is the position vector and $F_i$ is the force acting upon the atom. Force is the space derivative of the interatomic potential energy:

$$F_i = -\nabla V_i, \qquad (2.101)$$

where $V_i(\mathbf{r_1}, \mathbf{r_2}, ..., \mathbf{r_N}, )$ is called the Force Field and it is a function of positions of $N$ atoms. The Force Field consists of bonded interactions where two, three or four atoms

are connected by harmonic springs and non-bonded interactions which involve the van der Waals and electrostatic interactions.

The trajectory of the atoms is obtained by calculating the force and thus acceleration in each time step. Velocity and position of the atoms can be calculated by integration of acceleration once and twice, respectively. Since analytical integration is impossible for an ensemble of system, numerical integration is necessary to solve the equation of motion. Commonly used integration algorithm in MD simulations is Verlet algorithm. It is based on the Taylor expansion of $\mathbf{r}(t)$ at times $t + \delta t$ and $t - \delta t$ up to the 3rd order:

$$
\begin{aligned}
\mathbf{r}(t + \delta t) &= \mathbf{r}(t) + \dot{\mathbf{r}}(t)\delta t + \frac{1}{2}\ddot{\mathbf{r}}(t)\delta t^2 + \frac{1}{6}\dddot{\mathbf{r}}(t)\delta t^3 + O(\delta t^4), \\
\mathbf{r}(t - \delta t) &= \mathbf{r}(t) - \dot{\mathbf{r}}(t)\delta t + \frac{1}{2}\ddot{\mathbf{r}}(t)\delta t^2 - \frac{1}{6}\dddot{\mathbf{r}}(t)\delta t^3 + O(\delta t^4).
\end{aligned}
\tag{2.102}
$$

using these two equations, we obtain the Verlet integrator:

$$
\mathbf{r}(t + \delta t) = 2\mathbf{r}(t) - \mathbf{r}(t - \delta t) + \ddot{\mathbf{r}}(t)\delta t^2 + O(\delta t^4).
\tag{2.103}
$$

By default, MD simulations represent microcanonical ensemble, thus number, volume, and energy (NVE) of the system are kept constant. However, for realistic simulations the temperature and pressure of the system should be also constant or in equilibrium. For this purpose, thermostat and barostat algorithms are developed. Most thermostat algorithms do this task by scaling the velocities of the atoms. In effect, they apply small kicks onto the atoms to reduce the average kinetic energy of the system therefore the temperature. For example, the Langevin thermostat uses the Langevin equation of motion instead of Newton equation:

$$
\ddot{\mathbf{r}}_i = \frac{F_i}{m_i} - \gamma\dot{\mathbf{r}}_i + \xi_i,
\tag{2.104}
$$

where $\gamma$ denotes the Langevin damping coefficient which scales the velocity and $\xi_i$ random force that maintains the temperature constant. Advantage of this algorithm is that the diffusion coefficient of the atoms can be adjusted by choosing a convenient damping coefficient. Since the diffusional properties of the molecules are especially sensitive for ODNP, this is of major importance for our work. In this thesis, the diffusion coefficient of the molecules in MD simulations are adjusted with this method.

## 2.4..2  Frequency-dependent Dielectric Response

Complex frequency-dependent dielectric response can be performed to asses the fidelity of the rotational motion of the molecules in the simulation. The analysis is based on the linear response theory[31, 32, 33] which describes the reaction of a system under applied electric field. In linear response theory, the expectation value of frequency component of polarization is proportional to the frequency component of the electric field with a

generalized susceptibility function. This function is obtained through the time correlation functions (TCF) of the electric dipole moment. These TCFs are calculated from the simulated system as follows:

$$\Phi(t) = \left\langle \mathbf{M}(\tau)\mathbf{M}(t+\tau) \right\rangle_\tau, \qquad (2.105)$$

where,

$$\mathbf{M}(t) = \sum_{a=1}^{N} \mu_a. \qquad (2.106)$$

$\mathbf{M}(t)$ represents the collective electric dipole moment of the entire simulation box with $N$ molecules at time t, and pointed brackets in (2.105) indicate averaging over the time $\tau$. Assuming rotationally isotropic motion, cross terms between Cartesian coordinates are zero, thus average over these coordinates can be also taken.

Then the frequency-dependent dielectric function can be written as [31]:

$$\epsilon(\omega) = \epsilon(\infty) - \frac{1}{Vk_{\mathrm{B}}T\epsilon_0} \int_0^\infty \mathrm{d}t \dot{\Phi}(t)\mathrm{e}^{-i\omega t}, \qquad (2.107)$$

where $V$ is volume of the simulation box, $k_{\mathrm{B}}$ is Boltzmann s constant, $T$ is temperature, $\epsilon_0$ is the permittivity of free space, and the dot above $\Phi$ indicates a derivative with respect to time. We can fit the TCFs obtained from the MD simulations to a sum of decaying exponential functions:

$$\Phi(t) = \sum_i a_i \mathrm{e}^{-t/\tau_i}. \qquad (2.108)$$

We use these functions to find the real and imaginary parts of the dielectric function through:

$$\begin{aligned}
\epsilon(\omega) &= \epsilon' + i\epsilon'' \\
&= \left[ 1 + \frac{1}{Vk_{\mathrm{B}}T\epsilon_0} \sum_i \frac{a_i}{1+(\tau_i\omega)^2} \right] + i\left[ \omega\frac{1}{Vk_{\mathrm{B}}T\epsilon_0} \sum_i \frac{a_i\tau_i}{1+(\tau_i\omega)^2} \right],
\end{aligned} \qquad (2.109)$$

where square bracketed expressions denote $\epsilon'$ and $\epsilon''$, respectively. The static dielectric constant can be evaluated through this function by equating the angular frequency $\omega$ to zero. Namely, it can be obtained by:

$$\epsilon'(0) = 1 + \frac{1}{Vk_{\mathrm{B}}T\epsilon_0} \sum_i a_i. \qquad (2.110)$$

### 2.4..3 Dipolar Spectral Density Functions

The methodology to calculate the dipolar Spectral Density Functions (SDFs) proceeds as follows. The dipolar interactions to nuclei on solvent molecules that are close in space to the free radical are calculated from the positions in the MD simulations. Dipolar interactions to more distant nuclei, all the way to infinity, are accounted analytically. For this purpose, an imaginary sphere with radius $d$ around the free radical is constructed during the analysis of the MD trajectories. Defining the inside of the sphere as near region (N) and outside as far region (F), four different time correlation functions (TCFs) are possible according to the region at some time, and time $t$ later (Fig. 2.2). The total dipolar TCF is the sum of these four contributions:

$$C_{\text{dip}}(t) = C^{\text{NN}}(t) + 2C^{\text{NF}}(t) + C^{\text{FF}}(t), \tag{2.111}$$

where for $C^{\text{FN}} = C^{\text{NF}}$ time reversibility is invoked. Only $C_{\text{NN}}(t)$ and $C_{\text{NF}}(t)$ are obtained from the MD simulations. The correlation function $C_{\text{FF}}(t)$ is calculated analytically [23] within the assumptions of the model of diffusing hard spherical molecules with centered spins (HSCS model) [34, 35].

The TCFs $C_{\text{NN}}(t)$ and $C_{\text{NF}}(t)$ are calculated from the recorded MD coordinates from:

$$C_{\text{dip}}^m(t) = \frac{1}{12} \langle F_{\text{dip}}^m(\tau) F_{\text{dip}}^m(t+\tau) \rangle_\tau, \tag{2.112}$$

where $F_{\text{dip}}^m(t) = F_{\text{dip}}^m(\mathbf{r}(t)$ are rank-2 spherical harmonics but includes the $\delta$ prefactor given in the Table 2.2. This prefactor differs for the different nuclear spin species. For $^1$H its value is $4.968 \times 10^{-4}$ nm$^3$/ ns and for $^{13}$C it is $1.249 \times 10^{-4}$ nm$^3$/ ns. The pointed brackets indicate averaging over the ensemble of molecules and over the time $\tau$. For isotropic liquids the TCFs for $m = 0, 1$ and $2$ are all equal, thus the superscript can be dropped. The SDFs corresponding to $C_{\text{NN}}(t)$ and $C_{\text{NF}}(t)$ are obtained by taking the Laplace-Fourier transform of the TCFs:

$$J_{\text{dip}}^{\text{XX}}(\omega) = \mathcal{L}[C_{\text{dip}}^{\text{XX}}(t)] = \int_0^\infty C_{\text{dip}}^{\text{XX}}(t) e^{-i\omega t} dt, \tag{2.113}$$

where XX is NN or FF. To perform the Fourier transformation, the near-near (NN) dipolar TCF is first fitted to a sum of exponential decays:

$$C^{\text{NN}}(t) = \sum_i a_i e^{-t/\tau_i}, \tag{2.114}$$

and subsequently Fourier-transformed as

$$J^{\text{NN}}(t) = \sum_i \frac{a_i \tau_i}{1 + (\omega \tau_i)}. \tag{2.115}$$
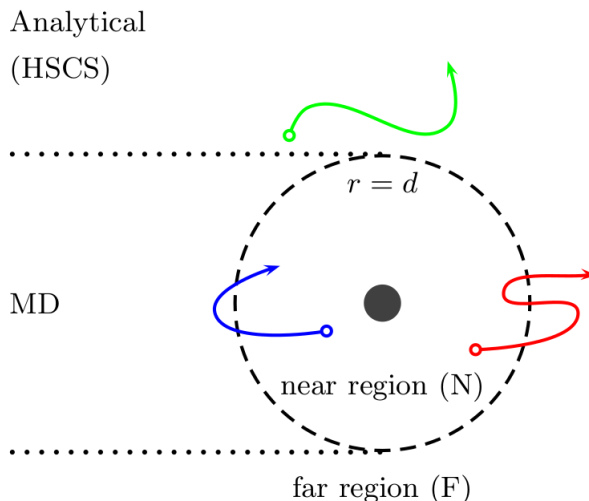
Figure 2.2: Partitioning of the space around the polarizing agent (dark circle) into near ($r < d$) and far ($r > d$) regions on the basis of the distance $r$ between the free radical and the solvent molecule. Trajectories of solvent molecules that are in N at two instances separated by time $t$ (blue path) contribute to $C_{\mathrm{NN}}(t)$. Solvent molecules starting in N and moving to F in time $t$ (red path) contribute to $C_{\mathrm{NF}}(t)$. Molecules that are in F at the beginning and end of a time interval of duration $t$ (green path) contribute to $C_{\mathrm{FF}}(t)$. This figure is taken from Ref. [1]

Due to the limited size of the MD simulation box, only molecules within a distance less than the simulation box will contribute to the MD estimate of $C_{\mathrm{NF}}(t)$. Formally, however, $C_{\mathrm{NF}}(t)$ should include the contribution of molecular trajectories reaching beyond the MD box, in principle going all the way to infinity. We, therefore, realize that $C_{\mathrm{NF}}(t)$ cannot be estimated directly from MD simulations. To overcome this problem, we introduce another auxiliary sphere centered at the free radical and having a radius $r = a$ (Fig. 2.3). When calculating TCFs from the MD trajectories we pretend that molecules crossing the surface of this outer sphere disappear. This amounts to an absorbing boundary condition at $r = a$. We refer to the region between the boundary at $r = d$ and the outer boundary at $r = a$ as the intermediate (mid) region (M).

The correlation function $C_{\mathrm{NM}}(t)$ obeying the absorbing boundary condition can be accurately determined from MD simulations that are finite in spatial extent. On the other hand, the corresponding dipolar SDF $J_{\mathrm{NM}}(\omega)$ can be obtained analytically within the classical HSCS model but subjected to an absorbing boundary condition at $r = a$ (denoted as HSCSa) [23]. The resulting analytical expression is parametrized by a diffusion constant $D$, and a distance of closest approach $b$. The desired SDFs $J_{\mathrm{NM}}(\omega)$, which correspond to an infinite region F, are obtained by letting $a \to \infty$ in the analytical expressions of the fitted $J_{\mathrm{NM}}(\omega)$. Thus, in a sense, we use the analytical expression of the HSCSa model to unfold the finite-extent $J_{\mathrm{NM}}(\omega)$ to an infinite-extent $J_{\mathrm{NF}}(\omega)$.

The same unfolding to infinite space should be applied even to the MD-estimated $J_{\mathrm{NN}}(\omega)$ since, in principle, molecular trajectories that contribute to $C_{\mathrm{NN}}(t)$ can cross into the F region and come back. (Fig. 2.2, blue path). However, because the analytical HSCSa
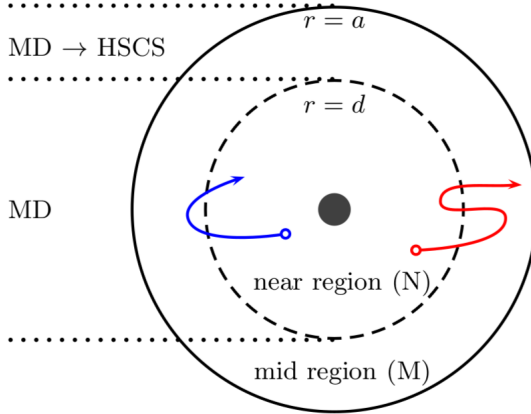
Figure 2.3: Partitioning of the space around the polarizing agent (dark circle) into near ($r < d$) and mid ($d < r < a$) regions, where the boundary $r = a$ is absorbing. This figure is taken from Ref. [1]

model assumes that the spins are at the centers of the (spherical) molecules, to perform this unfolding we calculate auxiliary $C_{\mathrm{NN}}(t)$ from the MD trajectories by pretending that the spins are at the centers of mass of the solvent and TEMPOL molecules. However, the actual spin locations on the molecules become immaterial once the spins are at a sufficiently large separation. After appropriately unfolding the MD-based $J_{\mathrm{NN}}(\omega)$ and $J_{\mathrm{NF}}(\omega)$, and calculating $J_{FF}(\omega)$ using the HSCS model, the final dipolar SDF is obtained by adding all these contributions:

$$J(\omega) = J^{\mathrm{NN}}(\omega) + 2J^{\mathrm{NF}}(\omega) + J^{\mathrm{FF}}(\omega). \tag{2.116}$$

## 2.4..4   Scalar Spectral Density Functions

Unlike the dipolar interaction, the scalar interaction is short-ranged. Therefore, for the scalar interaction, any reasonably-sized MD simulation box should automatically be sufficiently large such that applying the two-region unfolding procedure described above becomes unnecessary. Thus, it should be possible to base the estimate of the scalar TCF on the MD trajectories as such without any finite-size correction. The Fermi contact depends on the electron spin density at the positions of the nuclei of interest. While the nuclear positions can be obtained from the MD snapshots, the determination of the electron spin density requires genuinely quantum mechanical calculations. For the treatment of the scalar interaction, therefore, we introduced a quantum region in which the free radical and a few solvent molecules around it are modeled in greater (quantal) detail than available from the (classical) MD simulations (Fig. 2.4).

Differently from the near and mid regions introduced previously for the analysis of the dipolar interaction, the quantum region was not defined by a fixed distance from the center of mass of the free radical. Instead, a fixed number of solvent molecules whose
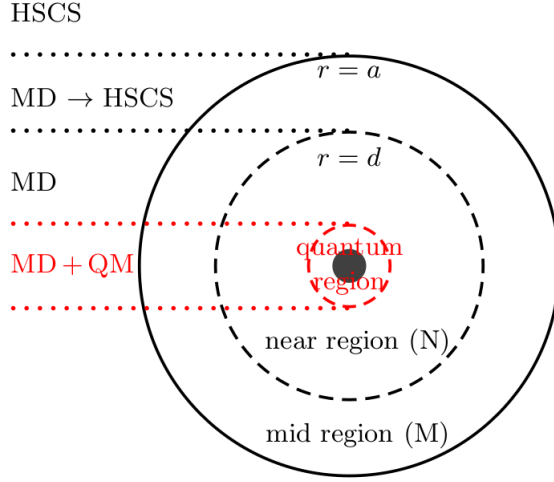
Figure 2.4: A schematic depiction of the quantum region (red) containing only a few solvent molecules closest to the oxygen atom of the nitroxide free radical. The scalar interaction is computed with *ab initio* calculations of the molecules in the quantum region as extracted from the MD snapshots. Thus, scalar SDF is obtained by combining the MD simulations with quantum mechanical calculations (MD + QM). The other two regions are necessary for the calculation of the dipolar SDF. This figure is taken from Ref. [1]

centers of mass were closest to the nitroxide oxygen atom, as well as the free radical itself, were included in the quantum region. With the so-defined quantum region, the scalar interaction between a given nucleus and the electron spin is either taken from the quantum mechanical (DFT) calculation if the nucleus is in the quantum region, or is automatically assigned as zero if the nucleus is outside the quantum region.

The time series of the Fermi contacts along the molecular trajectories, obtained either from DFT calculations or assigned as zero, are used to calculate the scalar TCFs as

$$C_{\text{iso}}(t) = \frac{2\pi}{N_I} \langle A_{\text{iso}}(\tau) A_{\text{iso}}(\tau + t) \rangle_\tau. \tag{2.117}$$

Here, $A_{\text{iso}}(t)$ denotes the Fermi contact at time $t$ in units of MHz, the pre-factor $(2\pi)$ converts the units from Hz to rad/sec, the angular brackets denote averaging over the ensemble of molecules and over the time $\tau$, and $N_I$ is the number density of the nuclear spins. The resulting TCF is fitted to a sum of decaying exponential functions, as in the dipolar case. The scalar SDFs are obtained from the scalar TCFs via one-sided Fourier transform:

$$K_\omega(t) = \int_0^\infty C_{\text{iso}} e^{-i\omega t} dt. \tag{2.118}$$

# Chapter 3

# $^1$H DNP OF ACETONE AND DMSO: DIPOLAR INTERACTION

In this chapter, computational modeling for $^1$H dynamic nuclear polarization was studied extensively by calibrating, validating and analyzing the MD simulations for the systems of acetone and DMSO solvents doped with polarizing agent TEMPOL. In the first section methodological details are given. In the next section, examination of the structures and then the validation of the partial charge distribution was carried out by analyzing the dielectric spectra for the solvents. Then the dipolar spectral density functions are calculated. Lastly, from these SDFs, relaxivities and coupling factors are reported.

## 3.1. Methods

The simulation parameters for acetone and DMSO are from the CHARMM General Force Field [36]. The atomic partial charges of the modified DMSO model, which we called DMSO*, are taken from Ref. [37] and TEMPOL parameters are taken from Ref. [38]. All MD simulations were performed with NAMD [39] accounting for electrostatic interactions with the particle-mesh Ewald method [40]. In all simulations the temperature was kept at 35 $^\circ$ C with a Langevin thermostat. Cubic boxes with periodic boundary conditions were used. An integration time step of 2 fs was employed in conjunction with SETTLE [41]. First, cubic boxes containing 2744 solvent molecules were created. For each solvent, the size of the simulation box, $L$, was selected to match the experimental densities of acetone and DMSO at 35°C (Table 3.1). By carefully choosing the friction coefficients of the Langevin thermostat that maintains the temperature of the MD simulations, we ensured that the diffusion constants of the simulated solutions match the experimental values at 35 $^\circ$ C [42, 43]. To this end, several constant volume (NVT) simulations were performed for 7 ns with different values of the friction coefficient, $\gamma$. The first 1 ns was not analyzed. Diffusion coefficients were estimated from the slope of the mean square

displacement in the time interval $400-500$ ps. Displacements in the three Cartesian directions were analyzed separately and used to calculate an average and standard deviation. The values of $\gamma$ for which the average diffusion coefficient was within one standard deviation of the experimental target was selected for the subsequent simulations.

Table 3.1: Information about the MD simulations of pure solvents or liquids containing 1 TEMPOL.

|  | $\rho$/kg m$^{-3}$ | $L$/nm | $T_{\text{pure}}$/ns | $T_{\text{low}}$/ns |
|---|---|---|---|---|
| acetone | 778 | 6.8964 | 1+6 | 1+10 |
| DMSO/DMSO* | 1085 | 6.9811 | 1+6 | 1+20 |

For simulations with TEMPOL at infinite dilution, 1 TEMPOL molecule was placed into the pure solvent boxes. Four acetone and three DMSO molecules that overlapped with the TEMPOL were removed from the boxes. Constant volume simulations were performed for 11 ns for acetone and 21 ns for DMSO. The first 1 ns was not analyzed. Atomic coordinates were saved every 0.2 ps, which is several times less than the electron Larmor frequency at 260 GHz. For the simulations with high (1 M) TEMPOL concentration, 176 TEMPOL molecules were placed into the pure acetone box and 177 TEMPOL molecules were placed into the pure DMSO box. After removing the overlapping solvent molecules, 2048 acetone and 2040 DMSO molecules remained since experimental density information about the 1 M TEMPOL solutions was not available, constant pressure (NPT) simulations were performed for 10 ns to estimate the volume. The average volume of the simulation box over this period was calculated. The box sizes were then fixed by keeping the side lengths at the values given in the third column of Table 3.2, which imply the densities reported in the fourth column of the same table. After that, constant volume (NVT) simulations were performed for a duration of $T_{\text{high}}$ ns.

Table 3.2: Information about the MD simulations with 1 M TEMPOL.

|  | # TEMPOL+solvent | $L$/nm | $\rho$/kg m$^{-3}$ | $T_{\text{high}}$/ns |
|---|---|---|---|---|
| acetone | 176+2048 | 6.6737 | 801 | 5 |
| DMSO | 177+2040 | 6.6689 | 1063 | 10 |
| DMSO* | 177+2040 | 6.7127 | 1042 | 10 |

## 3.2. Liquid structure and dynamics

The structures of acetone and DMSO are similar (Fig. 3.1), they contain the hydrogens on the polarized on methyl groups. However, while the heavy atoms of acetone constitute a plane, in DMSO heavy atoms form a pyramid due to the lone pair of electrons on the sulfur. According to the MD simulations of the pure solvents, the local structure of the two pure liquids is also similar shown in the Fig. 3.2.
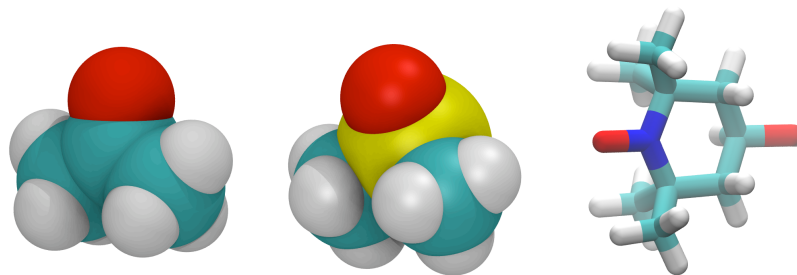
Figure 3.1: Molecular structures of acetone (left), DMSO (middle), and TEMPOL (right). This figure is taken from Ref. [2]
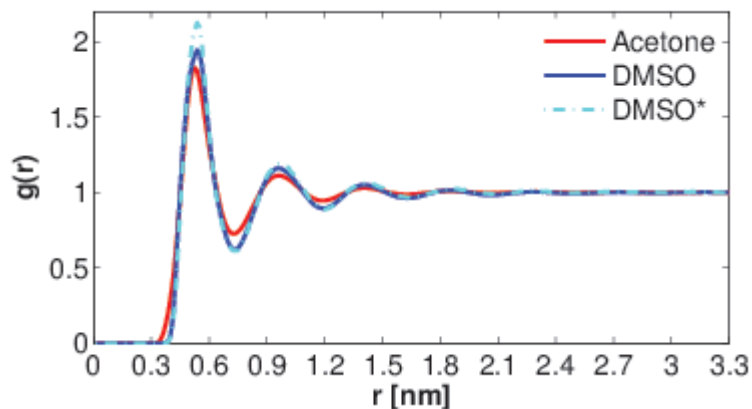


Figure 3.2: RDFs between the centers of mass of the solvent molecules from the pure-solvent simulations at 35°C. This figure is taken from Ref. [2]

The translational diffusion coefficients in the simulations are constructed to match the experimental values by adjusting the friction of the Langevin thermostat (Table 3.3). In addition to translation, the rotational diffusion of the solvent molecules is also expected to be important for high-field O-DNP, especially since it falls in the ps time window. Orientational motion in liquids can be assessed through analysis of dielectric relaxation spectroscopy [31, 33]. Therefore, to examine the degree to which the simulated molecular dynamics of the pure solvents correspond to reality, we examined the frequency-dependent electric susceptibility of acetone and DMSO. The calculated $\epsilon''$ (i.e., imaginary part of the relative permittivity) is compared with experiments in Fig. 3.3. The Debye (acetone) and Davidson-Cole (DMSO) fits to the experimental data [44, 45] are shown with black

Table 3.3: Liquid properties calculated from MD simulations at 35°C with the given choice of thermostat damping ($\gamma$): coefficients of translational diffusion ($D$) and static dielectric constants ($\epsilon$). (One standard deviation in parenthesis.)

|  | $\gamma/\text{ps}^{-1}$ | $D/\text{nm}^2\text{ns}^{-1}$ | $\epsilon$ |
|---|---|---|---|
| Acetone | 0.015 | 5.09 (0.37) | 21.4 (0.7) |
| DMSO | 0.072 | 0.94 (0.20) | 68.1 (0.5) |
| DMSO* | 0.050 | 0.92 (0.03) | 54.3 (3.6) |

dashed lines and MD calculations with colored solid lines. Although the measurements for acetone extend up to 24 GHz, the analytical fit and our prediction are drawn till 100 GHz for better visualization of the amplitude and position of the peak. The dielectric response experiments for acetone are reported at temperature 20°C [44] while our simulations are performed at 35°C. However, the fact that the static dielectric constant of acetone drops only by 3 units when going from 25°C to 53°C, the peak of $\epsilon''$ at $35°$ is expected to be about only one unit lower than what we reported in Fig. 3.3 for 20°C. The position of the peak is also expected to be slightly shifted towards higher frequencies. The experimental data for DMSO are at 35°C and extend up to 26 GHz [45].
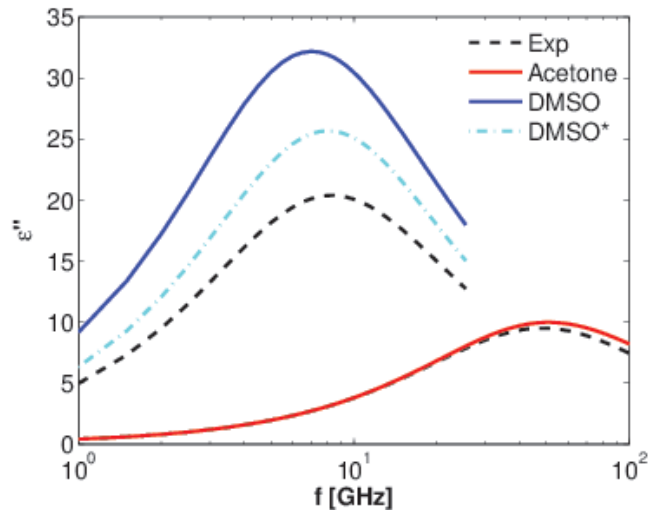


Figure 3.3: Imaginary part of the dielectric response function. Experimental data are valid up to $\sim 25$ GHz. For acetone, the analytical fit to experiment at 20°C(dashed line) and our computational prediction for 35°C (red solid line) are extended to 100 GHz to show the peak of the response. MD calculations for the original DMSO model (blue solid line) and the model DMSO* with modified charges (cyan $-\cdot-$) are shown for frequencies probed by experiment (all at 35°C). This figure is taken from Ref. [2]

The red solid line in Fig. 3.3 and the static dielectric constant calculated from simulations given in Table 3.3, we can safely conclude that the MD simulations of acetone are in good agreement with the experiments. The overestimation of the magnitude of $\epsilon$ is at most 10% and maximum of the $\epsilon''$ is very well captured. Thus, the time scales of orientation of the electric dipole moments of the acetone molecules in the simulated solution are realistic. The situation for DMSO of CHARMM DMSO parameters [46] is drastically different than the experiments. The static dielectric constant is larger by almost 50% than the experimental value (Table 3.3). Similarly, the peak of $\epsilon''$ in Fig. 3.3 (blue solid line) does not agree with experiment in magnitude, *i.e* it is larger than experiment by about 60%. Furthermore, its position on the frequency axis is shifted to the left, indicating somewhat slower reorientation of the electric dipoles of DMSO in the simulated solution compared to reality.

In order to address this discrepancy the partial charges of the heavy atoms of DMSO were changed retaining all the Force-Field parameters. The choice we consider and refer to as DMSO* is from Ref. [37]. The partial charges of the simulated solvents are given in Table 3.4. The last column of the table demonstrates that the electric dipole moment of the modified model, DMSO*, is smaller than DMSO closer to the experiment. For the pure liquid, this leads to a lower static dielectric constant (Table 3.3) and $\epsilon''$ closer to experiment (Fig. 3.3, $\cdots$ cyan line). In the case of the latter, not only the amplitude of the peak but its position on the frequency axis as well have improved. From the point of view of dielectric response, the overall deviation of DMSO* from experiment is seen to be about 20-25%, which is half of the deviation of DMSO.

Table 3.4: Partial charges (atomic units) of the specified atoms and the resulting molecular dipole moments (Debye). In the gas phase: $\mu = 2.9$ D (acetone), $\mu = 4.0$ D (DMSO).

|  | O | C/S | C | H | $\mu$ |
|---|---|---|---|---|---|
| Acetone | $-0.480$ | $0.400$ | $-0.230$ | $0.09$ | $3.6$ |
| DMSO | $-0.556$ | $0.312$ | $-0.148$ | $0.09$ | $5.2$ |
| DMSO* | $-0.437$ | $0.117$ | $-0.110$ | $0.09$ | $4.8$ |

# 3.3. Liquid properties
# in the presence of TEMPOL

We have performed two different sets of simulations for each solvent: containing one TEMPOL molecule in the simulation box, and containing 1M TEMPOL where the details of the simulations are given in the Section 3.1.. The simulations with one TEMPOL reveal that the solvent structure around the "impurity" is also very similar for the two solvents (Fig. 3.4a). The maxima and minima in solvent densities for all solvents, are found to be at identical distances from the polarizing agent, however DMSO exhibits somewhat larger amplitude of oscillations compared to acetone. Both DMSO models produced almost identical RDFs. The RDFs are seen to flatten only beyond about 2 nm from TEMPOL.

In Sec. 3.4., where dipole-dipole SDF is calculated by dividing the space around TEMPOL into near and far regions, couplings to solvent spins beyond $d = 2.5$ nm are accounted for analytically using the model of hard spheres with centered spins (HSCS) [34, 35]. Although the contribution of distant dipoles to the SDF is not very sensitive to the model parameter referred to as the "distance of closest approach," we choose the values of $b$ to be the distance at which the RDFs are equal to 0.5 (first three rows of Table 3.6).

It was reported the simulations of 1M TEMPOL in water induced a tendency to form nanoclusters, thereby causing the solvent to be substantially excluded [24]. Therefore determination of whether the polarizing agent is well accessed by acetone and DMSO is
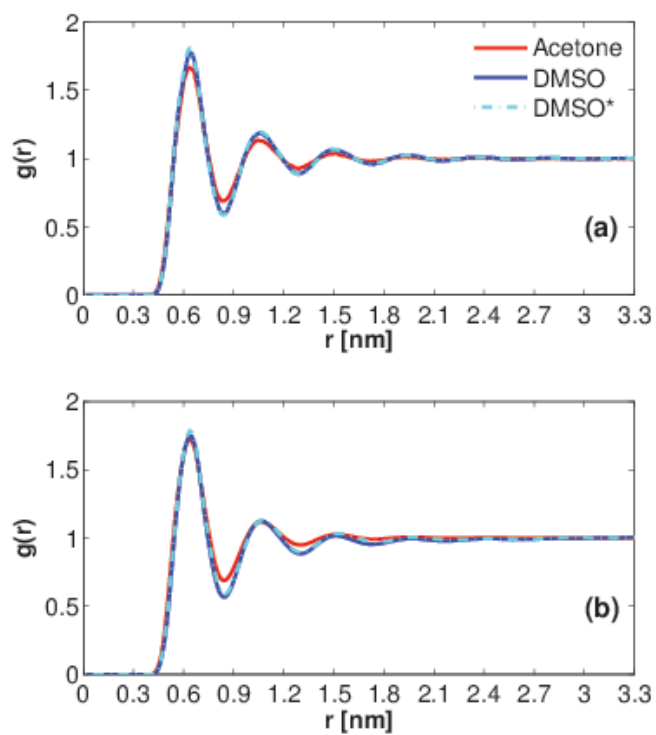
Figure 3.4: RDFs between the centers of mass of TEMPOL and the specified solvent molecules from simulations with (a) one TEMPOL molecule and (b) 1M TEMPOL. This figure is taken from Ref. [2]

Table 3.5: Diffusion coefficients (nm$^2$/ns) calculated from the simulations with one TEM-POL (1), or 1M TEMPOL (1M). (One standard deviation in parenthesis.) The viscosities of acetone, water and DMSO at 35°C are 0.283 mPa s, 0.719 mPa s and 1.655 mPa s, respectively.

| | solvent | | TEMPOL | |
|---|---|---|---|---|
| | 1 | 1M | 1 | 1M |
| Acetone | 4.93 (0.22) | 4.54 (0.37) | 3.18 (0.42) | 2.66 (0.34) |
| DMSO | 0.88 (0.01) | 0.73 (0.03) | 0.60 (0.02) | 0.41 (0.01) |
| DMSO* | 0.98 (0.01) | 1.08 (0.08) | 0.61 (0.09) | 0.67 (0.04) |

crucial in the case of high concentrations. The TEMPOL-solvent RDFs calculated from the MD simulations with 1M TEMPOL (Fig. 3.4b) are very similar to those shown in Fig. 3.4a, therefore access of the radical to solvent molecules is similar in the dilute case. Constant TEMPOL density is seen to be established in acetone and DMSO* beyond about 2 nm from any given TEMPOL molecule. Surprisingly, in DMSO (but not DMSO*) the free radicals show a slight tendency to stay closer together but do not form nanoclusters. This absence of cluster formation is especially important for the procedure summarized in Section 2.4..3 essential for the applicability of the analysis in the following sections.

The coefficients of translational diffusion of the solvent and the polarizing agent determined from the two sets of MD simulations are compiled in Table 3.5. When only one TEMPOL molecule is introduced in the simulation box the solvent diffusion (first column of Table 3.5) remains practically unchanged from its bulk value (Table 3.3). As expected, the diffusion of the single TEMPOL in acetone is faster than its diffusion in DMSO (third column of Table 3.5). In fact, the ratio of the MD diffusion coefficients is close to the ratio of the solvent viscosities. However, scaling the diffusion coefficient of TEMPOL in water (0.5 nm$^2$/ns at 35°C [24]) by the viscosities of the solvents predicts slower translational diffusion in both acetone and DMSO (1.27 nm$^2$/ns and 0.22 nm$^2$/ns) compared to the MD values in Table 3.5, indicating that the diffusion of TEMPOL in water is different in nature than its diffusion in acetone and DMSO.

The 1M TEMPOL simulations of acetone and DMSO demonstrate that both the solvent and TEMPOL molecules are slower at the elevated solute concentration (1M columns of Table 3.5). Surprisingly, the opposite trend is observed for the simulation with DMSO*. Here, both the solvent and TEMPOL molecules appear to be faster at the elevated TEMPOL concentration. This qualitative difference between the two DMSO parameter sets can be traced back to differences in the predicted density of the 1M mixture, for which experimental data are not available.

By adding the solvent and TEMPOL diffusion coefficients from Table 3.5, an estimate of the translational coefficient for relative solvent-TEMPOL motion can be obtained. These values, given in the first three rows of Table 3.6, are used in the calculation of the dipolar SDF in Sec. 3.4.. In Sec. 3.5. it is found that the relaxivities and O-DNP coupling
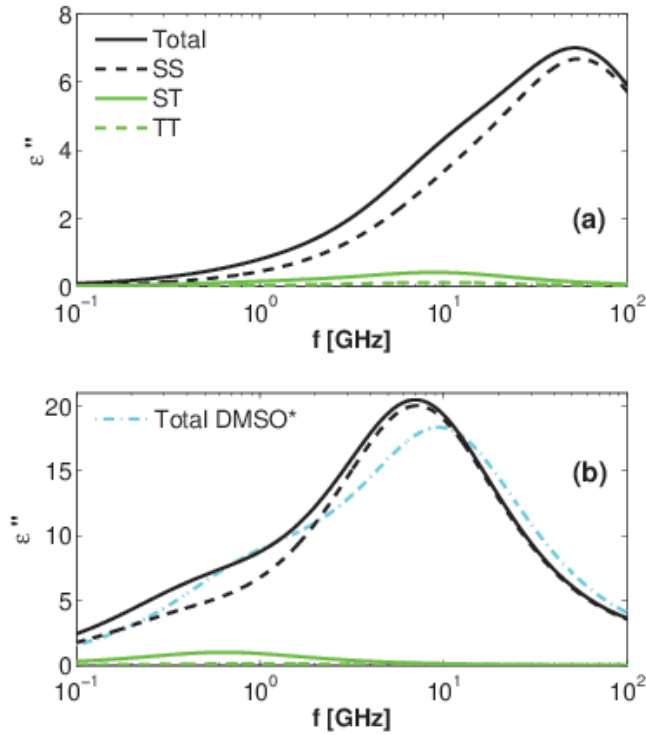
Figure 3.5: Dielectric response calculated from the simulations of 1M TEMPOL in (a) acetone and (b) DMSO. This figure is taken from Ref. [2]

factors calculated for low and high radical concentrations reflect the differences in the translational dynamics of the molecules observed in the MD simulations.

How about the rotational dynamics of the molecules? The solvent dielectric response from the simulations with one TEMPOL is essentially identical to that of pure solutions (data not shown). In the case of a mixture the absorption can be written as $\epsilon'' = \epsilon''_{SS} + \epsilon''_{ST} + \epsilon''_{TT}$, where the subscripts denote solvent-solvent (SS), solvent-TEMPOL (ST), and TEMPOL-TEMPOL (TT) contributions. The dielectric response spectra calculated from the simulations of acetone and DMSO with 1M TEMPOL are shown in Fig. 3.5. Comparing the profiles of $\epsilon''$ with those for pure solvents (Fig. 3.3) we see that in all cases the magnitude of the peak has decreased by about 30%. For acetone and DMSO, the position of the peak on the frequency axis remains practically unchanged. In other words, the time scales of rotational diffusion of the solvent molecules do not seem to be affected by the presence of 1M TEMPOL. In contrast, the peak of DMSO* in Fig. 3.5b ($-\cdot-$ cyan line) has shifted to higher frequencies compared to the pure solvent (Fig. 3.3). In Sec. 3.5. we find that this shift to faster time scales at elevated TEMPOL concentration leads to predicted DNP coupling factors which are larger than the dilute case.

## 3.4.  Dipolar spectral densities

Magnetic dipole-dipole time correlation functions (TCFs) are calculated from the MD simulations and Fourier transformed to obtain the corresponding SDFs. In the calculation, the space around a given TEMPOL radical is imagined to be composed of a near region (N) and a far region (F), as depicted schematically in Fig. 2.2. In the analysis of the MD simulations solvent molecules farther than a distance $a$ from TEMPOL are assumed to disappear as explained in the Section 2.4..3. The value of this cut-off distance is dictated by the size of the simulation box.

The $C_{NN}$ and $C_{NF}$ contributions to the TCFs calculated from the MD simulations with 1 TEMPOL are given in Figs. 3.6a and 3.6b, respectively. The solid lines are calculated by taking the nuclear spin to be at the position of a proton, and the electron spin to be divided equally between the TEMPOL nitrogen and oxygen atoms. The dashed lines, on the other hand, are calculated from the same MD trajectories but pretending that the spins are located at the centers of mass (COM) of the molecules. Clearly, the exact position of the spins is inconsequential once their separation is larger than our choice of $d = 2.5$ nm (Fig. 3.6b). In contrast, for shorter separations, the locations of the spins on the molecules influence $C_{NN}$ (Fig. 3.6a). The difference is dramatic at shorter times, which are of particular importance for O-DNP at high magnetic fields.

In the MD simulations the far region extends up to the edge of the simulation box, which typically is a few nanometers. To correct for its finite size, the far-far contribution to the SDF, $J_{FF}(\omega)$, is calculated using the HSCS model [47]. Analytical finite-size corrections to $J_{NF}(\omega)$ and $J_{NN}(\omega)$ are obtained by calculating the difference between the HSCS model and its finite-size version with absorbing outer boundary [23, 24]. All these corrections, however, assume that the approximations of hard spherical molecules with spins at their centers hold for sufficiently large inter-spin separations.

To validate these approximations, SDFs obtained by Fourier transforming the COM TCFs from Fig. 3.6 are fitted by the finite-size HSCS model. The best fits, shown in Fig. 3.7, demonstrate that the analytical model reproduces the SDFs from the MD simulations rather well. In light of Fig. 3.6b, the fit in Fig. 3.7b implies that for solvent molecules starting in the near region and reaching the far region the HSCS model is able to reproduce $J_{NF}$ with reasonable values of the model parameters $b$ and $D$ (middle of Table 3.6). However, as with toluene [23] and water [24], we find that the best-fit parameter $D$ is smaller than the sum of the coefficients of translational diffusion of the TEMPOL and solvent molecules (first three rows of Table 3.6). In the case of $J_{NN}$, the agreement in Fig. 3.7a is with the calculations where the spins are taken to be at the COM of the molecules, which is one of the approximations of the HSCS model. In this case the best fitting $D$ is even smaller (last three rows of Table 3.6), as observed previously [23, 24].

The same analysis was performed for the simulations with 1M TEMPOL. The TCFs
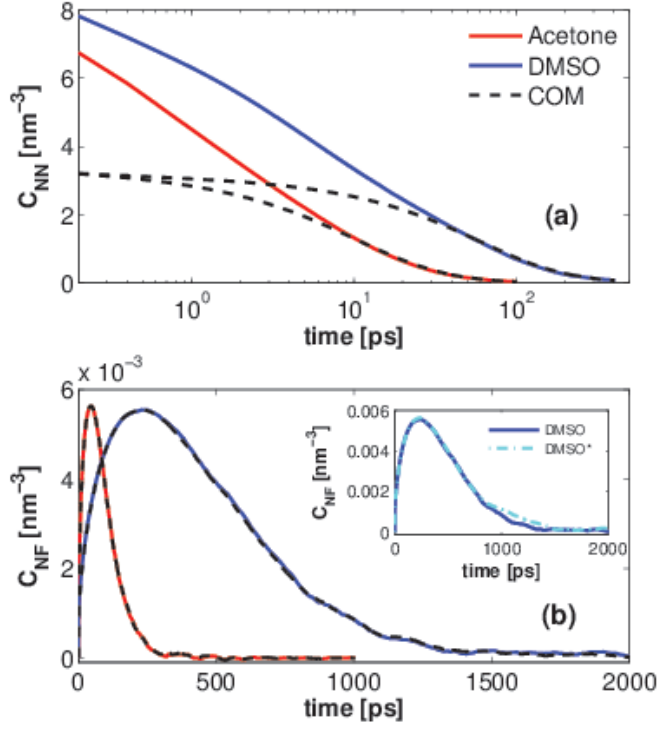
Figure 3.6: (a) Near-near and (b) near-far dipolar time correlation functions for acetone (red) and DMSO (blue). Taking the spins to be at the centers of mass (COM) of the molecules (dashed lines) makes a difference in (a) but not in (b). The inset of (b) compares DMSO and DMSO*. This figure is taken from Ref. [2]

Table 3.6: Values of $b$ (nm) and $D$ (nm$^2$/ns) determined from the fits to the MD SDFs with the finite-size HSCS model. Numbers before and after the slash are for the simulations with 1 TEMPOL and 1M TEMPOL, respectively.

|  | solvent | $b$ | $D$ |
|---|---|---|---|
| | Acetone | 0.51/0.55 | 8.11/7.20 |
| $J_{FF}$ | DMSO | 0.51/0.55 | 1.48/1.14 |
| | DMSO* | 0.51/0.51 | 1.59/1.75 |
| | Acetone | 0.40/0.45 | 6.16/5.20 |
| $J_{NF}$ | DMSO | 0.45/0.47 | 1.16/0.93 |
| | DMSO* | 0.45/0.45 | 1.15/1.25 |
| | Acetone | 0.45/0.45 | 5.22/4.10 |
| $J_{NN}$ | DMSO | 0.45/0.43 | 0.96/0.81 |
| | DMSO* | 0.45/0.43 | 0.88/1.07 |
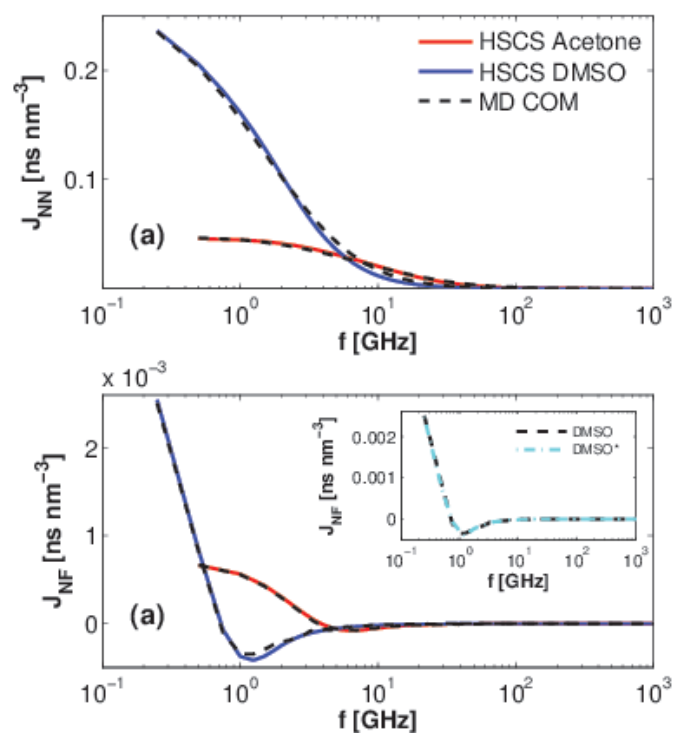
Figure 3.7: (a) Near-near and (b) near-far dipolar spectral density functions for acetone (red) and DMSO (blue). Analytical fits with the parameters given in Table 3.6 (solid lines) agree with MD results for spins assumed to be at molecular COM (dashed lines). The inset of (b) compares DMSO and DMSO*. This figure is taken from Ref. [2]

are shown in Fig. 3.8. As expected from the faster dynamics in DMSO* compared to DMSO, substantial differences are visible between the two parameter sets (inset of Fig. 3.8b). Fits to the Fourier transforms of the TCFs are given in Fig. 3.9 and their parameters are compiled in Table 3.6.
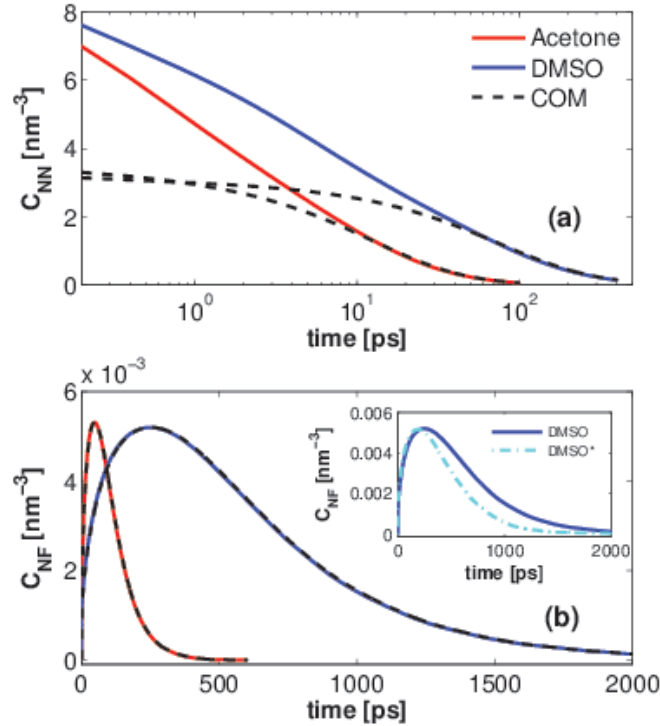


Figure 3.8: (a) Near-near and (b) near-far dipolar time correlation functions from the simulations with 1M TEMPOL. This figure is taken from Ref. [2]

The analytical fits to the SDFs calculated from the MD simulations are used to calculate finite-size corrections, as described in Section 2.4..3. Putting everything together, the dipolar SDF is calculated as in (2.116). The three additive contributions and their total are plotted as a function of frequency in Fig. 3.10 for the dilute and in Fig. 3.9 for 1 M TEMPOL solutions. Because of the relatively large size of the near region ($d = 2.5$ nm) most of the contribution to the SDF comes from the near-near (NN) correlation function. With the further choice of absorbing boundary at $a = 3.4$ nm, the near-far (NF) and far-far (FF) contributions end up being comparable in magnitude.

As evident from (2.80), in an experiment at a given magnetic field the relaxivity (2.81) and the DNP coupling factor (2.82) probe only two values of the dipolar SDF, $J(\omega_I)$ and $J(\omega_S)$. These are indicated with symbols in Fig. 3.10 and Fig. 3.11 for two different choices of the magnetic field, 0.33 T (blue) and 9.2 T (red). At the electron Larmor frequency the NN contribution completely dominates the SDF for both magnetic fields (triangles). At the proton Larmor frequency, however, the finite-size corrections to MD become important for the quantitative determination of the SDF (circles), especially at the
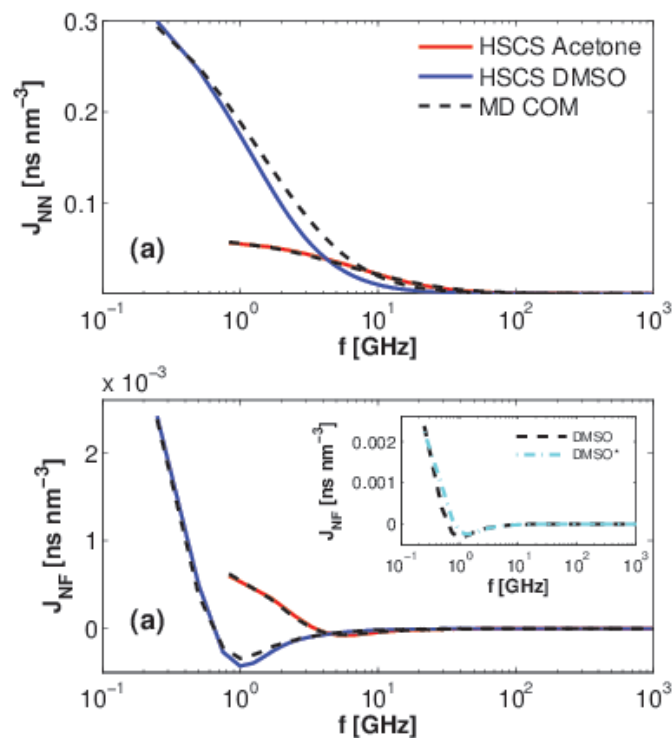
Figure 3.9: (a) Near-near and (b) near-far dipolar spectral density functions from the simulations with 1M TEMPOL. This figure is taken from Ref. [2]

lower field of 0.33 T.

## 3.5. Relaxivity and coupling factors

Armed with the dipolar SDFs we proceed to calculate the relaxivity according to (2.80) and (2.81). To this end, one copy of the SDF is multiplied by 3, while another copy is multiplied by 7 and shifted to the left along the frequency axis until the same-colored symbols in Fig. 3.10 are aligned. Finally these two contributions are added together and scaled appropriately. Figure 3.12 shows the two added parts (dashed lines) and their sum (solid line) for the dilute TEMPOL solutions of acetone and DMSO. At 0.33 T (15 MHz/9.7 GHz) $3J(\omega_I)$ and $7J(\omega_S)$ contribute equally to the relaxivity in acetone (Fig. 3.12a, blue symbols). In the case of DMSO, $7J(\omega_S)$ is about one fourth of $3J(\omega_I)$ (Fig. 3.12b, blue symbols). The relaxivity measurement at this field, therefore, encodes information about the dipolar SDF at both the nuclear and electron Larmor frequencies. In contrast, the the relaxivity at 9.2 T (400 MHz/260 GHz) is dominated by the contribution of $3J(\omega_I)$ for both acetone and DMSO (Fig. 3.12, red symbols). There is little hope, therefore, of accessing $7J(\omega_S)$ on the background of $3J(\omega_I)$ from measurements of the relaxivity at high magnetic fields. The ability to separate these two contributions is essential for predicting DNP coupling factors from NMRD relaxivity measurements.
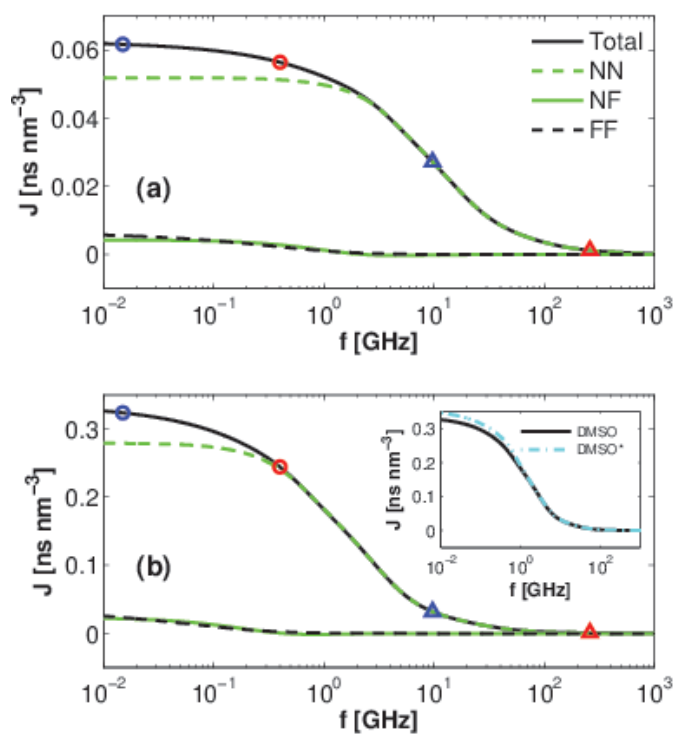
Figure 3.10: Dipolar SDF and its additive contributions from the simulations with 1 TEM-POL in acetone (a) and DMSO (b). Symbols indicate SDF values at proton (circle) and electron (triangle) Larmor frequencies at 0.33 T (blue) and 9.2 T (red). The inset of (b) compares the SDFs of DMSO and DMSO*. This figure is taken from Ref. [2]
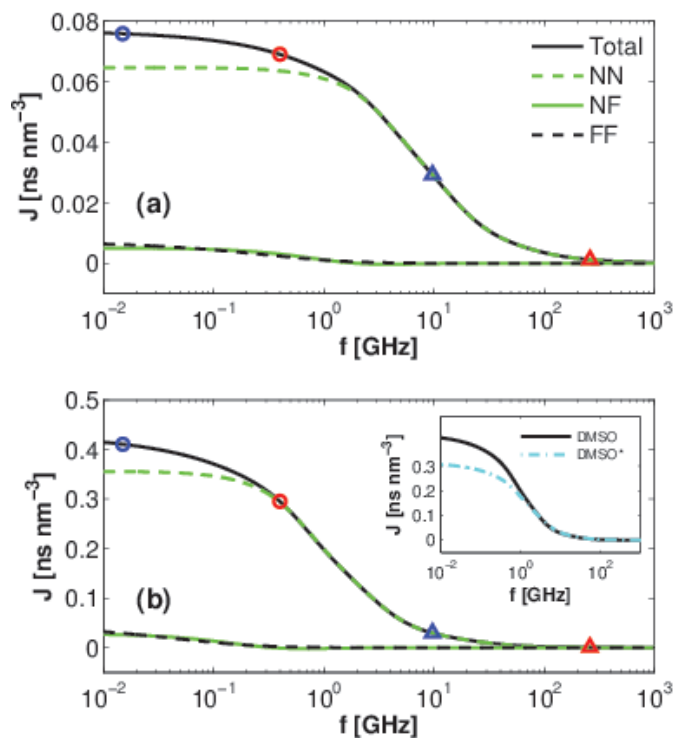
Figure 3.11: Dipolar SDF and its additive contributions from the simulations with 1 M TEMPOL in acetone (a) and DMSO (b). Symbols indicate SDF values at proton (circle) and electron (triangle) Larmor frequencies at 0.33 T (blue) and 9.2 T (red). The inset of (b) compares the SDFs of DMSO and DMSO*. This figure is taken from Ref. [2]

Our predictions of the relaxivity in Fig. 3.12 (solid lines) are compared with published [3] NMRD values (diamonds). The agreement at 260 GHz is very good. At and around 10 GHz, our predicted values for acetone are smaller than the NMRD measurements (Fig. 3.12a). The agreement is better for DMSO, where our values are somewhat larger (Fig. 3.12b). The same analysis was performed for the MD simulations with 1M TEMPOL (plots not shown).

The NMRD measurements that we compare with were performed with 40 mM TEM-POL solutions [3]. To assess the extent of variation of the relaxivity due to the experimental uncertainty in the concentration of the polarizing agent, in Fig. 3.13 we report the relaxivities deduced from nuclear $T_1$ measurements of solutions with different TEMPOL concentrations and at different temperatures. For acetone (Fig. 3.13a), the temperature variation of the relaxivity is seen to be smaller than the variation due to the TEMPOL concentration. The NMRD value at 35°C (black diamond) agrees very well with the other measurements. Similarly, the relaxivities computed from the MD simulations with 1 TEMPOL (black star at 2 mM) and 1M TEMPOL (black star at 1000 mM) are in very good agreement with the experimental data.

The situation is different for DMSO (Fig. 3.13b). Here, the variation of the relaxivity
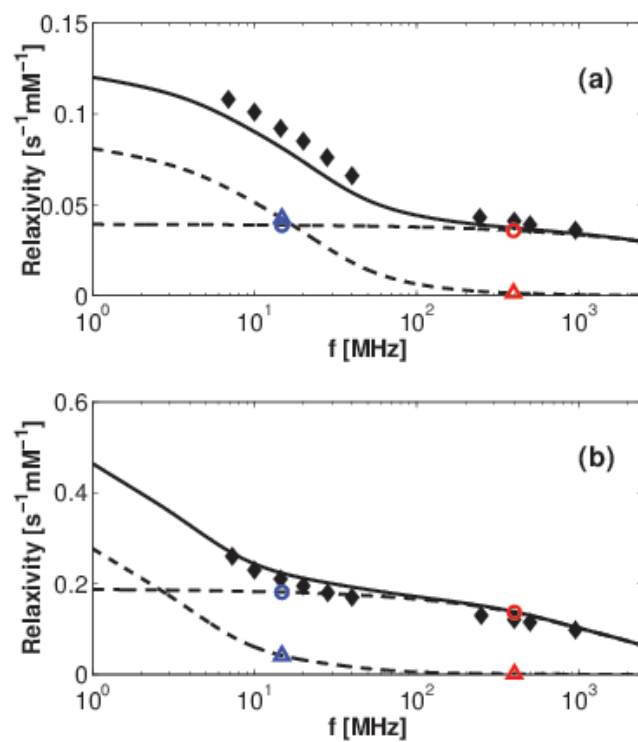
Figure 3.12: TEMPOL relaxivities in (a) acetone and (b) DMSO. The relaxivity (solid line) is the sum of two parts proportional to $3J(\omega_I)$ and $7J(\omega_S)$ (dashed lines). Colored circle and triangle symbols are same as in Fig. 3.10. Solid diamonds are NMDR values from Ref. [3]. This figure is taken from Ref. [2]
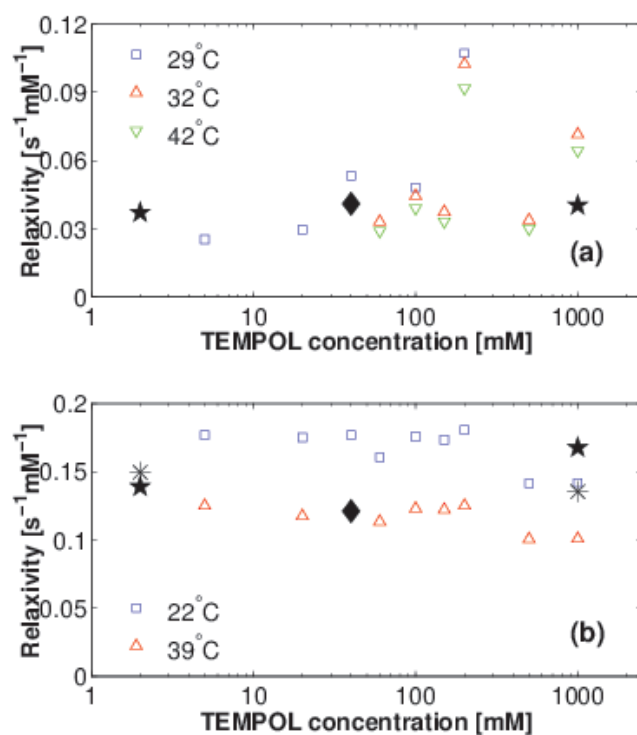
Figure 3.13: Relaxivity in (a) acetone and (b) DMSO. Comparison of estimates from $T_1$ measurements at several temperatures and TEMPOL concentrations with values from Ref. [3] and computational predictions. This figure is taken from Ref. [2]

Table 3.7: Coupling factors (%) at the specified ESR(NMR) frequencies (GHz/MHz) computed from the simulations with 1 TEMPOL (before the slash) and 1 M TEMPOL (after the slash).

|  | 9.7(15) | 34(50) | 94(140) | 260(400) | 460(700) |
|---|---|---|---|---|---|
| Acetone | 36.3/33.6 | 20.0/16.9 | 9.41/7.70 | 3.50/2.90 | 2.05/1.75 |
| DMSO | 13.4/10.3 | 4.88/3.60 | 1.53/1.15 | 0.69/0.56 | 0.44/0.38 |
| DMSO* | 13.1/13.9 | 4.79/5.28 | 1.50/1.71 | 0.65/0.74 | 0.43/0.48 |

with the concentration of TEMPOL is smaller than its change due to temperature. A small decrease of the relaxivity is measured at the largest two TEMPOL concentrations of 500 mM and 1 M. The NMRD value at 35°C (diamond) is closer to the experimental values at 39°C, whereas the relaxivities calculated from the MD simulations of DMSO (star) and DMSO* (asterisk) containing 1 TEMPOL are somewhat larger than the values at 39°C, in perfect agreement with what should be expected at 35°C. The MD calculations for 1 M TEMPOL differ between DMSO and DMSO*. The former model predicts larger relaxivity, comparable with the experimental values for lower TEMPOL concentrations at 22°C. This increase in the relaxivity with increase in the TEMPOL concentration is due to the decreasing coefficient of relative translational diffusion in the MD simulations (Table 3.6). The relaxivity calculated from the DMSO* simulations, on the other hand, agrees with what is expected from the low concentration measurements at 39°C. None of the models, however, captures the decrease of the relaxivity at TEMPOL concentrations above 0.5 M that is seen in the experiment.

Having tested the ability of the calculated SDFs to predict relaxivity, we now use them to compute DNP coupling factors for several different magnetic fields spanning the range of experimental interest (Table 3.7). As expected on the basis of the viscosities of the two solvents, the coupling factors of acetone are larger than DMSO. From a methodological point of view, it is encouraging that the coupling factors for the dilute DMSO solutions (before the slash) predicted by the two models—DMSO and DMSO*—are very similar. In line with the reduction of the diffusion coefficients (Table 3.5), smaller coupling factors are predicted for acetone and DMSO at the higher TEMPOL concentration. In contrast, again as expected from the diffusion coefficients, the simulations with DMSO* predict larger coupling factors at 1 M TEMPOL. In Fig. 3.14 the 1 M TEMPOL values at 260 GHz are compared with experiment [3]. While both DMSO and DMSO* agree well with the measurements (Fig. 3.14b), the latter is seen to perform better. In contrast, the coupling factor of acetone in our simulations is almost 50% larger than experiment (Fig. 3.14a). This is in spite of the excellent agreement of the computed relaxivity with measurements (Fig. 3.13a), demonstrating that very similar values of the relaxivity can correspond to drastically different coupling factors, in line with the observations of Ref. [3].

¡
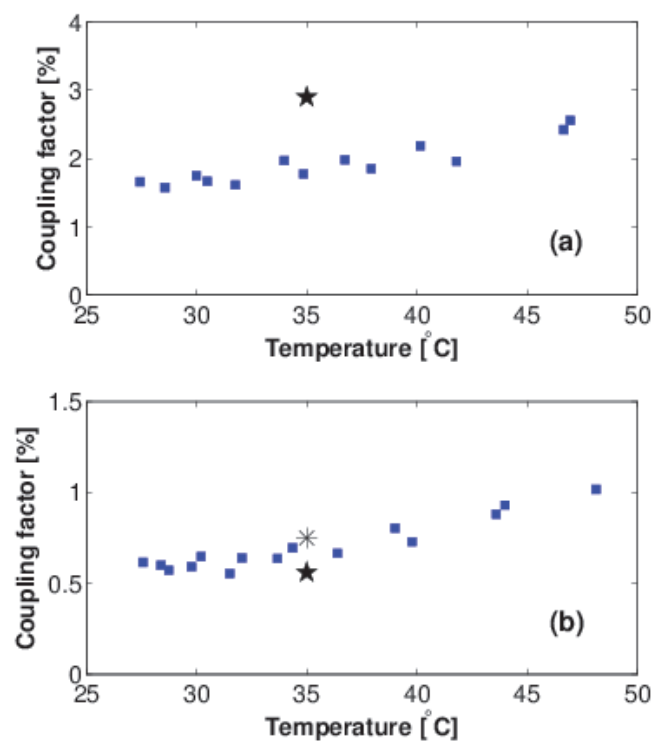
Figure 3.14: Coupling factors at 260 GHz for (a) acetone and (b) DMSO. Both experimental (blue squares) and calculated (black stars) values are with 1 M TEMPOL. DMSO* is indicated by asterisk. This figure is taken from Ref. [2]

# Chapter 4

# $^{13}$C DNP OF ACETONE FROM MD AND *AB INITIO* CALCULATIONS

In this chapter, analysis of $^{13}$C ODNP has been performed. Beside the dipolar interaction, carbons are known to be influenced by scalar coupling. Thus the scalar coupling analysis is also performed. In the first part, technical details are given. Afterwards calculation of dipolar and scalar SDFs are explained and the resulted coupling factors are discussed. Lastly, the three spin effect is examined for proton-carbon interaction.

## 4.1. Methods

The MD simulations of the 1 TEMPOL molecule in a cubic box containing 2740 acetone molecules are used in this study. *Ab initio* calculations were carried out on the molecular geometries from these MD snapshots. The packages Gaussian 09 [48] and ORCA [49] were used at the B3LYP level of theory and the EPR-II basis set. This combination is known to produce reasonably good hyperfine coupling constants [50]. In order to assess the uncertainty of the calculations, two separate fragments of the MD trajectory (located at the second and fifth nanosecond) were subjected to this analysis. Each fragment contained 1 ns of dynamics comprising 5 000 successive snapshots, making 10 000 *ab initio* calculations in total. An example of a fragment of the time series for hyperfine coupling constants are given in Fig. 4.3

The spatial distribution of the spin density due to the unpaired electron of TEMPOL is expected to be sensitive to the immediate surroundings of the free radical. For a realistic representation of the environment, the *ab initio* calculations should include as many acetone molecules near TEMPOL as possible. However, considering the steep increase of the computational cost in *ab initio* calculations with the number of atoms, a reasonable number of solvent molecules had to be chosen. To this end, for one MD snapshot, the coordinates of the TEMPOL molecule and an increasing number of acetone molecules

were provided as input to the *ab initio* calculation. The variation of the calculated Fermi contact of the methyl carbon closest to the TEMPOL oxygen is shown in Fig. 4.1 for different numbers of acetone molecules (from 1 to 7) present in the calculation (red squares). The value of $A_{\mathrm{iso}}$ is seen to increase monotonically. The increase appears to slow down once six acetone molecules closest to TEMPOL are explicitly included in the *ab initio* calculation.
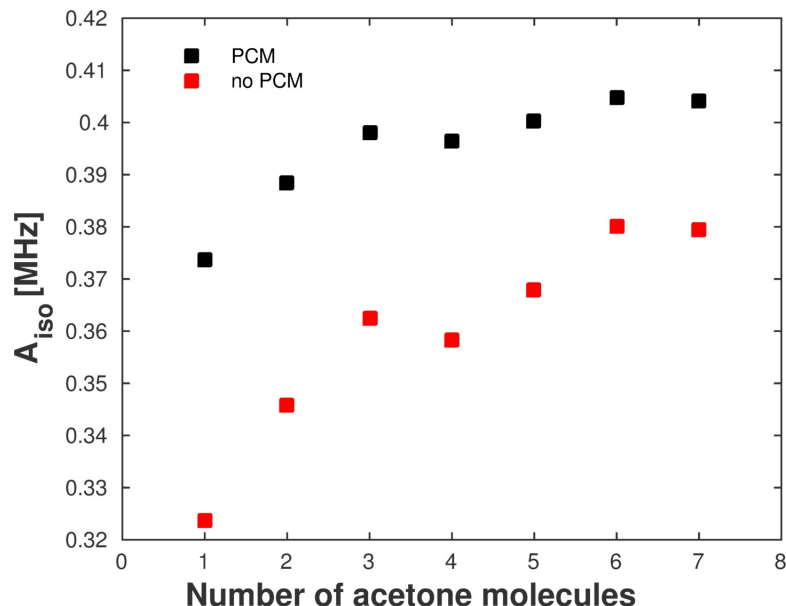


Figure 4.1: Hyperfine coupling constants of a selected methyl carbon. The closest acetone molecules to the radical TEMPOL was increased from 1 to 7 with and without polarization continuum model. This figure is taken from Ref. [4]

We further examined whether the dielectric properties of the acetone solution influence the calculated value of $A_{\mathrm{iso}}$ . The same molecular geometries were analyzed using the polarization continuum model (PCM) [51] implemented in Gaussian (Fig. 4.1, black squares). Systematically higher Fermi contact values were obtained in the calculations using the PCM. More importantly, by using the PCM the $A_{\mathrm{iso}}$ values calculated with three and more explicit acetone molecules were practically identical, showing convergence of the Fermi contact with the number of molecules in the *ab initio* calculation. In the light of these observations, TEMPOL and the six acetone molecules closest to its oxygen atom were retained in all the other MD snapshots and subjected to an *ab initio* calculation using the PCM with the dielectric constant of acetone ($\epsilon = 20.5$).

For the geometries that yielded the largest $A_{\mathrm{iso}}$ values among the 10 000 calculations we further evaluated the effect of the basis set on the calculated Fermi contacts. The numerical values produced using the packages Gaussian and ORCA with the basis sets EPR-II, EPR-III and TZVP are compared in Fig. 4.4. In spite of small numerical differences, which do not exceed 4%, all the basis sets are in good overall agreement. The electron spin densities for these snapshots are also depicted in the insets (generated with

UCSF Chimera [52]).

## 4.2.   Dipolar interaction

In the previous chapter, the report for proton ODNP was based on the assumption that the coupling between protons of acetone and TEMPOL was purely in dipolar nature and MD simulations were performed for this purpose. Using the same snapshots from these reported MD simulations, same analysis was applied for the carbon nuclear spins of the acetone solvent molecule treating only the effect of dipolar coupling. Calculated SDFS, $J_{NN}$ and $J_{NF}$, for both methyl and carbonyl carbons are given in Fig. 4.2.
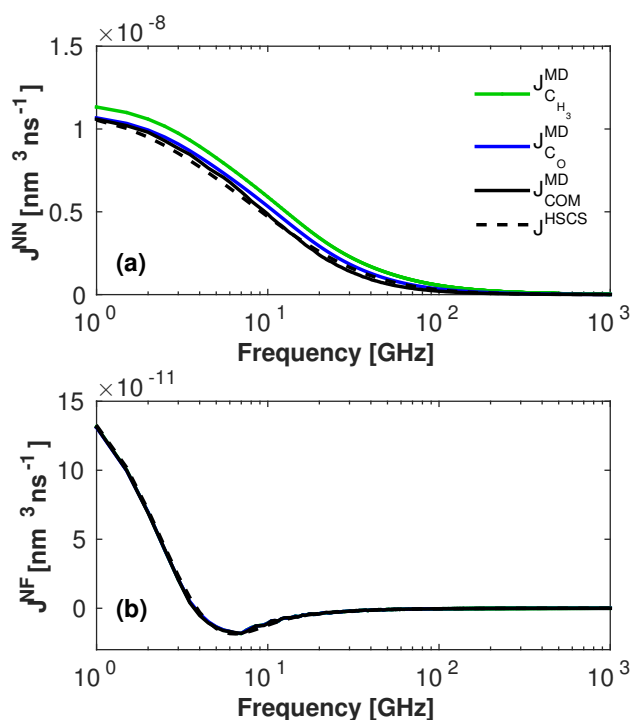


Figure 4.2:  (a) NN and (b) NM dipolar SDFs between the electron spin and the indicated carbon nuclei of acetone.  SDFs of $C_{H_3}$ (green) and $C_O$ (blue) are calculated from the actual positions of the nuclear spins.  COM SDFs (black) are calculated pretending that the electron and nuclear spins are at the centers of mass of the TEMPOL and acetone molecules. Best fits to the latter with the HSCSa model are shown with dashed lines. This figure is taken from Ref. [4]

The procedure for calculating the coupling factor is repeated for the methyl carbon ($C_{H_3}$) and carbonyl carbon ($C_O$) of acetone and obtained DNP coupling factors are given in Table 4.1.  For purpose of comparison proton coupling factors are also given in the table.

The dipolar coupling factor is known to be influenced by the translational diffusion of the spins and their distance of the closest approach, as made clear by the analytically-tractable model of hard spherical molecules with centered spins [34, 35].  Being on the

Table 4.1: DNP coupling factors (%) for $^1$H and $^{13}$C calculated at different electron Larmour frequencies (GHz) using only the dipolar interaction of electronic and nuclear spins.

|           | 9.7  | 34   | 94   | 200  | 260  | 330  | 460  |
|-----------|------|------|------|------|------|------|------|
| $C_{H_3}$ | 35.4 | 17.8 | 6.54 | 2.58 | 1.84 | 1.33 | 0.81 |
| $C_O$     | 34.4 | 15.3 | 4.37 | 1.48 | 1.00 | 0.70 | 0.41 |
| H         | 36.2 | 20.0 | 9.38 | 4.51 | 3.48 | 2.78 | 2.04 |

same molecule, we expect the translational diffusion of the carbon atoms of acetone to be the same as that for the acetone protons. However, because both the methyl and carbonyl carbon atoms are closer to the center of the acetone molecule than the protons, the coupling factors of the former are expected to be somewhat smaller. This trend is confirmed by the calculated values in Table 4.1.

## 4.3. Scalar interaction
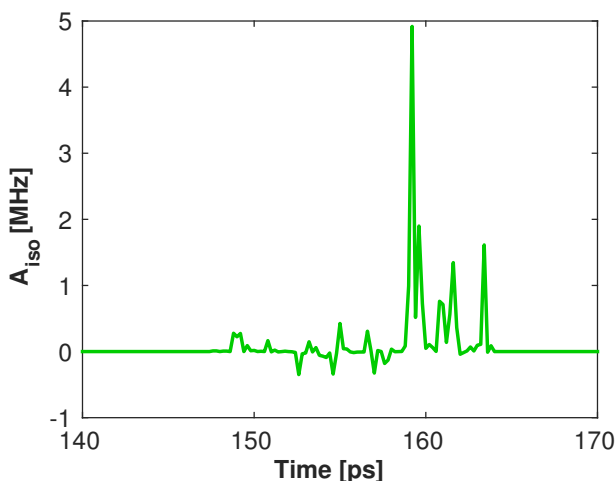


Figure 4.3: Fermi contact values of the $C_{H_3}$ nucleus as a function of time. The selected time window includes the point with observed maximum positive $A_{iso}$ value. This figure is taken from Ref. [4]

The values of the Fermi contacts from the *ab initio* calculations are shown in Fig. 4.5, where they are plotted against the distance between the TEMPOL oxygen and the respective acetone atom. Both positive and negative values occur for the three types of nuclei. While the largest positive values are larger in magnitude than the smallest negative values for the carbon atoms, positive and negative Fermi contacts of a similar absolute value are observed for the protons. Notably, the Fermi contacts do not change monotonically with the distance of the nucleus from the position of the oxygen atom of TEMPOL.

For the geometries leading to largest positive Fermi contacts (indicated by asterisk in Fig. 4.5) the positive part of the spin density is shown in the insets of Fig. 4.4. Methyl
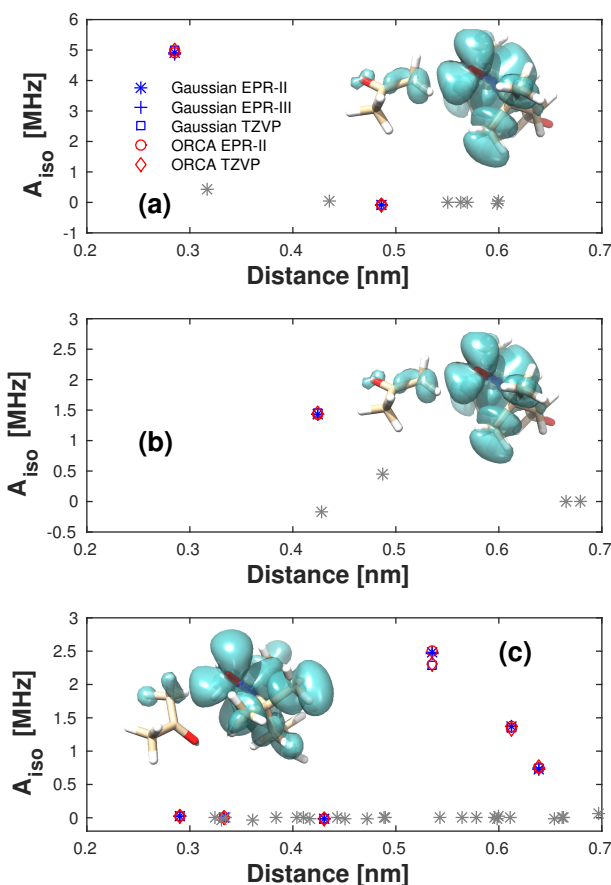
Figure 4.4: Observed maximal Fermi contacts of (a) $^{13}C_{H_3}$, (b) $^{13}C_O$, and (c) $^1H$. Different symbols show calculations with various basis sets. Colored and grey symbols represent the same kind of nuclei on, respectively, the closest (shown in inset) and more distant acetone molecules present in the same snapshot. Insets show electron spin densities for the corresponding configurations. $C_{H_3}$ and $C_O$ attain their maximum Fermi contacts in the same snapshot. This figure is taken from Ref. [4]

and carbonyl carbon atoms attain their maximum (positive) Fermi contacts in the same MD snapshot, as seen in Fig. 4.4a and b, whereas the maximum for protons is reached in a different MD snapshot (Fig. 4.4c). The molecular geometries and spin densities demonstrate how, for the acetone molecule closest to the unpaired electron of TEMPOL, the value of the spin density at the atomic nucleus does not scale with its distance from the TEMPOL oxygen. In Fig. 4.4c, for example, all the three protons of the methyl group closer to TEMPOL have positive Fermi contacts. However, the spin density at the proton farther from the TEMPOL oxygen is larger than the spin density at the closer proton, which is reflected in the magnitude of their Fermi contacts.

The scalar TCFs calculated from the $A_{iso}$ values are given in Fig. 4.6. A comparison across the three atom types reveals that $C_{iso}$ of $^{13}C_{H_3}$ (Fig. 4.6a) is an order of magnitude larger than $^{13}C_O$ (Fig. 4.6b) and $^1H$ (Fig. 4.6c). The TCF of $^{13}C_{H_3}$ also exhibits a slow decaying component of a relatively larger amplitude than the other two. In order to calculate SDFs from the TCFs the latter were fit to a multiexponential decay. The best
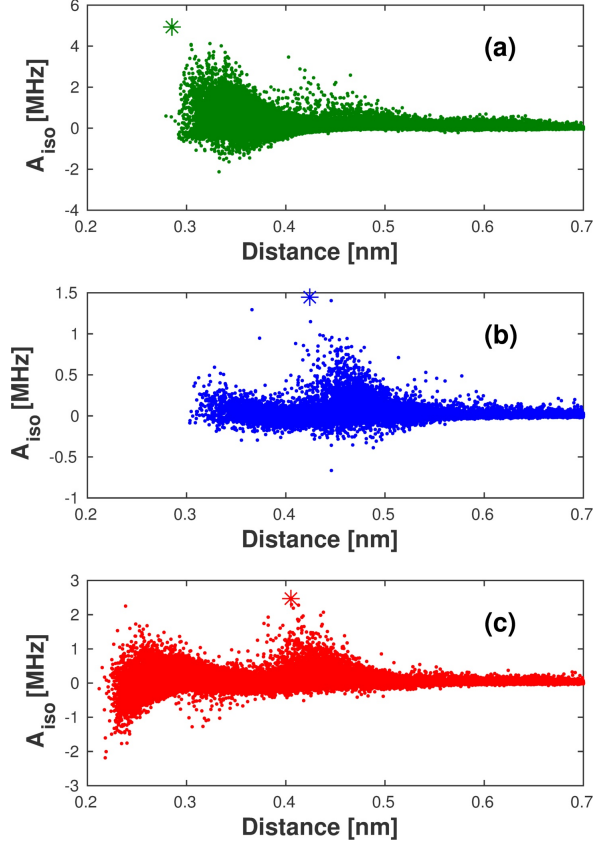
Figure 4.5: Fermi contacts of (a) $^{13}C_{H_3}$ (b) $^{13}C_O$ and (c) $^1H$ nuclei of acetone against their distances to the TEMPOL oxygen. This figure is taken from Ref. [4]

fits, shown with dashed lines in Fig. 4.6, are found to be in very good agreement with the raw data.

Fig. 4.7 shows the scalar SDFs calculated as the Fourier transform of the multiexponential fits to the TCFs. As anticipated, $K(\omega)$ for $^{13}C_{H_3}$ is larger than that of the other two nuclei. Because the SDF is affected by both the magnitude and the decay rate of the TCF, the longer tail of the $C_{iso}$ of $^{13}C_{H_3}$ leads to a larger difference in the SDFs, especially at the lower frequencies.

## 4.4. Coupling factors

The DNP coupling factor reflects the competition of the dipolar and scalar interactions between the electron and nuclear spins. At high magnetic fields $J(\omega_I) \gg J(\omega_S)$. If in addition $J(\omega_I) \gg K(\omega_S)$, then coupling factor becomes

$$c_I^S \approx [5J_{IS}(\omega_S) - 6K_{IS}(\omega_S)]/3J_{IS}(\omega_I), \qquad (4.1)$$

where the approximation follows from (2.97), (2.98) and (2.99) if $J(\omega_I) \gg J(\omega_S)$ and $J(\omega_I) \gg K(\omega_S)$. Note that while the scalar SDF contributes only at the Larmor fre-
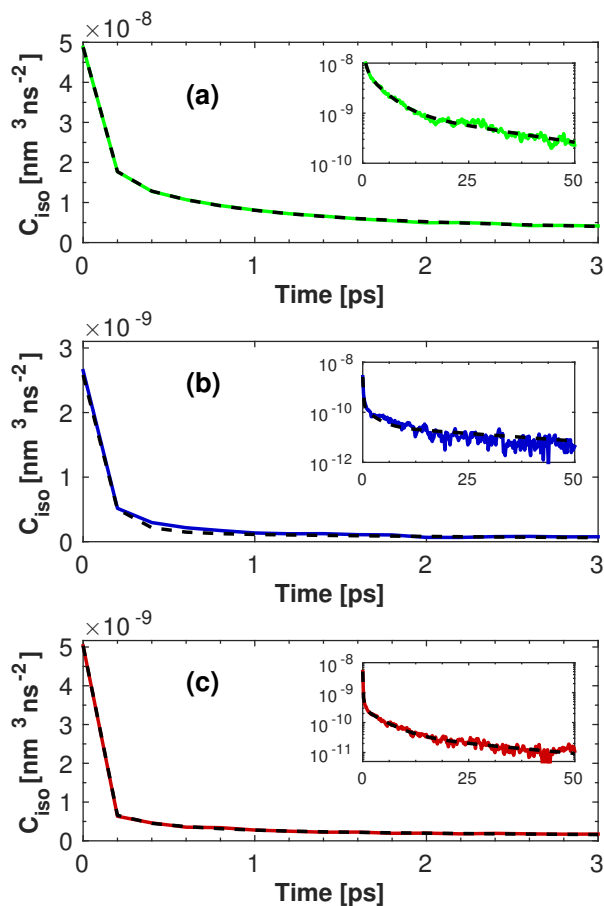
Figure 4.6: Scalar TCFs calculated from the average of two trajectory fragments (solid) and multiexponential fits (dashed) for (a) $C_{H_3}$, (b) $C_O$ and (c) H. This figure is taken from Ref. [4]
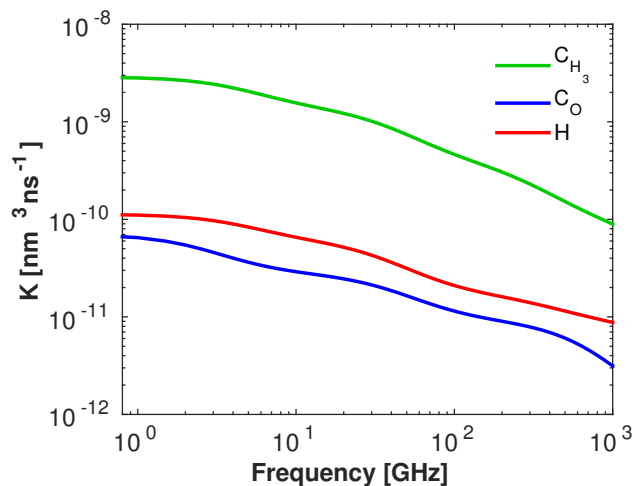


Figure 4.7: Scalar SDFs for $C_{H_3}$ (green), $C_O$ (blue) and H (red). Dashed lines are calculated from each of the two trajectory fragments. Solid lines show their average, which is our best estimate for scalar SDFs. This figure is taken from Ref. [4]

quency of the electron, the dipolar SDF is probed at both the electron and nuclear Larmor frequencies. However, being in the denominator of (2.99), a larger $J(\omega_I)$ always de-
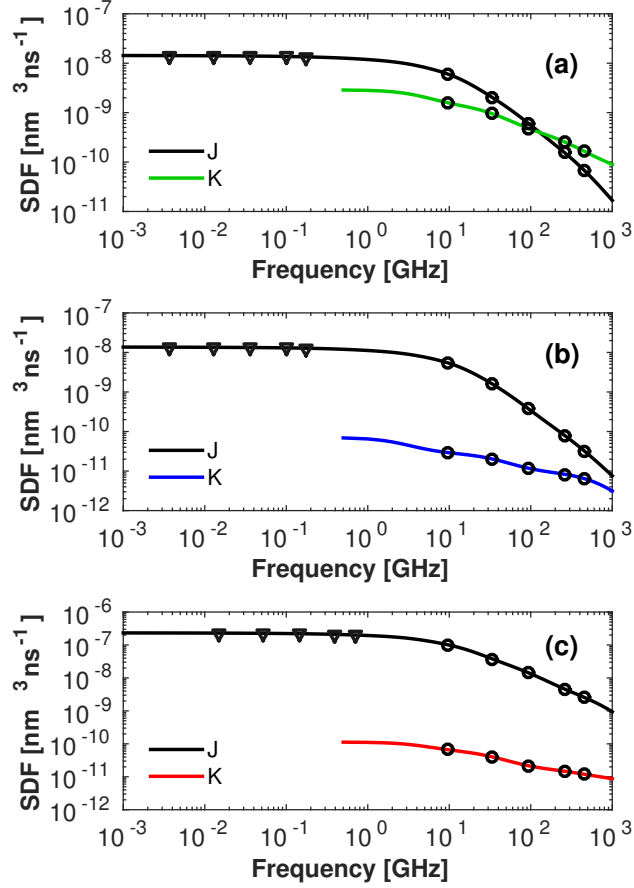
Figure 4.8: Dipolar and scalar SDFs for (a) $C_{H_3}$, (b) $C_O$ and (c) H. Symbols indicate the five electron (circle) an nuclear (triangle) Larmor frequencies reported in Table 4.2. This figure is taken from Ref. [4]

creases the magnitude of the coupling factor, independently of the competition between $J(\omega_S)$ and $K(\omega_S)$ in the numerator.

The dipolar and scalar SDFs, $J(\omega)$ and $K(\omega)$, are compared in Fig. 4.8 for the three atom types of interest. At the electronic Larmor frequencies (indicated with circles)the different nuclei exemplify different possibilities. In the case of $^1$H, $J(\omega_S)$ completely dominates over $K(\omega_S)$ over the entire frequency range (Fig. 4.8c), thus the DNP coupling factor is expected to be insensitive to the proton-electron Fermi contact. The situation is similar for $^{13}C_O$, however, the difference between the dipolar and scalar SDFs is smaller. In contrast, for $^{13}C_{H_3}$ $K(\omega_S)$ is almost equal to $J(\omega_S)$ at $\sim 94$ GHz ($\sim 140$ MHz) and exceeds it at larger frequencies. Because in (2.99) $K(\omega_S)$ is multiplied by 6 while $J(\omega_S)$ is multiplied by 5, we expect the two to balance exactly, and thus lead to vanishing DNP coupling factor, at frequencies of interest to medical MRI (50-70 GHz).

Quantitative calculation of the DNP coupling factors according to (2.99), (2.98) and (2.97) confirms these expectations (Table 4.2). Comparison with the purely dipolar coupling factors in Table 4.1 makes clear that the scalar contribution to $^1$H ODNP is negligible over the entire frequency range of experimental interest. In the case of $^{13}C_O$ scalar cou-

Table 4.2: DNP coupling factors (%) for various electron/proton Larmour frequencies (GHz/MHz) calculated by accounting for both dipolar and scalar interactions.

|  | 9.7/15 | 34/50 | 94/140 | 260/400 | 460/700 |
|---|---|---|---|---|---|
| $C_{H_3}$ | 21.7 | 7.0 | 0.2 | $-1.7$ | $-1.6$ |
| $C_O$ | 34.1 | 15.1 | 4.2 | 0.8 | 0.3 |
| H | 36.2 | 19.9 | 9.36 | 3.47 | 2.02 |

pling can be safely ignored at the lower frequencies of interest, however, its effect starts being detrimental at the higher frequencies in Table 4.2. The opposite is true for $^{13}C_{H_3}$: Scalar coupling is detrimental at the lower frequencies, entirely canceling the dipolar contribution at $\sim 94\,\text{GHz}$. It becomes sufficiently large to produce comparable (but opposite in sign) enhancement at 260 GHz. At 460 GHz the coupling factor in the presence of both scalar and dipolar coupling is two times larger in magnitude than what would be possible with dipolar coupling only.

## 4.5.  Three-spin effect

When both the $^{13}C$ and $^{1}H$ nuclei experience ODNP, the polarization of the latter has the potential to influence the polarization of the former. The extent to which the $^{13}C$ coupling coefficient will change due to this additional three-spin effect is determined by the multiplicative correction factor m defined in (2.35).

Fig. 4.9 shows the frequency dependence of the cross-relaxation $\sigma_C^H$ (black) and $\sigma_C^S$ (colored) calculated for, respectively, [H] = 80 M and [S] = 1 mM. At frequencies where the dipolar and scalar SDFs (shown in Fig. 4.8) become comparable in magnitude, $\sigma_C^S$ is vanishingly small. The values of $\sigma_C^S$ at 9.7 GHz, 94 GHz and 260 GHz are indicated with circles in Fig. 4.9. This cross-relaxation rate decreases sharply when going from 9.7 GHz to 94 GHz for both $C_{H_3}$ (Fig. 8a) and $C_O$ (Fig. 4.9b). In the case of the former, $\sigma_C^S$ is negative at 260 GHz. Thus, the correction factor m is expected to be larger than 1 at 260 GHz.

The carbon$-$proton dipolar SDF was calculated in exactly the same way as the carbonelectron SDFs. The cross-relaxation rates $\sigma_C^H$ obtained by appropriately normalizing the dipolar SDFs and multiplying by the proton density [H] = 80 M are shown in Fig. 4.9 with black lines. The magnitude of $\sigma_C^H$ is found to be very similar for the magnetic fields of 0.34 T, 3.3 T and 9.2 T (indicated by triangles in the figure).

In order to see the effect of the raidcal concentration, the multiplicative three-spin correction factors at these three magnetic fields are plotted in Fig. 4.10 for $C_{H_3}$ (left) and $C_O$ (right) by keeping the proton concentratio at [H] = 80 M and changing the TEMPOL contration varying from 1 mM to 20 mM. The plotted ratio is between $\sigma_C^H$ and $\sigma_C^S$. In addition, we used the $^{1}H$ coupling factor $\sigma_H^S$ from Table 4.2.
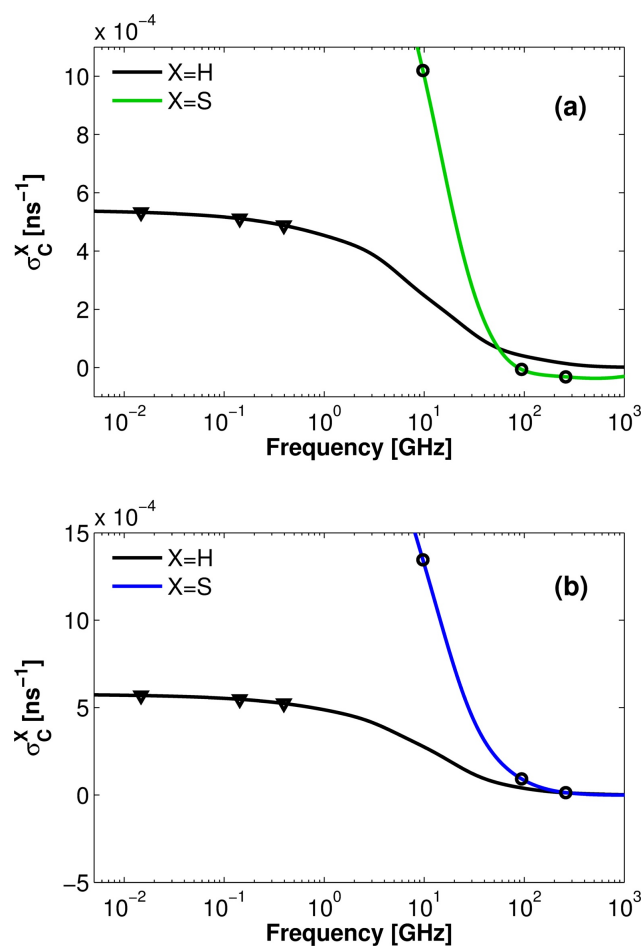
Figure 4.9: Cross-relaxation rates of (a) $C_{H_3}$ and (b) $C_O$. $\sigma_C^H$ (black) is calculated for [H] = 80 M and $\sigma_C^S$ (green/blue) is calculated for [S] = 1 mM. Symbols indicate the electron (°) and proton ($\triangle$) Larmor frequencies 9.7 GHz/15 MHz, 94 GHz/140 MHz and 260 GHz/400 MHz. This figure is taken from Ref. [4]
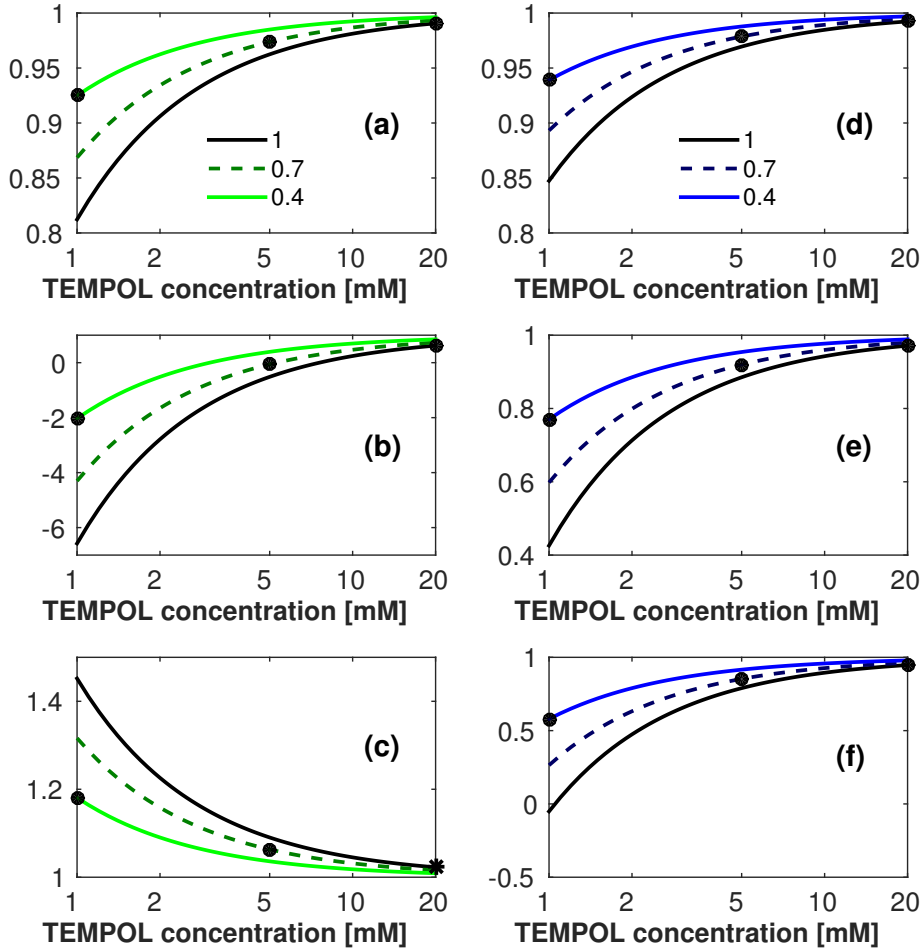
Figure 4.10: Three-spin multiplicative correction factors, m, of $C_{H_3}$ (left) and $C_O$ (right) calculated at 9.7 GHz (a and d), 94 GHz (b and e), and 260 GHz (c and f). The examined proton leakage factors are $f_H^S = 1$ (black), 0.7 (dashed) and 0.4 (colored). Plausible leakage factors for the specified TEMPOL concentrations are indicated with black points. This figure is taken from Ref. [4]

In Fig. 4.10, m is calculated for three different values of the proton leakage factor: $f_H^S = 1$ (black), $f_H^S = 0.7$ (dashed) and $f_H^S = 0.4$ (colored). Because $f_H^S$ is proportional to the concentration of the polarizing agent, we can (arbitrarily) imagine these values to correspond to TEMPOL concentrations of, respectively, 20 mM, 5 mM and 1 mM.

In all cases, at a TEMPOL concentration of 20 mM the $^{13}C$ coupling factor is essentially unaffected by the three-spin effect ($m \approx 1$). The influence is strongest at the lowest concentration of 1 mM, on which we focus now. For $C_O$ (Fig. 4.10, right), the three-spin effect is predicted to reduce the coupling factor at all magnetic fields examined in the figure. The decrease can be as small as $\sim 5$ % at 9.7 GHz (Fig. 9d) and as large as $\sim 50\%$ at 260 GHz (Fig. 4.10f). In the case of $C_{H_3}$ (Fig. 4.10, left), the three-spin effect leads to a smaller (by $\sim 5\%$) coupling factor at 9.7 GHz (Fig. 4.10a) and to a larger coupling factor (by $\sim 20\%$) at 260 GHz (Fig. 4.10c). At 94 GHz (Fig. 4.10b), the three-spin effect flips the sign of the coupling factor and increases its magnitude by a factor of $\sim 300\%$.

This huge three-spin effect is caused by the vanish- ingly small value of $\sigma_C^S$ , by which $\sigma_C^H$ is to be divided. However, because $c_C^S$ is itself proportional to $\sigma_C^S$ , the direct coupling factor of $C_{H_3}$ is already rather small at 94 GHz (Table 4.2). Thus, its significant increase caused by the three-spin effect is not expected to be very helpful in practice.

# Chapter 5

# $^{13}$C DNP OF THE ACETONE IN WATER AND CHLOROFORM

In this chapter, developed methodology for calculation of enhancements due to both dipolar and scalar interactions are subjected to cases carbons of acetone solvent mixed with water and carbons of chloroform liquids. First part gives the methodological details employed in this study and accuracy of the point-dipole approximation is examined by comparison with the DFT calculations. In the second part, report for experimental enhancements for methyl and carbonyl carbons in the mixture of water-acetone is revised. The last part reports for calculated SDFs and coupling factors are reported.

## 5.1. Methods

### 5.1..1 Simulations for acetone in water

Simulation of the box containing 1 TEMPOL, 1029 acetone and 7433 water molecules were carried out with NAMD [39]. Acetone and water (TIP3P) parameters were taken from CHARMM36 molecular Force Field [36]. Parameters of TEMPOL were from the Ref. [53].

Temperature of 25 °C and pressure of 1 atm were maintained with Langevin thermostat and barostat. The average box size was $6.98$ nm, leading to acetone concentration of $5$ M. The friction of the thermostat was chosen as $4.35$ ps$^{-1}$ in order to reproduce the reported translational diffusion constant of acetone in water ($D = 1.10$ nm$^2$/ns) [5]. Duration of the simulations was 10 ns and coordinates were recorded every $0.2$ ps.

DFT calculations were performed using the package Gaussian 09 [48]. Fermi contacts were obtained with the EPR-II basis set [50] and functionals were B3LYP and BLYP. 5000 consecutive MD snapshots, amounting to a total duration of 1 ns, were analyzed with B3LYP and 10000 consecutive snapshots were analyzed with the BLYP functional. In the BLYP case, DNP coupling factors were also obtained using only the first 5000 or

only the second 5000 snapshots in order to asses the uncertainty in the estimates due to the finite number of calculated Fermi contacts. 2 acetone and 15 water molecules closest to the TEMPOL oxygen were present explicitly in each DFT calculation. A continuum polarization model (PCM [51]) with $\epsilon = 62.5$, corresponding to a 1:3 acetone-water mixture, was employed to account for the dielectric properties of the solution.

### 5.1..2  Simulations for chloroform

MD simulations of 1 TEMPOL and 2741 chloroform molecules in a box of average size 7.17 nm were carried out with NAMD employing the barostat and thermostat to keep the temperature at 25 °C and pressure at 1 atm. The parameters of chloroform were from Ref. [54] The thermostat friction was chosen $0.014 \, \text{ps}^{-1}$ which matches the experimental diffusion coefficient of chloroform ($D = 2.8 \, \text{nm}^2 \, \text{ns}^{-1}$) [55]. The total duration of simulations was 10 ns. Snapshots were saved every $0.1$ ps. TZVP [56] was chosen as the basis set in the DFT simulations. The continuum polarization model SMD [57] with $\epsilon = 4.7$, was employed to account for the dielectric properties of the pure chloroform solution. The difference between SMD and PCM was negligible(See Fig. 5.1)
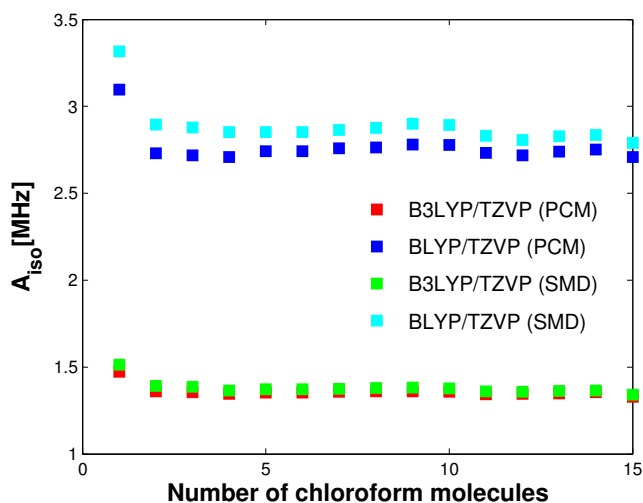


Figure 5.1: Fermi contact of carbon at the nearest chloroform calculated with increasing number of chloroform molecules around TEMPOL explicitly present in the DFT calculation. The level of theory is either B3LYP/TZVP or BLYP/TZVP, as indicated. The dielectric properties of the environment are accounted for with the continuum dielectric models PCM or SMD. This figure is taken from Ref. [1]

## 5.2.  Background

DNP measurements at 0.35 T were reported for 5 M acetone in water doped with 20 mM TEMPOL [5]. The enhancements and leakage factors of the methyl ($C_{H_3}$) and carbonyl

($C_O$) carbons of acetone are compiled in Table 5.1, with $e$ calculated from the enhancements in the absence of three-spin effects [5]. The saturation factor was estimated to be $s \approx 0.6$, with uncertainty $\approx 15\%$ [5]. Although the experimental coupling factors deduced from (2.31) depend on the value of $s$, their ratio is independent of it (Table 5.1, last row).

Table 5.1: Experimental parameters at 0.35 T [5]. The coupling factors (%) deduced from experiment, $c_{\mathrm{exp}}$, are compared with the computational predictions of the present study, $c_{\mathrm{calc}}$.

| | $e$ | $f$ | $c_{\mathrm{exp}}$ ($s = 0.6$) | $c_{\mathrm{exp}}$ ($s = 0.68$) | $c_{\mathrm{calc}}$ (BLYP) |
|---|---|---|---|---|---|
| $C_O$ | $-232$ | 0.86 | 17.2 | 15.2 | 15.3 |
| $C_{H_3}$ | $-59.3$ | 0.85 | 4.44 | 3.92 | 3.9 |
| $\frac{C_O}{C_{H_3}}$ | 3.91 | 1.01 | 3.87 | 3.87 | 3.92 |

# 5.3.  Spectral density functions and coupling factors

Overhauser DNP coupling factors can be calculated from the values of the dipolar and scalar spectral density functions (SDFs) at the Larmor frequencies of the electron ($\omega_S$) and nuclear ($\omega_I$) spins at the desired magnetic field from the equation given in (2.99). The dipolar SDF $J(\omega)$ can be calculated by seamlessly matching molecular dynamics (MD) simulations [22] and the hard sphere centered spin model [23, 24, 2]. MD simulations are employed to realistically model the short-distance molecular motions (Fig. 5.2b), and the analytical expression is used to account for the large-distance dipolar couplings (Fig. 5.2a) [23]. For the scalar SDF $K(\omega)$ in (2.99), we introduced a third, quantum mechanical region at even shorter inter-spin distances (Fig. 5.2c). Here, Fermi contacts for nuclear spin bearing molecules are calculated by subjecting the molecular geometries obtained from the MD simulations to density functional theory (DFT) calculations [4]. Since the scalar interaction is short-ranged, a few solvent molecules around the polarizing agent are sufficient to be explicitly present at this region thereby making the procedure computationally feasible.

MD simulations of an aqueous 5 M acetone solution, containing 1 TEMPOL in the simulation volume were used to calculate dipolar SDFs. Scalar SDFs were obtained from Fermi contacts calculated for 10000 consecutive MD snapshots ($= 2$ ns). The positive and negative contributions to the coupling factor in (2.99) were calculated from $J(\omega)$ and $K(\omega)$ with $\omega_S/2\pi = 9.8$ GHz and $\omega_I/2\pi = 3.74$ MHz. The results for the carbonyl and methyl carbons of acetone are shown in Fig. 5.3.
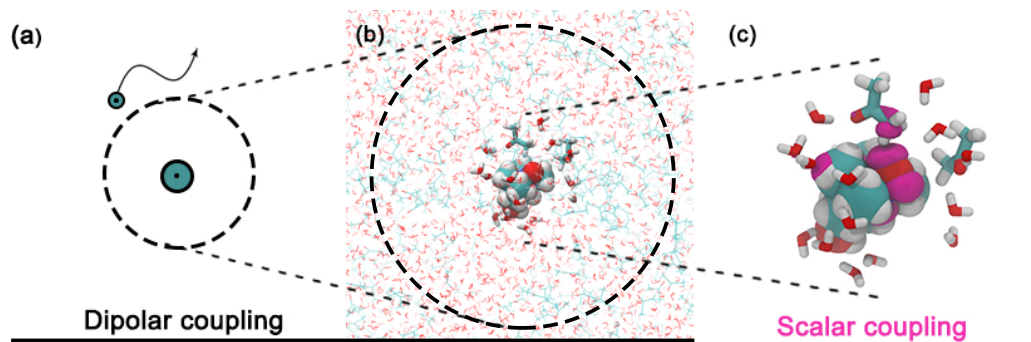
Figure 5.2: Multiscale approach used to calculate the scalar and dipolar SDFs. (b) The dynamics of the polarizing agent TEMPOL (balls) and thousands of (acetone and water) solvent molecules are followed through MD simulations. (a) The dipolar interaction between TEMPOL and solvent nuclei beyond a certain distance (dashed circle) is treated analytically. 18 (c) The scalar SDF is obtained by calculating the spin densities (magenta) for thousands of successive MD snapshots, with only a few (2 acetone and 15 water) solvent molecules closest to TEMPOL retained explicitly in the DFT calculations. This figure is taken from Ref. [1]
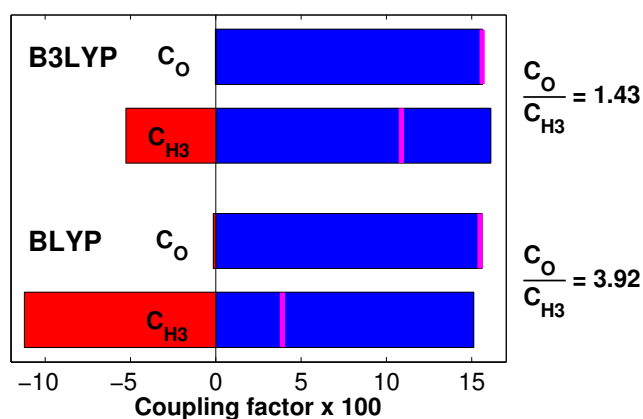


Figure 5.3: Calculated coupling factors (magenta line) of $C_O$ and $C_{H_3}$ of acetone at 0.35 T result from the competition of the positive (dipolar) contribution shown in blue and the negative (scalar) contribution in red. The latter is underestimated by the density functional B3LYP but is accurately reflected by BLYP. This figure is taken from Ref. [1]

When DFT calculations are performed with B3LYP/EPR-II [58], the ratio of the calculated coupling factors of $C_O$ and $C_{H_3}$ became 1.43 (Fig. 5.3, top), which is 2.7 times less than the experimental value (Table 5.1). The coupling factor of $C_O$ (15.6 %) is entirely due to the dipolar interaction and is in overall agreement with experiment (Table 5.1, top row). In the case of $C_{H_3}$, the scalar contribution to the coupling factor is found to be important. However, the calculated coupling factor (10.9 %) is substantially larger than the experimental value, indicating that the DFT calculations underestimate the scalar contribution.

Using the same snapshots with DFT calculations with BLYP/EPR-II, i.e., replacing the popular hybrid functional B3LYP with the pure functional BLYP, leads to much larger

scalar contribution to the coupling factor of $C_{H_3}$ (Fig. 5.3, bottom). In this case, the ratio of the coupling factors of the two carbons is 3.92, in quantitative agreement with the experiment (Table 5.1). Furthermore, with only assumption of the saturation factor $s = 0.68$ absolute values of the coupling factors (Table 5.1, last column) match exactly the experimental values. (Reported experimental error is reported as $\pm 15\%$ [5])

The dipolar and scalar SDFs $J(\omega)$ and $K(\omega)$ obtained from the analysis of 5 M acetone in water are shown in Figs. 5.4a and 5.4b for $C_O$ and $C_{H_3}$, respectively. While $J(\omega)$ is in very similar magnitudes for the carbonyl and methyl carbons of acetone, $K(\omega)$ of methyl carbon is comparable to it and carbonyl carbon SDF is negligibly small. For both carbons, BLYP leads to larger $K(\omega)$ than B3LYP across the entire frequency range. The coupling factors calculated according to (2.99) are given for five different magnetic fields in Table 5.2.

Table 5.2: DNP coupling factors (%) at several magnetic fields calculated for 5 M acetone in water at $25\,°C$. Fermi contacts were computed using the specified density functional.

| Field (Tesla) | | 0.35 | 1.2 | 3.4 | 9.2 | 16.4 |
|---|---|---|---|---|---|---|
| BLYP | $C_O$ | 15.3 | 2.91 | 0.66 | 0.13 | 0.02 |
| | $C_{H_3}$ | 3.9 | −2.7 | −2.2 | −1.1 | −0.9 |
| B3LYP | $C_O$ | 15.6 | 3.05 | 0.73 | 0.16 | 0.05 |
| | $C_{H_3}$ | 10.9 | 0.8 | −0.6 | −0.4 | −0.4 |

The same methodology was applied to TEMPOL in pure chloroform. As in the case of acetone in water, B3LYP produces substantially smaller scalar SDFs than BLYP (Fig. 5.4c). Independently of whether the scalar SDF is smaller ($C_O$), comparable ($C_{H_3}$), or larger (C of chloroform) than the dipolar SDF, its decay with frequency is slower than that of $J(\omega)$ (Fig. 5.4). To rationalize this observation we examine the magnitudes of the scalar and dipolar ($F_{\text{dip}}$) interactions between the unpaired electron and $^{13}C$ on one
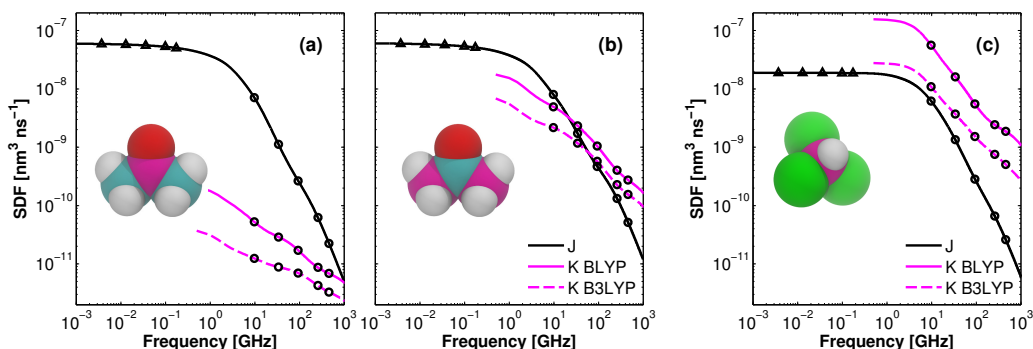


Figure 5.4: Calculated dipolar (black) and scalar (magenta) SDFs for (a) carbonyl carbon and (b) methyl carbon of acetone in water, and (c) carbon of chloroform. Symbols indicate values at the electron (circle) and $^{13}C$ (triangle) Larmor frequencies at the magnetic fields in Tables 5.2 and 5.3. (Carbon is cyan, chlorine green, hydrogen white, oxygen red, and carbon whose SDFs are shown is magenta.) This figure is taken from Ref. [1]
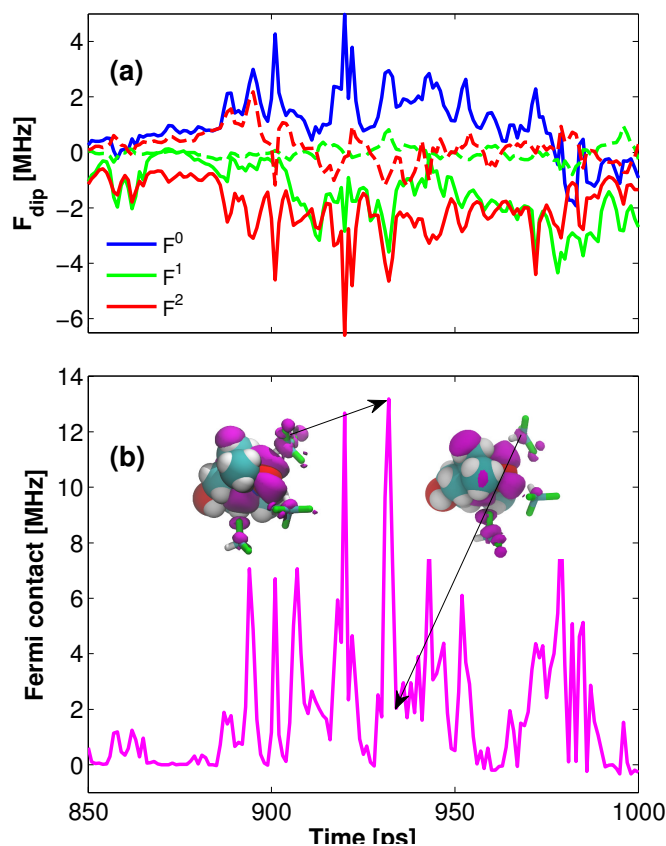
Figure 5.5: Temporal variation of the (a) dipolar and (b) scalar interactions with $^{13}$C on one chloroform molecule. In (a), the real (solid lines) and imaginary (dashed lines) parts of the solid harmonics $F_2^0$ (blue), $F_2^1$ (green), and $F_2^2$ (red) describing the dipolar interaction are obtained directly from the DFT calculations. The insets in (b) show the delocalization of the spin density (magenta) over TEMPOL and the closest three chloroform molecules. This figure is taken from Ref. [1]

chloroform molecule (Fig. 5.5). While a small change in the relative geometry of the polarizing agent and the solvent molecule has a similarly small effect on their dipolar interaction (Fig. 5.5a), it has a large effect on the Fermi contact. Evidently, the value of the Fermi contact depends on the complex distribution of the spin density (Fig. 5.5b). Because this rapid modulation affects the $K(\omega)$ at high frequencies, DNP enhancements for the high-field becomes still substantial for scalar-dominated $^{13}$C. Since dipolar SDF drops significantly at high frequencies, proton DNP produces less enhancements compared to $^{13}$C.

Our predicted $^{13}$C and $^1$H coupling factors for five different magnetic fields are given in Table 5.3. Whereas at the higher fields the proton coupling factor drops to $\approx 1\,\%$ that of carbon is $\approx -25\,\%$. For the carbon of chloroform an enhancement of $2200 \pm 330$ has been reported at 0.33 T [59]. Assuming that the leakage and saturation factors are close to one, this corresponds to c = $84 \pm 13\%$. The coupling factor at 0.35 T calculated with BLYP (78%) is in very good agreement with this experimental value, while the B3LYP value

Table 5.3: Predicted $^{13}$C and $^{1}$H DNP coupling factors (%) for TEMPOL in pure chloroform at 25 °C.

| | Field (Tesla) | 0.35 | 1.2 | 3.4 | 9.2 | 16.4 |
|---|---|---|---|---|---|---|
| C | BLYP | −78 | −64 | −43 | −26 | −22 |
| | B3LYP | −33 | −27 | −16 | −9.1 | −7.5 |
| H | BLYP/B3LYP | 34.3 | 15.1 | 5.01 | 1.64 | 0.84 |

(33%) is unrealistically low. Recently, the group of Marina Bennati has performed $^{13}$C DNP measurements on pure chloroform at 3.4 T. Their experimentally deduced coupling factor of $37\pm9\%$ (private communication) is in perfect agreement with our predicted value of $43\%$ calculated using BLYP. Again, BYLP stands out as the functional that needs to be employed to calculate Fermi contacts as part of our computational methodology.
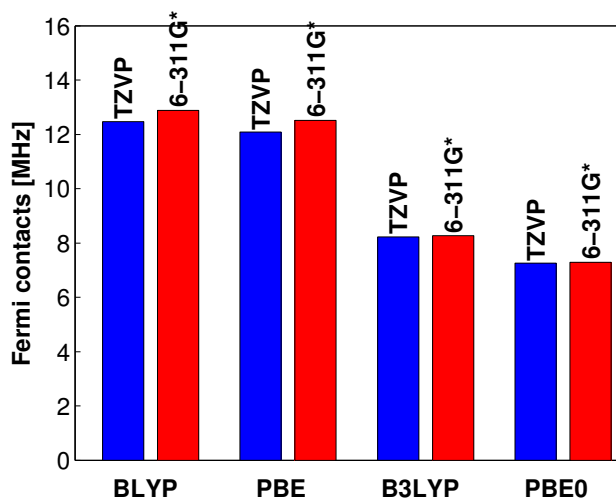


Figure 5.6: Dependence of the Fermi contact on the density functional and basis set. The configuration that gives largest Fermi contact with BLYP/TZVP was analyzed 6-311G* with other hybrid (B3LYP, PBE0) or pure (BLYP,PBE) functionals. This figure is taken from Ref. [1]

The outcomes of the functionals were further examined. The configuration that chloroform produces the largest Fermi contact with BLYP/TZVP which is shown in the inset of Fig. 5.5b, was subjected to DFT calculations with other functionals and another basis set (Fig. 5.6). The pure functionals BLYP and PBE consistently produced larger Fermi contacts than the hybrid functionals B3LYP and PBE0. In comparison, the effect of basis set is negligibly small. The majority of studies using B3LYP to calculate Fermi contacts for nitroxide free radicals focus on intra-molecular hyperfine interactions that are typically calculated on the optimized molecular geometries, unless the effect of molecular distortions is explicitly assessed [58]. In our case, inter-molecular Fermi contacts are calculated on molecular structures that are not optimal, since they come directly from the MD snapshots. Whether there is a fundamental reason for pure functionals to be more accurate than hybrid functionals in this case remains to be explored.

## 5.4.  Validation of the point-dipole approximation

In addition to Fermi contacts (i.e., isotropic scalar couplings) DFT calculations also provide anisotropic hyperfine (i.e., dipolar) couplings. This allows us to investigate the accuracy of the point dipole approximation. When calculating dipolar TCFs from the atomic coordinates in the MD trajectories, we treat the electron spin as localized at the oxygen (50%) and nitrogen (50%) atoms of TEMPOL. However, the DFT calculations clearly show the spin density is delocalized in space. Such delocalization is the reason for large Fermi contacts. As a result, the point-dipole approximation of the electron spin is expected to fail to describe the dipolar interaction with nearby nuclear spins.
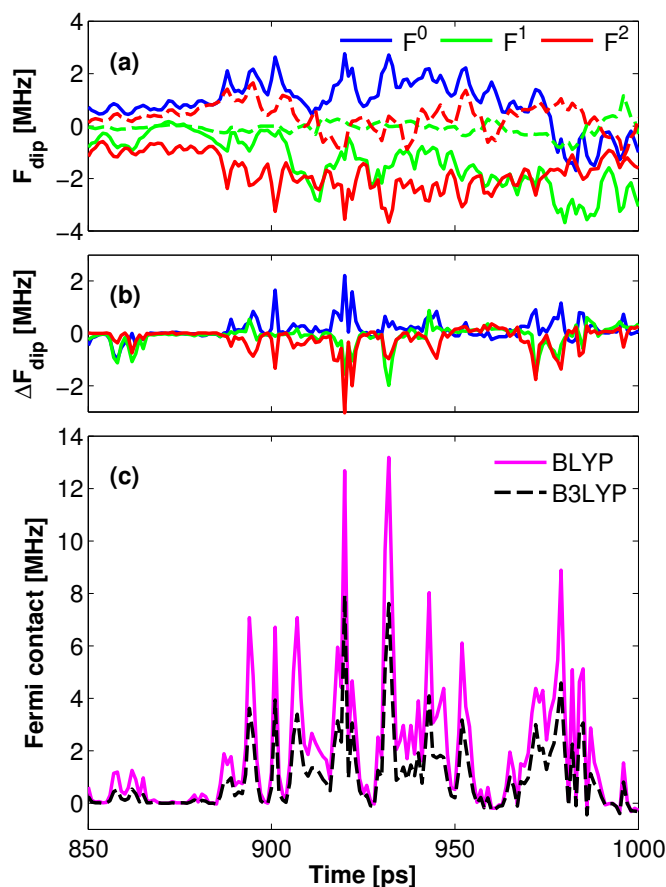


Figure 5.7: The dipolar and scalar couplings to a carbon of chloroform. In (a), the dipolar constants are calculated using the point-dipole approximation. Their difference from the coupling constant taken directly from the DFT calculations (i.e., without the point-dipole approximation) are given in (b). The Fermi contacts of the same atom are given in (c). Using the functional BLYP in the DFT calculations leads to systematically larger Fermi contacts compared to B3LYP. This figure is taken from Ref. [1]

Figure 5.7c shows the temporal variation of the Fermi contacts carbon nucleus on one chloroform molecule obtained from the DFT calculations. The solid harmonics describing the dipolar interaction between the electron spin and the nuclear spin of the same carbon atom over the same time period are given in Fig. 5.7a. These, however, were calculated

Table 5.4: DNP coupling factors (%) of chloroform calculated from 1 ns fraction of the MD simulations. Dipolar contributions for the molecules in the quantum region are calculated by either point-dipole approximation or DFT calculations. BLYP functional is used in all DFT calculations.

| Field (Tesla) | 9.8 | 34 | 94 | 260 | 460 |
|---|---|---|---|---|---|
| point dipole | −78.2 | −64.8 | −43.4 | −26.9 | −22.6 |
| DFT + p.d. | −77.8 | −64.4 | −43.1 | −26.6 | −22.4 |
| $\Delta$ | 0.3 | 0.3 | 0.2 | 0.2 | 0.14 |

from the distance vector between the atomic positions namely relying on the point-dipole approximation. The same solid harmonics is also obtained with DFT calculations and their differences are plotted in 5.7b. As expected, the point-dipole approximation fails at the instances exhibiting substantial Fermi contacts. On the other hand, the performance of the approximation is seen to be acceptable for the instances of small Fermi contacts. This implies that it can be safely used for molecules outside the quantum region, where the scalar couplings are vanishingly small anyway.

Although we have demonstrated the limitations of the point-dipole approximation, what matters from a practical point of view is the impact of the approximate treatment on the calculated DNP coupling factors. The calculated coupling factors are given in Table 5.4 The differences between the coupling factors are seen to be small and less than the statistical uncertainties of the 10 ns simulations [1].

# Chapter 6

# CONCLUSION AND OUTLOOK

In this thesis, a multiscale computational modeling that quantitatively predicts the magnitude of Overhauser DNP enhancements in simple liquids is presented. First, the methodology was applied for proton DNP of liquids, acetone and DMSO. Only dipolar interaction was taken into account and for protons dipolar coupling is almost always true. Translational and rotational motion of the simulated molecules were validated due to the high sensitivity of the ODNP on the molecular motions. These tasks were achieved by calibrating the Langevin damping coefficient of the simulations for translational diffusion and dielectric response analysis for the rotational diffusion. This validation procedure pushed us to seek for different Force Field models for DMSO, therefore two different Force Field were used for DMSO.

The dipolar spectral densities were calculated for diluted and concentrated solutions of acetone, DMSO and modified DMSO simulations. From the spectral density functions, we were able to calculate various experimental parameters such as coupling factors and relaxivities which were reported for a broad range of magnetic fields. They were directly compared with the experimental results. Our calculations of relaxivities were in perfect agreement with the experiments performed at high magnetic fields (9.2 T). Coupling factors calculated from DMSO and modified DMSO models also gave similar values and good agreement with experiment at 9.2 T was achieved. For acetone, on the other hand, our prediction at 9.2 T was larger than the experiment by almost %50 despite the good agreement of the relaxivities. This discrepancy can be originated from the flawed Force Field models which may not reflect the reality although the orientational motion of the model was better agreement with the experiments.

Secondly, the scope of the methodology was extended by introducing the scalar coupling contribution. Addition of the scalar coupling makes possible to calculate the ODNP enhancements of nuclear spin species where larger enhancements than proton is possible. The methodology was applied to the $^{13}C$ DNP for carbonyl and methyl carbons of acetone. The calculated coupling factors due to only dipolar interaction produced were similar to coupling factors of the proton DNP. This was expected since the magnitude of

the dipolar coupling, in principle, varies with the diffusion coefficient of molecules and the distance of closest approach between the nuclear and electron spins. Since the latter depends on the shape of the molecule, proximity of the spins are dictated by the position of the nuclear spin in the molecule. Since the distance from the center of mass of acetone is similar for carbons and protons, dipolar contribution was expected to be similar.

The scalar interaction contribution was quantified by computation of Fermi contacts from coordinates taken from a fragment of the MD simulations. The Fermi contact values were changed from negative to positive values very quickly throughout the motion of the molecules. Therefore a fast decay of the TCFs were observed for all nuclei types. While the magnitude of this TCFs were substantially small and close to each other for proton and carbonyl carbon, magnitude of the methyl carbon demonstrated a much larger intensity. Therefore, the scalar contribution from proton and carbonyl carbon was observed to be negligible, agreeing with the common knowledge of the dominance of the dipolar interaction in the proton DNP. The magnitude of the scalar and dipolar SDFs for methyl carbon was similar therefore produced smaller enhancement factor since they run against each other.

The calculated coupling factors were compared with the experimental values. Although there was a qualitative agreement, the numbers were substantially different. The reason for this was speculated as the simulated system was not exactly matching with the experimental conditions. For instance, experimental system was a mixture and simulations contain pure acetone. And the temperature of the experiment was 25°C while simulations were executed under 35°.

Three spin effect which corresponds to the effect of the enhancement due to secondary nucleus on the polarization of a nucleus was also analyzed. This analysis was performed on the acetone liquid which simultaneously has the carbon and proton nuclei. Calculated results, suggested a negligible effect.

In the third part, the density functional method which we used in our Fermi contact calculations was examined. In the previous study, applied functional/basis set combination was B3LYP/EPR-II which is a highly popular functional and basis set for calculation of the Fermi contact couplings. In the analysis, we have performed several functional dependency tests. For a configuration, the computations were performed with hybrid functionals such as B3LYP and PBE0 and also with pure functionals such s BLYP and PBE. The pure functionals produced much larger contact values than the hybrid functionals. The calculated enhancements for $^{13}C$ of acetone in the acetone-water mixture and carbon of chloroform are compared with experiments. The results suggested that the DNP calculations with popular hybrid functionals are unable to match the experimental values while the pure functionals produced enhancements that perfectly agrees with experiments. Therefore, our calculations suggest that the pure functionals produce better results for inter-molecular hyperfine coupling constants calculations despite the fact that

intra-molecular coupling constants are better computed by hybrid functionals.

In conclusion, the presented methodology quantitatively predicts the magnitude of Overhauser DNP enhancements with a multiple scale offering applicability to systems under any magnetic field. Therefore the methodology provides a broad spectrum of predictions that can be utilized for the knowledge-based experiments.

However, current version of the methodology assumes that the media of the simulations are isotropic which limits the applicability to only simple liquids and fairly small radicals. Since most of the biological systems contain biomolecules such as proteins, lipids and micelles which give rise to anisotropic motions. Therefore one extension of the methodology may be the incorporation of anisotropic motions into the model.

Since, the methodology depends on the MD simulations, the predictions is affected from the choice of Force Fields. For this reason, validation of the Force Fields especially for the respect of translational and rotational motion is crucial. The translational motion can be taken care by adjusting the friction coefficient of the thermostat in MD simulations, but the rotational motion depends on the given parameters for the partial charge distribution. However, Force Fields assume partial charges to be static, whereas Polarizable Force Fields are developed for a time dependent charge distribution which can reflect better representation of the rotational motion.

The experimental procedure of DNP involves the MW irradiation of the sample which results with undesired heating of the sample. Therefore, this leads to alteration of the relaxation time $T_1$ and thus coupling factor. The contribution of the MW irradiation is discussed in the Ref. [60]. The influence of the irradiation can be theoretically estimated and incorporate to the methodology.

# Bibliography

[1] Sami Emre Kucuk and Deniz Sezer. Multiscale computational modeling of 13c dnp in liquids. *Phys. Chem. Chem. Phys.*, 18:9353–9357, 2016.

[2] Sami Emre Küçük, Petr Neugebauer, Thomas F. Prisner, and Deniz Sezer. Molecular simulations for dynamic nuclear polarization in liquids: a case study of tempol in acetone and dmso. *Phys. Chem. Chem. Phys.*, 17:6618–6628, 2015.

[3] Petr Neugebauer, Jan G. Krummenacker, Vasyl P. Denysenkov, Christina Helmling, Claudio Luchinat, Giacomo Parigi, and Thomas F. Prisner. High-field liquid state NMR hyperpolarization: a combined DNP/NMRD approach. *Phys. Chem. Chem. Phys.*, 16:18781–18787, 2014.

[4] Sami Emre Küçük, Timur Biktagirov, and Deniz Sezer. Carbon and proton overhauser dnp from md simulations and ab initio calculations: Tempol in acetone. *Phys. Chem. Chem. Phys.*, 17:24874–24884, 2015.

[5] Mark D. Lingwood and Songi Han. Dynamic nuclear polarization of 13C in aqueous solutions under ambient conditions. *J. Magn. Reson.*, 201(2):137 – 145, 2009.

[6] Albert W. Overhauser. Polarization of nuclei in metals. *Phys. Rev.*, 92(2):411–415, 1953.

[7] T. R. Carver and C. P. Slichter. Polarization of Nuclear Spins in Metals. *Physical Review*, 92:212–213, October 1953.

[8] K. H. Hausser and D. Stehlik. Dynamic nuclear polarization in liquids. *Adv. Magn. Reson.*, 3:79–139, 1968.

[9] Werner Müller-Warmuth and Karin Meise-Gresch. Molecular motions and interactions studied by dynamic nuclear polarization (dnp) in free readical solutions. *Adv. Magn. Reson.*, 11:1–45, 1983.

[10] Maria-Teresa Türke, Igor Tkach, Marcel Reese, Peter Höfer, and Marina Bennati. Optimization of dynamic nuclear polarization experiments in aqueous solution at 15 MHz/9.7 GHz: a comparative study with DNP at 140 MHz/94 GHz. *Phys. Chem. Chem. Phys.*, 12(22):5893–5901, 2010.

[11] P. J. M. van Bentum, G. H. A. van der Heijden, J. A. Villanueva-Garibay, and A. P. M. Kentgens. Quantitative analysis of high field liquid state dynamic nuclear polarization. *Phys. Chem. Chem. Phys.*, 13(39):17831–17840, 2011.

[12] Eugeny V. Kryukov, Kevin J. Pike, Thomas K. Y. Tam, Mark E. Newton, Mark E. Smith, and Ray Dupree. Determination of the temperature dependence of the dynamic nuclear polarisation enhancement of water protons at 3.4 Tesla. *Phys. Chem. Chem. Phys.*, 13(10):4372–4380, 2011.

[13] Petr Neugebauer, Jan G. Krummenacker, Vasyl P. Denysenkov, Giacomo Parigi, Claudio Luchinat, and Thomas F. Prisner. Liquid state DNP of water at 9.2 T: an experimental access to saturation. *Phys. Chem. Chem. Phys.*, 15(16):6049–6056, 2013.

[14] G. H. A. van der Heijden, A. P. M. Kentgens, and P. J. M. van Bentum. Liquid state dynamic nuclear polarization of ethanol at 3.4 T (95 GHz). *Phys. Chem. Chem. Phys.*, 16:8493–8502, 2014.

[15] Eugeny V. Kryukov, Mark E. Newton, Kevin J. Pike, David R. Bolton, Radoslaw M. Kowalczyk, Andrew P. Howes, Mark E. Smith, and Ray Dupree. DNP enhanced NMR using a high-power 94 GHz microwave source: a study of the TEMPOL radical in toluene. *Phys. Chem. Chem. Phys.*, 12(22):5757–5765, 2010.

[16] Nikolay Enkin, Guoquan Liu, Igor Tkach, and Marina Bennati. High dnp efficiency of tempone radicals in liquid toluene at low concentrations. *Phys. Chem. Chem. Phys.*, 16:8795–8800, 2014.

[17] Marcel Reese, Maria-Teresa Türke, Igor Tkach, Giacomo Parigi, Claudio Luchinat, Thorsten Marquardsen, Andreas Tavernier, Peter Höfer, Frank Engelke, Christian Griesinger, and Marina Bennati. 1H and 13C dynamic nuclear polarization in aqueous solution with a two-field (0.35 T/14 T) shuttle DNP spectrometer. *J. Am. Chem. Soc.*, 131(42):15086–15087, 2009.

[18] S. Stevenson, T. Glass, and H. C. Dorn. 13C dynamic nuclear polarization: an alternative detector for recycled-flow nmr experiments. *Analytical Chemistry*, 70(13):2623–2628, 1998.

[19] Maria-Teresa Türke, Giacomo Parigi, Claudio Luchinat, and Marina Bennati. Overhauser DNP with 15N labelled Fremy's salt at 0.35 Tesla. *Phys. Chem. Chem. Phys.*, 14(2):502–510, 2012.

[20] Oliver Neudert, Carlos Mattea, Hans Wolfgang Spiess, Siegfried Stapf, and Kerstin Münnemann. A comparative study of 1H and 19F Overhauser DNP in fluorinated benzenes. *Phys. Chem. Chem. Phys.*, 15:20717–20726, 2013.

[21] Oliver Neudert, Carlos Mattea, Siegfried Stapf, Miriam Reh, Hans W. Spiess, and Kerstin Münnemann. Fast-field-cycling relaxometry enhanced by dynamic nuclear polarization. *Microporous and Mesoporous Materials*, 205(0):70 – 74, 2015.

[22] Deniz Sezer, M. J. Prandolini, and Thomas F. Prisner. Dynamic nuclear polarization coupling factors calculated from molecular dynamics simulations of a nitroxide radical in water. *Phys. Chem. Chem. Phys.*, 11(31):6626–6637, 2009.

[23] Deniz Sezer. Computation of DNP coupling factors of a nitroxide radical in toluene: seamless combination of MD simulations and analytical calculations. *Phys. Chem. Chem. Phys.*, 15(2):526–540, 2013.

[24] Deniz Sezer. Rationalizing Overhauser DNP of nitroxide radicals in water through MD simulations. *Phys. Chem. Chem. Phys.*, 16(3):1022–1032, 2014.

[25] Nikolaus M. Loening, Melanie Rosay, Volker Weis, , and Robert G. Griffin*. Solution-state dynamic nuclear polarization at high magnetic field. *Journal of the American Chemical Society*, 124(30):8808–8809, 2002. PMID: 12137529.

[26] James Keeler. *Understanding NMR Spectroscopy*. Wiley-Blackwell, 2010.

[27] I. Solomon. Relaxation processes in a system of two spins. *Phys. Rev.*, 99(2):559–565, 1955.

[28] Anatole Abragam. *The Principles of Nuclear Magnetism*. Oxford University Press, New York, 1961.

[29] Maurice Goldman. Formal theory of spin-lattice relaxation. *J. Magn. Reson.*, 149:160–187, 2001.

[30] Rainer Kimmich. *NMR: Tomography, Diffusometry, Relaxometry*. Springer, 2001.

[31] Bordewijk P. Boettcher C.J.F. *Theory of Electric Polarization, Vol. 2: Dielectrics in Time-Dependent Fields,*. Elsevier Science B. V, 2nd ed. edition, 1978.

[32] Gerald Lffler, Hellfried Schreiber, and Othmar Steinhauser. Calculation of the dielectric properties of a protein and its solvent: theory and a case study1. *Journal of Molecular Biology*, 270(3):520 – 534, 1997.

[33] Stephan Gekle and Roland R. Netz. Anisotropy in the dielectric spectrum of hydration water and its relation to water dynamics. *The Journal of Chemical Physics*, 137(10), 2012.

[34] Y. Ayant, E. Belorizky, J. Alizon, and J. Gallice. Calcul des densit'es spectrales r'esultant d'un mouvement al'eatoire de translation en relaxation par interaction dipolaire magn'etique dans les liquides. *J. Phys. (Paris)*, 36:991–1004, 1975.

[35] L.-P. Hwang and J. H. Freed. Dynamic effects of pair correlation functions on spin relaxation by translational diffusion in liquids. *J. Chem. Phys.*, 63:4017–4025, 1975.

[36] K. Vanommeslaeghe, E. Hatcher, C. Acharya, S. Kundu, S. Zhong, J. Shim, E. Darian, O. Guvench, P. Lopes, I. Vorobyov, and A. D. Mackerell. Charmm general force field: A force field for drug-like molecules compatible with the charmm all-atom additive biological force fields. *Journal of Computational Chemistry*, 31(4):671–690, 2010.

[37] Patrice Bordat, Javier Sacristan, Dirk Reith, Sverine Girard, Alice Glttli, and Florian Mller-Plathe. An improved dimethyl sulfoxide force field for molecular dynamics simulations. *Chemical Physics Letters*, 374(34):201 – 205, 2003.

[38] Deniz Sezer, Jack H. Freed, and Benoit Roux. Simulating electron spin resonance spectra of nitroxide spin labels from molecular dynamics and stochastic trajectories. *J. Chem. Phys.*, 128(16):165106–16, 2008.

[39] James C. Phillips, Rosemary Braun, Wei Wang, James Gumbart, Emad Tajkorshid, Elizabeth Villa, Christophe Chipot, Robert D. Skeel, Laxmikant Kale, and Klaus Schulten. Scalable molecular dynamics with NAMD. *J. Comp. Chem.*, 26:1781–1802, 2005.

[40] Ulrich Essmann, Lalith Perera, Max L. Berkowitz, Tom Darden, Hsing Lee, and Lee G. Pedersen. A smooth particle mesh ewald method. *The Journal of Chemical Physics*, 103(19), 1995.

[41] Shuichi Miyamoto and Peter A. Kollman. Settle: An analytical version of the shake and rattle algorithm for rigid water models. *Journal of Computational Chemistry*, 13(8):952–962, 1992.

[42] H. Ertl and F. A. L. Dullien. Self-diffusion and viscosity of some liquids as a function of temperature. *AIChE Journal*, 19(6):1215–1223, 1973.

[43] Manfred Holz, Stefan R. Heil, and Antonio Sacco. Temperature-dependent self-diffusion coefficients of water and six selected molecular liquids for calibration in accurate 1h nmr pfg measurements. *Phys. Chem. Chem. Phys.*, 2(20):4740–4742, 2000.

[44] J. Barthel and R. Buchner. High frequency permittivity and its use in the investigation of solution properties. *Pure & Appl. Chem.*, 63(10):1473–1482, 1991.

[45] Zijie Lu, Evangelos Manias, Digby D. Macdonald, and Michael Lanagan. Dielectric relaxation in dimethyl sulfoxide/water mixtures studied by microwave dielectric relaxation spectroscopy. *J. Phys. Chem. A*, 113(44):12207–12214, 2009.

[46] Matthew L. Strader and Scott E. Feller. A flexible all-atom model of dimethyl sulfoxide for molecular dynamics simulations. *J. Phys. Chem. A*, 106(6):1074–1080, 2002.

[47] Pascal H. Fries, Daniel Imbert, and Andrea Melchior. Determination of outer-sphere dipolar time correlation functions from high-field nmr measurements. example of a gd[sup 3+] complex in a viscous solvent. *J. Chem. Phys.*, 132(4):044502–11, 2010.

[48] M. J. Frisch, G. W. Trucks, H. B. Schlegel, G. E. Scuseria, M. A. Robb, J. R. Cheeseman, G. Scalmani, V. Barone, B. Mennucci, G. A. Petersson, H. Nakatsuji, M. Caricato, X. Li, H. P. Hratchian, A. F. Izmaylov, J. Bloino, G. Zheng, J. L. Sonnenberg, M. Hada, M. Ehara, K. Toyota, R. Fukuda, J. Hasegawa, M. Ishida, T. Nakajima, Y. Honda, O. Kitao, H. Nakai, T. Vreven, J. A. Montgomery, Jr., J. E. Peralta, F. Ogliaro, M. Bearpark, J. J. Heyd, E. Brothers, K. N. Kudin, V. N. Staroverov, R. Kobayashi, J. Normand, K. Raghavachari, A. Rendell, J. C. Burant, S. S. Iyengar, J. Tomasi, M. Cossi, N. Rega, J. M. Millam, M. Klene, J. E. Knox, J. B. Cross, V. Bakken, C. Adamo, J. Jaramillo, R. Gomperts, R. E. Stratmann, O. Yazyev, A. J. Austin, R. Cammi, C. Pomelli, J. W. Ochterski, R. L. Martin, K. Morokuma, V. G. Zakrzewski, G. A. Voth, P. Salvador, J. J. Dannenberg, S. Dapprich, A. D. Daniels, Ö. Farkas, J. B. Foresman, J. V. Ortiz, J. Cioslowski, and D. J. Fox. Gaussian09 Revision D.01. Gaussian Inc. Wallingford CT 2009.

[49] F Neese. The orca program system. *Wiley interdisciplinary Reviews - Computational Molecular Science*, 2:73–78, 2012.

[50] V Barone. World Scientific Publ. Co., Singapore, 1997.

[51] Jacopo Tomasi, Benedetta Mennucci, and Roberto Cammi. Quantum mechanical continuum solvation models. *Chem. Rev.*, 105(8):2999–3094, 2005.

[52] Eric F. Pettersen, Thomas D. Goddard, Conrad C. Huang, Gregory S. Couch, Daniel M. Greenblatt, Elaine C. Meng, and Thomas E. Ferrin. Ucsf chimera—a visualization system for exploratory research and analysis. *J. Comp. Chem.*, 25(13):1605–1612, 2004.

[53] Deniz Sezer, Jack H. Freed, and Benoit Roux. Parametrization, molecular dynamics simulation, and calculation of electron spin resonance spectra of a nitroxide spin label on a polyalanine alpha-helix. *J. Phys. Chem. B*, 112(18):5755–5767, 2008.

[54] Nora A. McDonald, Heather A. Carlson, and William L. Jorgensen. Free energies of solvation in chloroform and water from a linear response approach. *Journal of Physical Organic Chemistry*, 10(7):563–576, 1997.

[55] Carl L. Yaws. *Thermodynamic and Physical Property Data*. Gulf Publishing, 1992.

[56] Ansgar Schfer, Christian Huber, and Reinhart Ahlrichs. Fully optimized contracted gaussian basis sets of triple zeta valence quality for atoms li to kr. *The Journal of Chemical Physics*, 100(8), 1994.

[57] Aleksandr V. Marenich, Christopher J. Cramer, and Donald G. Truhlar. Universal solvation model based on solute electron density and on a continuum model of the solvent defined by the bulk dielectric constant and atomic surface tensions. *The Journal of Physical Chemistry B*, 113(18):6378–6396, 2009. PMID: 19366259.

[58] Vincenzo Barone, Paola Cimino, and Alfonso Pedone. An integrated computational protocol for the accurate prediction of epr and pnmr parameters of aminoxyl radicals in solution. *Magnetic Resonance in Chemistry*, 48(S1):S11–S22, 2010.

[59] X. Wang, W. C. Isley III, S. I. Salido, Z. Sun, L. Song, K. H. Tsai, C. J. Cramer, and H. C. Dorn. Optimization and prediction of the electron-nuclear dipolar and scalar interaction in 1h and 13c liquid state dynamic nuclear polarization. *Chem. Sci.*, 6:6482–6495, 2015.

[60] John M. Franck, Anna Pavlova, John A. Scott, and Songi Han. Quantitative cw Overhauser effect dynamic nuclear polarization for the analysis of local water dynamics. *Prog. Nucl. Magn. Reson. Spectrosc.*, 74:33–56, 2013.